UNIVERSITAT POLITÈCNICA DE CATALUNYA BARCELONATECH

ICFO The Institute of Photonic Sciences

Generation of Macroscopic Spin Singlets in Cold Atomic Ensembles

DISSERTATION

Submitted for the degree of
Doctor of Philosophy
by
Naeimeh Behbood

ICFO - The institute of Photonic Sciences
UPC - Universitat Politecnica de Catalunya

Thesis Advisor: Prof. Dr. Morgan W. Mitchell

March 16, 2015

Dedicated to my parents and to Hessam

پیشکشی به پدر و مادر عزیزم و به حسام نازنینم

Acknowledgements

I believe doing a PhD is not just about finishing a project but about improving the personality and knowledge of the people involved in it. I have done my PhD under supervision of Morgan Mitchell and I am in huge debt to him. You will not find someone with his personality quite often around you and having him as your supervisor, I think you should be very fortunate. He is a good experimentalist, a good theoretician, a good touter and very generous to share his knowledge with people. I have enjoyed working with him and in his group and I would like to thank him for all his support and all discussion about physics and beyond.

Also my huge thanks goes to atom team. I have been fortunate enough to work with many bright people in the lab, from early days with Marco, Mario and Brice whom their friendship is very valuable to me, till later on, that we bound a great team with Rob, Giorgio and Ferran. We experienced many challenges, frustrations and also great successes together. Thank you guys.

The nice ambient of our group which make it feel like home is because of nice people sharing their good mode, nice jokes and though about physics and life. Many thanks to Florian, Anna, Ale, Federica, Yannick, Gian Vito, Joanna, Jia, Ricardo, Thomas, Natali, Silvana, Simon, David and all the visitors and summer students.

I would like to thank Gemma for being such a nice teacher and Geza for all his interest over the years on singlet project. I have learned a lot from Ivan during his short visit in ICFO, I would like to also thank him for the nice discussions and very nice lectures.

ICFO is a great place because of the great people. Being at ICFO has been a fantastic experience from the first day and although it is changing and growing, it never get a less interesting place. Thank to all ICFOnians.

I thank all people in electronic workshop and mechanical workshop, also people in human resource, in purchasing unit, logistics, IT-support. Life would be much harder without their support and hard work.

My biggest thank to Hessam in the long journey that we went through together and the experience that with you became sweet and worth to continue. I love you.

Abstract

This thesis describes the generation of macroscopic spin singlets in a cold atomic ensemble by performing quantum non-demolition measurement. Toward this goal we have implemented a real-time shot-nose limited detection system, incoherent feedback and spin state preparation via optical pumping, an upgraded absorption imaging system and coherent rotation of atomic spin via magnetic field control.

Working with a magnetically sensitive atomic system triggered the development of a vector field magnetometry technique. We demonstrate a fast three-axis optical magnetometer using cold, optically trapped ^{87}Rb gas as a sensor. By near-resonant Faraday rotation we record the free-induction decay following optical pumping to obtain the three field components and one gradient component. A single measurement achieves shot-noise limited sub-nT sensitivity in 1 ms, with transverse spatial resolution of about 20 μm. We make a detailed analysis of the shot-noise-limited sensitivity.

We apply entropy removal by measurement and feedback to a cold atomic spin ensemble. Using quantum non-demolition probing by Faraday rotation measurement, and feedback by weak optical pumping, we drive the initially random collective spin variable $\mathbf{F}$ toward the origin $\mathbf{F} = 0$. We use input-output relations and ensemble quantum noise models to describe this quantum control process and identify an optimal two-round control procedure. We observe 12 dB of spin noise reduction, or a factor of 63 reduction in phase-space volume. The method offers a non-thermal route to generation of exotic entangled states in ultra-cold gases, including macroscopic singlet states and strongly correlated states of quantum lattice gases.

We generate approximate singlet states using the tools of measurement-induced spin squeezing: quantum non-demolition measurement and coherent magnetic rotations. By squeezing all three spin components, we approach the zero spin noise. Using a cold Rubidium atomic ensemble and near-resonant Faraday rotation probing, we have observed up to 3 dB of squeezing relative to the standard quantum limit, and a violation of the generalized spin squeezing inequality by more than 5 standard deviations.

Resumen

Esta tesis describe la generación del estado singlete de espín macroscópico formado por un conjunto de átomos fríos mediante medidas cuánticas no destructivas. Para tal objetivo hemos implementado un sistema de detección en tiempo real limitado por propiedades fundamentales de la luz, "shot noise", así como un sistema de retroalimentación (feedback) incoherente, una preparación del estado de espín mediante bombeo óptico, una mejora del sistema de absorción de imágenes y un control del campo magnético para rotar de forma coherente el espín de los átomos.

Trabajar con átomos sensibles al campo magnético desencadenó la necesidad de desarrollar una técnica pare medir el vector del campo magnético. Hemos demostrado un magnetómetro rápido, óptico, tri-axial que utiliza átomos de ^{87}Rb atrapados ópticamente como sensor. Midiendo el decaimiento libre de la inducción (FID) a través de la rotación de Faraday con pulsos casi-resonantes obtenemos las tres componentes del campo así como una componente del gradiente. Una única medida está limitada por shot-noise y sensible en el rango sub-nT en 1 mili-segundo, con una resolución espacial transversa de 20 micrómetros. En el cuerpo de la tesis estudiamos con detalle la sensibilidad en el límite 'shot-noise'.

Reducimos la entropía en un conjunto de átomos fríos con medidas y feedback. Utilizando medidas cuánticas no destructivas con la rotación de Faraday, y aplicando un leve feedback por bombeo óptico, llevamos la distribución inicial aleatoria de la variable colectiva de espín $\mathbf{F}$ hacia el origen de coordenadas $\mathbf{F} = 0$. Utilizando relaciones de entrada-salida y modelos colectivos de ruido cuántico para describir la interacción identificamos como

rutina óptima repetir el proceso de medir y feedback dos veces. Experimentalmente observamos 12 dB de reducción del ruido del espín, o una reducción en el espacio de fases de un factor 63. Éste método ofrece un procedimiento no térmico para la generación de estados entrelazados exóticos en gases ultrafríos, incluyendo un estado de singlete macroscópico y estados fuertemente correlacionados en quantum lattice gases.

Generamos estados que se aproximas al estadosinglete utilizando los recursos que inducen spin squeezing: medidas no destructivas y rotaciones magnéticas coherentes. Al reducir el ruido en las tres componentes del espín, nos acercamos al cero ruido de espín. Utilizando un conjunto de átomos fríos de Rubidio y rotaciones de Faraday casi-resonantes, hemos observado hasta 3 dB de squeezing relativos al límite cuántico estándar, y una violación de la generalización de la desigualdad para spin squeezing de más de 5 desviaciones estándar.

Contents

1
Introduction

In the first half century of quantum mechanics the theory was developed with the consideration that the outcome of the experiments are probabilistic with various possible outputs and this was the case because the technology of that era was incapable of making a measurement without destroying or severely changing the measured object. In the 1960s, the development of quantum optics opened the possibility to make repetitive quantum measurements on a single quantum object with minimal effect of each measurement on the system. For decades after that the quantum features of light-atoms interaction have been studied in the framework of cavity QED where light can be efficiently coupled to a few atoms. Later on, the collective behavior of light-matter interaction began to play more and more important role in different areas of quantum optics and atomic physics such as quantum memory, teleportation schemes, metrology and tomography.

1.1 quantum theory of measurement

Real measurements can be divided into two groups:
1)Direct measurement:
Direct measurement refers to quantum measurements in which the measured system interacts with a macroscopic measurement device. This measurement collapses the wave-function such that no additional information can be obtained.
2) Indirect measurement:

Indirect measurement refers to a situation, in contrast to what you have in direct measurement, in which the system of interest interacts with a second system, known as "meter", (or probe) and then the meter (not the system) interacts with the macroscopic measurement apparatus. In the first step, the quantum system interacts with a probe such that a correlation is established between the quantum system and quantum probe. The second step is the direct measurement of the observable of the quantum probe. The state of the probe will collapse in this step and since there is correlation between the system and the probe, it will lead to reduction of the state of the quantum object. To achieve high precision in indirect measurement, the second step should not contribute significantly to the total error of the measurement. Given that this condition is satisfied in the indirect measurement, the only perturbation of the object would be that caused by the quantum probe. In the ideal case, this perturbation will be the minimum allowed by the quantum uncertainty of probe initial state coming from the Heisenberg principle.

1.1.1 Quantum non-demolition measurement

In the 1970s, in connection to the project of construction of a gravitational wave detector, it became necessary to invent new methods of measurement. These new methods aimed to detect gravitational waves with reasonable probability and for this needed to improve the measurement precision for free mass detectors or mechanical harmonic oscillators. The big challenge was the fact that the precision of conventional measurements cannot overcome the standard quantum limits that are imposed by the Heisenberg uncertainty relations. The solution to this challenge was a certain nonstandard measurement scheme, which was based on the careful choice of the observable and a careful preparation of the measurement device. This nonstandard measurement was called quantum non-demolition measurement [1].

Although the concept of the QND measurement was developed for gravitational wave detectors, the idea has not been demonstrated in this area. Rather, it was demonstrated in quantum optics.

Consider a system, described by conjugate variables q, p, with $[p, q] = i$

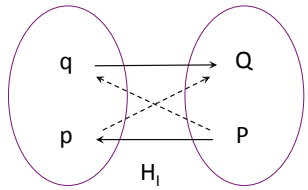

Figure 1.1: schematic of the interaction between the system and the measurement.

in interaction with a meter described by P, Q with commutation relations $[P, Q] = i$. The Heisenberg equations of motion for the variable of the system q and variable of the meter P are:

$$i\frac{d}{dt}q = -[H_s, q] - [H_I, q] \tag{1.1}$$

$$i\frac{d}{dt}P = -[H_m, P] - [H_I, P] \tag{1.2}$$

where H_s is the Hamiltonian of the system, H_m is the Hamiltonian of the meter and H_I is the interaction Hamiltonian between the system and the meter. In order to measure q using P such that the q remains protected against interaction, the interaction Hamiltonian H_I should be a function of q, otherwise q has no effect on the meter, and the commutator $[H_I, q] = 0$ to avoid back-action on q. The QND Hamiltonian for the system and the probe used in this thesis is described in more detail in chapter 2.

1.2 Macroscopic singlet state

The goal of this thesis is to generate a macroscopic spin singlet in a cold atomic ensemble. The singlet state is defined for two spin-1/2 particles as

$$\psi = \frac{1}{\sqrt{2}}(|\uparrow\downarrow\rangle - |\downarrow\uparrow\rangle) \tag{1.3}$$

which is a maximally entangled state. The macroscopic spin singlet is a state containing a large number of atoms with total angular momentum $\mathbf{F} = 0$

and total variation of angular momentum $|\Delta\mathbf{F}|^2 = 0$.

The same concept is valid for continuous light source where simultaneous fluctuation suppression in three Stokes observables below the shot-noise limit has been demonstrated [2, 3, 4, 5]. For this macroscopic singlet state, the mean value of the polarization Stokes observables is $\langle S_1\rangle = \langle S_2\rangle = \langle S_3\rangle = 0$, showing that the states are unpolarized. Due to this unpolarised behaviour, the uncertainty relation $\Delta S_i \Delta S_j \geq |\langle S_k\rangle|, (i \neq j \neq k = 1, 2, 3)$ impose no restriction on the noise suppression in all the Stokes observable simultaneously. This provides the possibility to suppress the noise of all Stokes observable.

1.2.1 Spin singlets and entanglement

The concept of generating a macroscopic singlet state in our case is closely related to spin squeezing and noise reduction using quantum non-demolition measurement [6, 7, 8]. Generating and detecting large-scale spin entanglement in many-body quantum systems is of fundamental interest [9, 10] and motivates many experiments with cold atoms [11, 12, 13, 14, 15] and ions [16]. For example, macroscopic singlet states appear as ground states of many fundamental spin models [17, 18], and even in quantum gravity calculations of black hole entropy [19]. Being able to engineer such states in cold atoms will open the path to study quantum magnetism [20] and 'exotic' types of antiferromagnetic order [21] and systems with critical behaviour such as phase transition and spin liquids [17] in cold atom systems.

More broadly long-range entanglement is observed or hypothesised in many different areas of science including in biology, chemistry, materials science, condensed matter physics which allows complex systems to perform extraordinary behaviour such as high temperature superconductivity, high-efficiency photosynthesis [22, 23] and magneto-reception in birds [24, 25].

1.2.2 Gradient magnetometry with singlets

The macroscopic singlet state can be used also for quantum metrology proposes. This state is invariant under homogenous magnetic field, but the spins at different locations of the atomic ensemble are rotating differently in

the presence of the gradient of the magnetic field. During this process, the variance of the collective spin component will increase and that can be used to measure the field gradient [26, 27].

1.3 Quantum control

In this thesis, we also used the concept of the quantum feedback control to achieve spin cooling [28]. Quantum feedback control has been used to improve the system performance in different areas of quantum optics, including quantum error correction [29, 30, 31], generating spin squeezed state and entangled state [32, 33]. Even though this approach was not used directly to generate macroscopic spin singlets [34], it can be considered as an approach to generate such states in cold atomic ensemble.

1.4 content of the thesis

The experiments that are reported in this thesis are divided into two main categories. The first category is using atoms as a sensitive device to measure the magnetic field with high precision. The free induction decay signal obtained from QND probe is used to access to the information of the three components of the field and one component of the gradient of the field. The related theoretical background and the experiment are explained in chapters 4 and 5 respectively. This vector magnetometry technique provides the possibility to apply coherent rotation of the spin using a magnetic field that is well defined both in amplitude and in direction. This technique also provides the possibility to measure all components of the angular momentum.

The other category is more closely related to the generation of new exotic quantum states in the cold atomic ensemble. The experiments related to generation of new quantum states, manipulation of the atomic state and their theoretical background are discussed in chapters 6, 7, 8 and 9.

In the experiment explained in chapter 7, we apply entropy removal by measurement and feedback to a cold atomic ensemble in the spin cooling experiment. Using quantum non-demolition probing by Faraday rotation

measurement, and feedback by weak optical pumping, we drive the initially random collective spin variable $\mathbf{F}$ toward the origin $\mathbf{F} = 0$. We use input-output relations and ensemble quantum noise models to describe this quantum control process and identify an optimal two-round control procedure. The method offers a non-thermal route to generation of exotic entangled states in ultra-cold gases, including macroscopic singlet states and strongly correlated states of quantum lattice gases.

In the experiment explained in 9, we generate approximate singlet states using the tools of measurement-induced spin squeezing: quantum non-demolition measurement and coherent magnetic rotations . By squeezing all three spin components, we approach the zero of total spin. Using a cold Rubidium atomic ensemble and near-resonant Faraday rotation probing, we have observed spin squeezing and generation of spin singlets in the cold atomic ensemble.

2
Theoretical background

This chapter summarizes the theoretical framework for the collective light-matter interaction. The system that we want to acquire information about are the atoms and the probe is the light. First we will see the definition of light and atomic spins for our system, before describing the Hamiltonian.

2.1 Continuous variable of light

The light can be described in terms of Stokes operators (see e.g. [35]). The Stokes operators of light are measurable quantities which are represented by S_0, S_x, S_y and S_z. S_0 represents half the total number of photons, S_x is half the difference between the number of photons polarized along x and y axes, The x and y axes are usually selected to be parallel to horizontal and vertical direction in laboratory. S_y is the analogue of S_x in the frame rotated by 45° and S_z is the analogue for left and right circularly polarized components. The components of the Stokes vector are given by:

$$S_0 = \frac{1}{2}\mathbf{a}^\dagger I \mathbf{a}, \qquad S_x = \frac{1}{2}\mathbf{a}^\dagger \sigma_x \mathbf{a}, \qquad S_y = \frac{1}{2}\mathbf{a}^\dagger \sigma_y \mathbf{a}, \qquad S_z = \frac{1}{2}\mathbf{a}^\dagger \sigma_z \mathbf{a}. \tag{2.1}$$

Here $\mathbf{a} \equiv [a_+, a_-]^T$ and a_+, a_- are annihilation operators for circular plus and minus polarization respectively, I is the identity matrix and σ_x, σ_y and σ_z are the Pauli matrices. To simplify the notation we used $\hbar = 1$ in our description.

The Stokes operators obey the standard spin commutation relations

$$[S_i, S_j] = i\epsilon_{ijk} S_k. \tag{2.2}$$

2.2 Continuous variable of atoms

The atom that we are using to study the light-atom interaction is rubidium-87 atom. ^{87}Rb has 37 electrons, only one of which is in the outer most shell. The D_2 transition line (connecting $5^2S_{1/2} \rightarrow 5^2P_{3/2}$)of ^{87}Rb is the most relevant to our experiment. The name D_2 transition identifies the transition within the fine structure of the rubidium spectrum, but in addition there is hyperfine structure. The fine structure is a result of the coupling between the orbital angular momentum $\mathbf{l}$ of the outer electron and its spin angular momentum $\mathbf{s}$. The total angular momentum is given by

$$\mathbf{j} = \mathbf{l} + \mathbf{s} \tag{2.3}$$

The hyperfine structure is a result of the coupling of $\mathbf{j}$ with the total nuclear angular momentum $\mathbf{i}$. The total angular momentum $\mathbf{f}$ is then given by

$$\mathbf{f} = \mathbf{j} + \mathbf{i} \tag{2.4}$$

and the magnitude of $\mathbf{f}$ varies between $|\mathbf{j} - i| \leq f \leq \mathbf{j} + i$. For the ground state of ^{87}Rb , $l = 0$ and $s = 1/2$, so $j = 1/2$ and $I = 3/2$, so $f = 1$ or $f = 2$. For the excited state of the D_2 line f can be 0,1,2 or 3.

The operator of total angular momentum is denoted by $\mathbf{f}$ and any components of it comutes with $\mathbf{f}^2$. The spectrum of $\hat{f}_z$ is discrete with eigenvalues m, $m \in \{-f, -f+1, ..., f-1, f\}$ and the eigenvalue of $\mathbf{f}^2$ is $f(f+1)$.

$$\hat{f}_z|f, m\rangle = m|f, m\rangle \tag{2.5}$$

$$\mathbf{f}^2|f, m\rangle = f(f+1)|f, m\rangle. \tag{2.6}$$

The vectors $|f, m\rangle$ form a complete orthogonal basis and the components f follow the commutation relation

$$[\hat{f}_r, \hat{f}_s] = i\epsilon_{rst}\hat{f}_t \tag{2.7}$$

A collective spin operator for an ensemble of N_A atoms is defined as

$$\hat{\mathbf{F}} = \sum_{k=1}^{N_A} \hat{\mathbf{f}}^{(k)} \tag{2.8}$$

where $\hat{\mathbf{f}}^{(k)}$ is the spin operator for the kth atom. In addition to these well-known vector spin components, sometimes referred to as spin orientation, a spin-1 or larger atom also has tensor spin components, referred to as spin alignment. The tensor spin operators $\hat{j}_x$, $\hat{j}_y$ and $\hat{j}_m$ are defined as

$$\hat{j_x} = \hat{f}_x^2 - \hat{f}_y^2 \tag{2.9}$$

$$\hat{j_y} = \hat{f}_x\hat{f}_y + \hat{f}_y\hat{f}_x \tag{2.10}$$

$$\hat{j}_m = \frac{1}{\sqrt{3}}(2\hat{f}_z^2 - \hat{f}_{\mathrm{x}}^2 - \hat{f}_{\mathrm{y}}^2) \tag{2.11}$$

where the collective tensor spin operator $\hat{\mathbf{J}}$ is

$$\hat{\mathbf{J}} = \sum_{i=1}^{N_A} \hat{\mathbf{j}}^{(i)}. \tag{2.12}$$

Collective spin operators obey the same commutation relation as single particle operators

$$[\hat{F}_{\mathrm{r}}, \hat{F}_{\mathrm{s}}] = i\epsilon_{rst}\hat{F}_{\mathrm{t}} \tag{2.13}$$

As quantum mechanical quantities, these collective spin operators obey the Heisenberg uncertainty principle as follow

$$\mathrm{var}(\hat{F}_{\mathrm{r}})\mathrm{var}(\hat{F}_{\mathrm{s}}) \geq \frac{1}{4}|\epsilon_{rst}|\langle\hat{F}_{\mathrm{t}}\rangle^2. \tag{2.14}$$

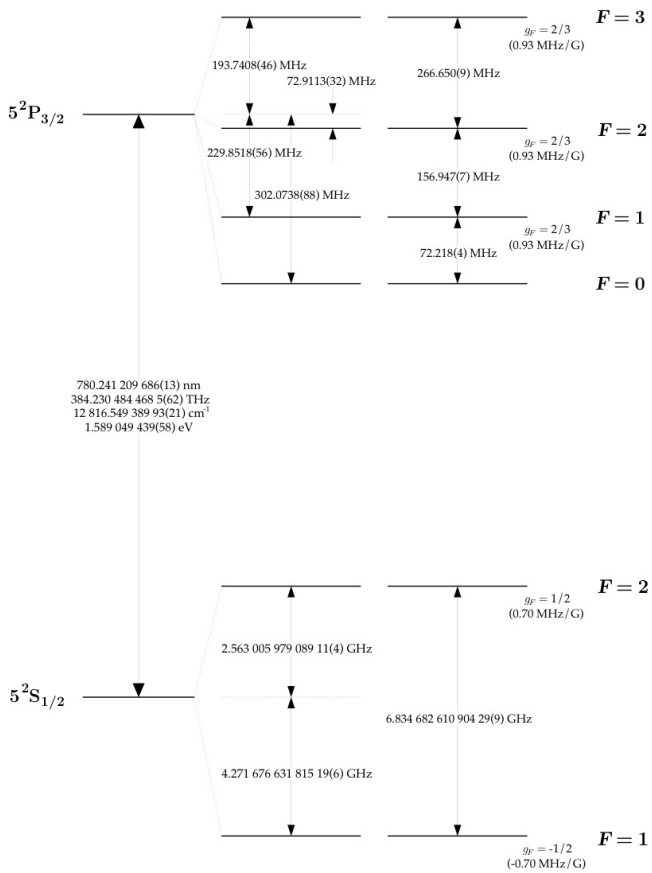

Figure 2.1: Detailed level diagram of ^{87}Rb D_2 transition hyperfine structure, with frequency splitting between the hyperfine energy levels. The figure is taken from [36].

2.2.1 Effective Hamiltonian

Several groups [37, 38, 39] have studied the effective interaction Hamiltonian of the case where the detuning of the light is much larger than the excited level hyperfine splitting. This interaction Hamiltonian can be interpreted as a scattering interaction: the atoms are first brought to a virtual excited state via the raising operator $\mathbf{d}^\dagger$ by annihilating a photon from the probe field through $\mathbf{E}^{(+)}$. Later, these virtual excited atoms decay back to the ground state by emitting a photon into a potentially different probe mode via $\mathbf{d}$ and $\mathbf{E}^{(-)}$. The full Hamiltonian for the collective atomic spin has been described in detail in [38, 40]. It can be written as

$$H_{\text{int}} = \frac{1}{\tau} G_1 \hat{S}_z \hat{F}_z + \frac{1}{\tau} G_2 [\hat{S}_x \hat{J}_x + \hat{S}_y \hat{J}_y + \frac{1}{\sqrt{3}} \hat{S}_0 \hat{J}_m] \tag{2.15}$$

where G_1 and G_2 are the light-atom coupling constants proportional to vector polarizability $\alpha^{(1)}$ and tensor polarizability $\alpha^{(2)}$ components, respectively. The detuning dependence of the coupling constant G_1 and G_2 is given by

$$G_1 = \frac{\sigma_0}{A} \frac{\Gamma}{16} (-4\delta_0(\Delta) - 5\delta_1(\Delta) + 5\delta_2(\Delta)) \tag{2.16}$$

$$G_2 = \frac{\sigma_0}{A} \frac{\Gamma}{16} (4\delta_0(\Delta) - 5\delta_1(\Delta) + \delta_2(\Delta)) \tag{2.17}$$

where $\delta_i(\Delta) \equiv 1/\sqrt{\Gamma^2 + (\Delta - \Delta_i)^2}$, Δ_i is the frequency difference between the lowest excited hyperfine level, $f' = 0$ and the level with $f' = i$. The detuning from the resonance $F = 1 \rightarrow F' = 0$ is called Δ where for red detuning $\Delta < 0$. $\sigma_0 \equiv \frac{\lambda^2}{\pi}$ where λ is the transition wavelength and A is the effective atom-light interaction area and Γ is the excited state linewidth. Note that for large detuning, i.e. $\Delta \gg \Gamma$, $G_1 \propto 1/\Delta$ and $G_2 \propto 1/\Delta^2$ [38]. Due to the dependence of G_1 and G_2 to the detuning, it is possible to choose between the first term of the interaction Hamiltonian and the second term of the interaction Hamiltonian and engineer the Hamiltonian depend on the use that one desires [38, 41].

In many experiments that require sensitivity at the projection noise level, the effect of the G_2 term cannot be neglected [7]. Still in the experiments reported in this thesis we can and will ignore the effect of the G_2 term. In the vector magnetometry and spin-cooling experiments, the spin-measurement sensitivity never reached the projection-noise level, but rather was limited by technical noise contributions. For this reason, the additional quantum noise from the G_2 term was not important. In the case of the macroscopic singlet state, the quantum noise is the important effect that we are studying, but since the initial state is the thermal spin state, the quantum noise added due to G_2 is small. See section 9.1 for a quantitative discussion.

2.2.2 Loss and decoherence due to probing

We measure G_1 and G_2 by observing the average rotation for a known number of atoms in a polarized state as has been shown in chapter 3. To characterize depolarization, we measure the depolarization as a function of number of photons in the probe. At any detuning, the measurement sensitivity can be improved by increasing the number of photons N_L used in the measurement. Note, however, that increasing N_L also increases the damage done to atomic state that we are trying to measure due to probe scattering. The amount of this damage can be defined by the total damage η_{sc} for a number N_L of photons in the probe as:

$$\eta_{sc} = k(\Delta)\eta_\gamma N_L \tag{2.18}$$

where $k(\Delta)$ is the correction factor that accounts for the fact that a fraction of the scattering events leave the state unchanged. η_γ is the probability of scattering a single photon:

$$\eta_\gamma = \frac{\sigma_0}{A}\frac{\Gamma^2}{64}(4\delta_0(\Delta)^2 + 5\delta_1(\Delta)^2 + 7\delta_2(\Delta)^2) \tag{2.19}$$

which also scales as $\eta_\gamma \propto 1/\Delta^2$ for large detuning. A is the effective interaction area between light and atoms and σ_0 is the on-resonance scattering cross-section for atoms in $F = 1$ ground state where we assume that the

excited states are degenerate and interact with linearly polarized light [42].

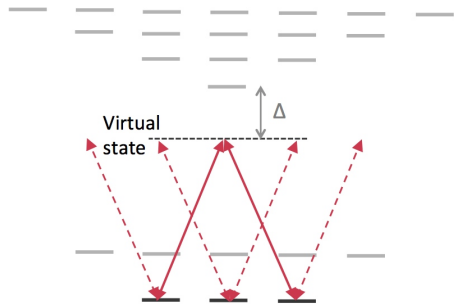

Figure 2.2: The hyperfine structure of ^{87}Rb. The arrows represent the light during the probing.

As mentioned earlier in this chapter 2.2.1 , we can engineer the interaction Hamiltonian such that one or other term of the interaction Hamiltonian becomes dominant. For most of the experiment reported in this thesis the parameters of light has been chosen such that QND term of the Hamiltonian be the dominant term. To study the atomic state properties of the system, there are two main approach that we have followed: The first one is input-output relation and the other is covariance matrix approach. Before each experimental chapter, there is one preliminary chapter where I introduce the formalism of the relevant approach for the experiment explained in the later chapter and the theoretical background related to the experiment.

3

Experimental setup

3.1 General overview of the setup

In this chapter I present new techniques, instruments, and apparatus that were developed for the experiments reported in this thesis. The cooling and trapping setup was described several times in previous doctoral theses [43, 44, 45, 46, 47]. For that reason, I concentrate on extensions and improvement of the existing setup. This setup is designed to manipulate and measure the collective spin state of a cold ^{87}Rb atomic ensemble.

The atoms are cooled to 25μK by laser cooling and trapping techniques and the atomic ensemble is trapped in an elongated far off resonance trap. The elongated trap geometry permits a strong light-atom interaction. The atomic state is measured via the induced Faraday rotation on polarized light pulses by a very low noise balanced polarimeter. The experimental setup consists of a two stage vacuum chamber. Rubidium atoms are released from the reservoir to the upper stage of the vacuum chamber where they are cooled in a 2D Magneto Optical Trap (MOT). In the next step these cooled atoms are guided with a push beam to the lower vacuum chamber and accumulate in the 3D MOT. The schematic of the experimental setup is shown in Fig. 3.1.b. The dipole beam is overlapped to the 3D MOT and once the atoms are loaded into the dipole trap, the MOT beams and the gradient of the magnetic field are switched off and the atoms are trapped in an all-optical trap as shown in Fig. 3.2.

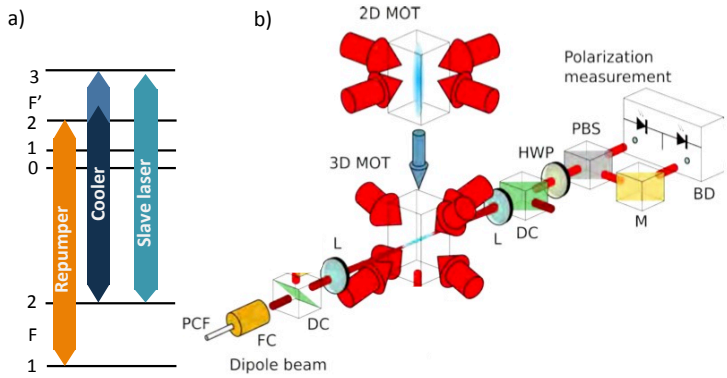

Figure 3.1: a) Light fields used for magneto-optical trapping: Repumper, cooler and slave laser. b)The schematic of the dipole trap and the 2D MOT and the 3D MOT. The upper 2D MOT works at higher background pressure of about 10^{-8} mbar. Four crossed propagating beams trap and cool atoms into an elongated sample. A push beam in the vertical direction guides cooled and trapped atoms into the lower chamber. The lower chamber has a smaller background pressure of about 10^{-11} mbar to reduce the collisions among atoms. In the lower chamber, the atoms are collected into a 3D MOT and in the last stage of trapping atoms are transferred from the 3D MOT into an all-optical trap. Image created by M. W. Mitchell.

3.1.1 Laser systems

In the process of magneto optical cooling, there are two lasers that are involved. One of the lasers is the cooler laser which is in charge of trapping atoms and the other is the repumper laser which is recycling the atoms that spontaneously fall into the $F = 1$ ground state back to the $F = 2$ ground state. Both lasers that we have used for cooler and repumper are external cavity diode lasers (Toptica DL 100). The cooler laser is locked close to $F = 2$ to $F' = 2$ of ^{87}Rb and it is stabilized by means of a saturation absorption spectroscopy setup. The laser is shifted by 60 MHz to the blue before it enters into the spectroscopy setup to have a large range for the cooler detuning of many natural line-widths. We use a double-pass AOM in the path of the cooler beam to control the detuning of the locked laser relative to the $F = 2$ to $F' = 3$ transition to 80 MHz to red of this transition. The large range of detuning is important for sub-Doppler cooling and helps to increase the number of atoms in the dipole trap. In order to enhance the cooling power, about 1 mW of the cooler laser power is used to injection-lock a second laser known as the "slave laser". The injection locked laser is locked to $F = 2$ to $F' = 3$ transition with a 10 MHz frequency shift to the red. The repumper laser is locked with a similar technique to the transition from $F = 1$ to the cross over transition $F' = 1$ and $F' = 2$. The light is shifted by a single pass AOM to the resonance $F = 1$ to $F' = 2$ as has been shown in Fig. 3.1.a. A detail information of the cooler and repumper laser system can be found in [46]. The laser used for far off-resonant dipole trap is a 1064 nm IPG fiber laser which is capable of providing 20W of continuous laser power. All the laser sources are fiber coupled for delivering light to the trap to have a better stability and clean spatial modes.

3.1.2 State preparation

The same lasers that have been used for cooling and repumping tasks are used for optical repumping and optical pumping to prepare initial desired atomic state or to apply optical feedback. There is a more detailed description of optical pumping in section 3.4.

3.1.3 Atom counting

There are two techniques that we are using for atom counting. One is the absorption imaging technique which has a illumination system at the side of the trap. The details of the illumination setup have been explained in section 3.5.1. The other technique is the dispersive atom number measurement (DANM). In this technique, we first optically pump the atoms into the maximally F_z polarized state, and then we use paramagnetic Faraday rotation measurements to measure the rotation angle $\phi = N_A G_1$. G_1 is calibrated using absorption imaging, as has been explained in section 3.6. This allows us to have a reference of the number of atoms without the destructiveness of absorption imaging.

Figure 3.2: Absorption image of the dipole trap.

The atomic distribution along the longitudinal axis varies from one trap loading to another, and reflects the dynamics of trap loading rather than a thermal equilibrium distribution. In some cases it is closer to a Gaussian distribution and in some other cases it is closer to a Lorentzian distribution. Depending on the situation of each experiment in some cases we have treated the atomic distribution as a Gaussian distribution and in some other case we considered it as a Lorentzian distribution.

3.2 Real-time shot noise limited detector

Here I will provide some details about the real time detection system capability that has been incorporated into the existing apparatus during this thesis. This detection system provides the possibility to detect the atomic spin polarization in real time. Although the old detection system detected the spin polarization in real time in the form of an analog signal few microsecond after the pulse, this detection was not very useful for feedback: since the measurement outcome was recorded on oscilloscope for offline analysis

to obtain information about the rotation angle and it was impossible to use it for feedback. The capability of real-time calculation of rotation angle is essential for applying feedback to the atomic spins for control of the spins of the atomic ensemble. This real time calculation opened the path to apply feedback to control atomic spin in real time via two digital output channels. This real time detection system has two parts. The first part is the shot-noise limited polarization detection and the second part is the pulse acquisition and processing device. The shot-noise limited detection includes optics, photodiodes and amplification electronics for the polarimeter part of the detector and digitisation electronic and pulse integration measurement or oscilloscope for visualisation. The details of the shot-noise limited detection system has been explained in [46] and [48]. Here I describe the digitization electronics (pulse acquisition and processing device). This module also performs another function: real-time computation of ϕ and the generation of the digital output signal for feedback. In order to detect the spin polarization of atomic ensemble, we use pulses of off-resonant light with well defined polarization and we measure polarization rotation of the light with a pulsed polarimeter down to very small angles below 10^{-4} rad. The polarimeter detector helps us to measure the change in the polarization of the input light. The angle of the rotation is proportional to $\hat{S}_{\mathrm{y}}/\hat{S}_{\mathrm{x}}$. We gain information on $\hat{S}_{\mathrm{y}}$ using measurement of polarization in 45 °-basis. For the input polarization measurement, we gain the information of the number of photons of the input pulse from reference detector $\hat{S}_{\mathrm{x}}$. The rotation angle of the Stokes vector can be calculated by

$$\phi = \frac{\hat{S}_{\mathrm{y}}^{\mathrm{meas}}}{\hat{S}_{\mathrm{x}}^{\mathrm{in}}} \tag{3.1}$$

in the small angle approximation, where $\hat{S}_{\mathrm{y}}^{\mathrm{meas}}$ is the measured photon-number imbalance. The pulse processing system (PIMAT) added to the detection system facilitates the calculation of the rotation angle.

The PIMAT electronics, shown schematically in Fig. 3.3 consists of an AD9248, 2 channel, 14-bits, 15 MSPS/ch Analog to Digital Convertor (ADC) that is 50 Ω- AC coupled. The hardware of PIMAT is connected through

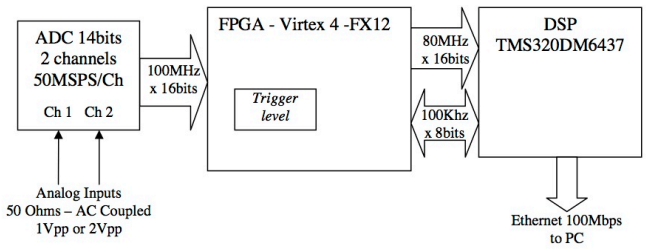

Figure 3.3: Schematic of the pulse acquisition and processing device.

Ethernet connection into a PC and the user interface program in visual C is used to control the different parameters such as triggering level and integration windows. Polarimeter detector and reference detector are connected to channel A and channel B of the ADC, respectively. The ADC is connected to a Field-Programmable Gate Array (FPGA). The FPGA has an on-board power PC. The exact model of this FPGA is FPGA-Virtex 4-FX12 xc4VFX12. All the tasks regarding acquiring data and integrating windows are happening in the FPGA. The tasks regarding the calculation of the ratio is carried out on the on-board processor of the FPGA and the results of the calculations performed on on-board processor (power PC) are passed again into the FPGA. This is the slowest part of the process and the system has a latency of 7μs. FPGA then will send the data to PC via a video channel of 16 bits through the DSP. There are two channels of communication between FPGA and PC. Both are connected through a DSP as shown in Fig. 3.3. The first Channel has a speed of 80 MHz and 16-bits resolution path and is used to send the data to the PC. The second channel, is used to receive the control data from the PC. It has a speed of 100 KHz and 8-bits resolution. It is in charge of communicating the triggering level, the starting points of each window, the length of each window and the gain of the digital output signals that are used for feedback.

The signal of channel B is used for triggering. The capturing and displaying starts when the signal of channel B is above the triggering level which we set at the user interface. In Fig. 3.3 the trigger level is indicated. Data of

each channel is divided into three windows as shown in Fig. 3.4. For example in channel A, there are three integration windows marked as I_{a0}, I_{a1}, I_{a2}. I_{a1} refers to the integration window of the pulse signal and I_{a0} and I_{a2} refer to the integration windows of before and after the pulse. The calculations that are done on FPGA and DSP include the integration of each window for each channel $I_{a0}, I_{a1}, I_{a2}, I_{b0}, I_{b1}, I_{b2}$. In order to choose the right windows for each channel, we use the user-interface. In user-interface we define $N_{a,i}, N_{b,i}, W_{a,i}$ and $W_{b,i}$ where $i = \{0, 1, 2\}$. In channel A, $N_{a,1}$ defines the start point of the signal with respect to the trigger level and $W_{a,1}$ defines the length of the window of the pulse. $N_{a,0}$ and $N_{a,2}$ are referred to the starting point of the background windows and are defined in respect to the $N_{a,1}$. $W_{a,0}$ and $W_{a,2}$ are indicating the window area defined in the user interface for the background regain. The same processing method is valid for channel B. The length of each window can vary in the range of 0 to 511 samples. The time resolution is 20 ns per sample. The timing diagram is shown in Fig. 3.4. The device is providing the digital signal with the information about the voltage received from each detector. The summation over this pack of digitized data for each given window provides the integration of each window.

The ADC performs a continuous digitization of the input signal at a rate of 50 Msps, or 20 ns per sample. The FPGA performs several functions on digitized data. First, it identifies the trigger event when the V_B crosses the trigger level. All other time points are defined with respect to this trigger. The FPGA then computes integrals over three time windows, defined as in Fig. 3.4. The definition of the time windows, i.e., the parameters $N_{a,0}$, ... $W_{b,2}$, are set via the user interface.

$$I_{a0} = \sum_{i=0}^{W_{a0}} \mathrm{d_i}(a, 0) \tag{3.2}$$

where $\mathrm{d_i}(\mathrm{a}, 0)$ is the digital voltage per sample of windows $W_{a,0}$. Calculation of angle of rotation requires calculation of the Stokes operators $\hat{S}_{\mathrm{y}}$ from channel A and $\hat{S}_{\mathrm{x}}$ from channel B. This part of the calculation requires calculating a ratio, which is a complicated task for FPGA to perform. To

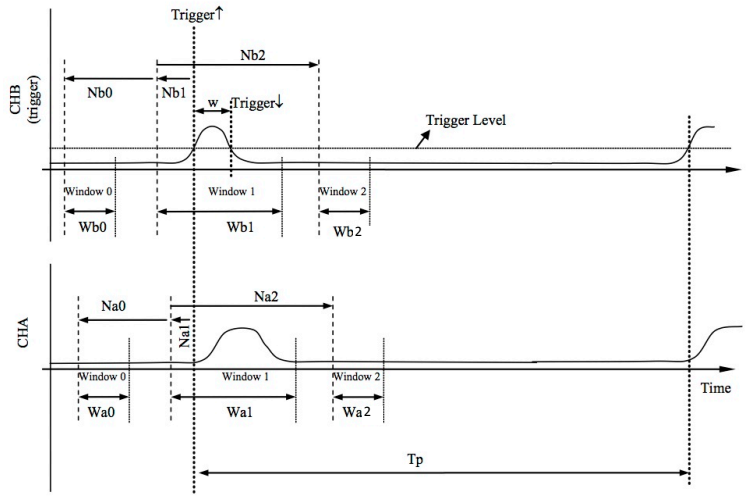

Figure 3.4: Timing diagram and definition of timing-related quantities. In channel A, $N_{a,1}$ defines the start point of the signal with respect to the trigger level and $W_{a,1}$ defines the length of the window of the pulse. To define the starting points of the two background windows, we use $N_{a,0}$ and $N_{a,2}$, that are defined in reference to start point of $N_{a,1}$.$W_{a,0}$ and $W_{a,2}$ indicate the window area defined in the user interface for the background region(the region without any pulse). The same definitions apply to the analogous quantities for channel B.

do this calculation, we use the help of the on-board power PC of the FPGA

$$\hat{S}_{\mathrm{y}} = I_{a1} - \frac{1}{2}\left(\frac{I_{a0}W_{a1}}{W_{a0}} + \frac{I_{a2}W_{a1}}{W_{a0}}\right) \tag{3.3}$$

$$\hat{S}_{\mathrm{x}} = I_{b1} - \frac{1}{2}\left(\frac{I_{b0}W_{b1}}{W_{b0}} + \frac{I_{b2}W_{b1}}{W_{b0}}\right) \tag{3.4}$$

The angle of rotation is equal to the ratio $\hat{S}_{\mathrm{y}}/\hat{S}_{\mathrm{x}}$ which is calculated on on-board power PC. The calculation of the angle of rotation is used for feedback. There are two digital signals generated for positive angle of rotation and negative angle of rotation. There is a user interface program designed to control the gain of the feedback which allow us to change the length of the digital signal which is used later on to control the length of the optical pulse send for optical feedback.

3.3 Performance of the shot-noise limited detector

To investigate the noise behaviour of the real time detection system and compare it to the old detection system performance, we send a series of probe pulses with pulse length of 1 μs and a period of 10 μs into the polarimeter and vary the number of photons per pulse. For each pulse length and photon number, we send a train of 200 pulses and evaluate ϕ. In Fig. 3.5, we plot the variance as a function of photon-number for three different scenarios where we measure the performance of the old detection system (red data points), the real time detection system without attenuation of any of the channels (green data points) and the real time detection system with 11 db attenuation on channel A (blue data points). I elaborate more on why we applied attenuation on channel A. As I have mentioned in the proceeding section 3.2, PIMAT has a user interface which allows us to set different parameters of the system, moreover it allows us to see the raw data of channel A and channel B in a visualized form. We had to attenuate the electronic signal with the fixed attenuation of 11 dB to avoid saturation of ADC on the channel A, in order to perform the measurement for higher numbers of

photons. The signal that is sent to channel A is the signal coming from an amplified detector, the DSP has an integrated low-pass filter that cuts off the high frequencies. For all of these cases we clearly see two different scalings, one for the low number of photons where the variance shows no dependence on photon number and represents the electronic noise level of the detector. The second is the linear scaling of the measured variance vs photon number. The result shows shot noise limited behaviour above 10^5 photon-number for the old detection system and real time detection system with 11 dB attenuation.

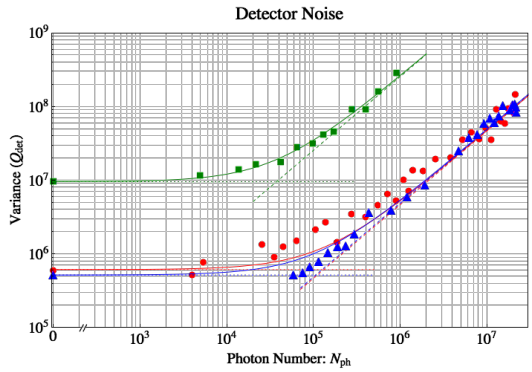

Figure 3.5: Variance of detector signal as a function of photon-number. The pulse length is 1 μs. The dynamic range of shot-noise limited behaviour for polarimeter detection system (red data points), real time detection system with 11 db attenuation on channel B (blue data points) and real time detection system without any attenuation (green data points) are $(0.5 \times 10^5 - 2 \times 10^8)$, $(10^5 - 2 \times 10^8)$ and $(2.8 \times 10^4 - 3 \times 10^6)$ respectively.

3.4 Optical pumping

The feedback scheme to manipulate the atomic spin is based on incoherent feedback via optical pumping. Optical pumping is a standard technique for preparing the quantum states of atoms. It is based on interaction with reso-

nanat light of particular polarization which according to the selection rules induces only specific transitions. The method has been pioneered by Kastler [49] in the 1950s. If the polarization of the optical pumping light is set accordingly, various distribution of the atomic population and coherences can be produced. Many experiments in atomic physics benefit from the ability of preparing atoms in a well defined and specific internal states. Within the many possible example, we can point out the examples of sensitive magnetometers [50, 51], magnetic-field-insensitive clock transition[52] that are used for atomic clocks.

For most of the applications mentioned above, the process of optical pumping will prepare the atoms in a specific state. The process is based on scattering from one internal state to another state, until it reaches to a "dark" state which is uncoupled from other states. Preparing the quantum state of the atomic state as precisely as the quantum mechanical uncertainty allows requires two conditions. First, it requires a single frequency mode radiation with all classical intensity fluctuations well below the photons shot noise. This is easily achievable with external-cavity lasers technology. Second, the polarization of this radiation must be filtered through a good polarizer. In order to get a uniform optical pumping effect in the transverse direction of the cloud, we use a collimated optical pumping beam with a beam waist which is larger than the beam waist of the atomic cloud. In this scenario, the optical pumping has a uniform intensity in the transverse direction of the atomic cloud. We discuss now the optical pumping set up that we have developed for that feedback task. This optical pumping is intended to be used as an incoherent feedback system. Coherent feedback, for example rotation under a controlled magnetic field, has previously been applied to spin ensembles [53, 54]. But coherent rotations necessarily preserve the volume of phase space, for example a magnetic field simply rotates the state on the Bloch sphere. In contrast, incoherent feedback can change the distribution of the population through excitation and relaxation and will make it possible to get to the center of the Bloch sphere where we get a higher phase-space density.

The task of this optical pumping is to remove the net polarization of the atoms which are marked by positive or negative ϕ. To remove the offset

polarization, we use two optical pumping beams with z axis as propagation axis of the probe beam. Both of them are collimated and have larger beam waists than the atomic cloud beam waist. One of the beams is propagating along the dipole trap direction and the other one in the contrary direction. To remove the offset polarization of the atoms, two optical pumping beams with different circular polarization are needed. The circularly polarized light is tuned to the $F = 1$ to $F' = 0$ of D_2 line transition of ^{87}Rb . For on

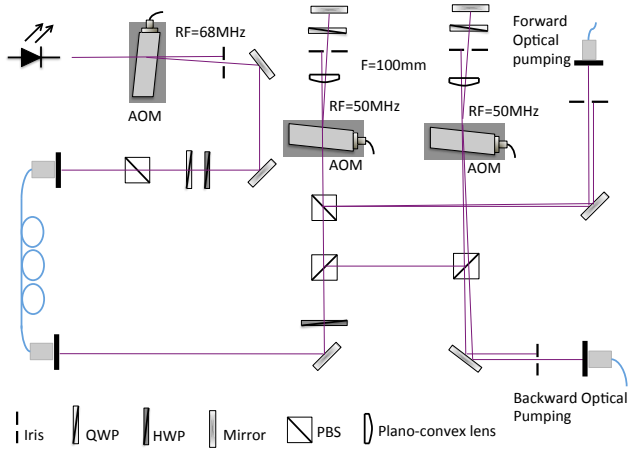

Figure 3.6: Schematic layout of the optics to control the beam power, to generate pulses and to adjust the frequency of the forward and backward optical pumping sources.

resonant optical pumping $F = 1$ to $F' = 0$ transition, the excitation and de-excitation would involve just the $F = 1$ and $F' = 0$ manifold. In this situation there are not so much loss into the $F = 2$ state. However, given that the high optical depth of the atomic sample in the longitudinal direction of the trap, pumping along this direction would be considerably slower. If we want the state to remain permutationally invariant, then the pumping has to be uniform in space. With the shadowing, we will get different polarization at the end versus the centre. To overcome the shadowing effect caused by

strong absorption of the photons in the initial portion of the ensemble and in order to get a more uniform optical pumping along the atomic cloud, we set the optical pumping to be 30 MHz red detuned from $F = 1$ to $F' = 0$ transition. These two optical pumping sources are derived from the repumper laser of the MOT with two AOMs as has been shown in Fig. 3.6.

3.4.1 Shadowing effect

As explained above, the high optical depth of the trap in the optical pumping direction has a disadvantage, in this scenario, the photons are strongly absorbed by only a portion of the cloud and as a consequence the sample is not uniformly illuminated. To have a more uniform optical pumping effect we have used a light source that is detuned from the resonance to the red. For this calculation, I considered that the optical beam has a beam waist much bigger than the beam waist of the atomic cloud. The optical pumping distribution is uniform in the radial direction. So the beam waist of the optical pumping beam does not enter in this calculation. Here we present the study on how by properly choosing the detuning and the beam focusing one might achieve a more uniform illumination. For a cylindrically-symmetric atomic cloud, we can work with the transversal, i.e. radial $r^2 = x^2 + y^2$ and longitudinal z coordinates. For the density, we assume a Gaussian distribution with $1/e^2$ waist w_r in the transverse plane, multiplied by also Gaussian distribution in the z direction with waist w_z. The atomic density distribution for the assumption of the Gaussian distribution in transverse and longitudinal direction is:

$$\rho(r,z) = N_a \frac{2}{\pi w_r^2} e^{-\frac{2r^2}{w_r^2}} \sqrt{\frac{2}{\pi}} \frac{1}{w_z} e^{-\frac{2z^2}{w_z^2}} \tag{3.5}$$

where N_a is the total number of atoms. The transmission of the light intensity as a function of z and r is calculated by integrating the atomic density along the propagation direction, i.e. computing what is known as column density.

$$\frac{I(z,r)}{I_{in}} = e^{-\sigma \int_{-\infty}^{z} \rho(r,\zeta) d\zeta} \tag{3.6}$$

σ, the scattering cross section, is

$$\sigma(\Delta) = \frac{\lambda^2\Gamma^2}{2\pi}\frac{1}{32}\Big[\frac{4}{\Gamma^2/4+\Delta^2} + \frac{5}{\Gamma^2/4+(\Delta-\delta_{01})^2} + \frac{7}{\Gamma^2/4+(\Delta-\delta_{02})^2}\Big] \tag{3.7}$$

where λ is the light wavelength, Γ is the spontaneous emission decay rate and δ_{ij} are the frequency splittings between the hyperfine energy levels $F' = i$ and $F' = j$ of the excited states manifold of ^{87}Rb , which are 72.2 MHz and 228.2 MHz for δ_{10} and δ_{02} respectively. The detuning Δ is referred to the detuning of the optical pumping from $F = 1 \rightarrow F' = 0$ transition.

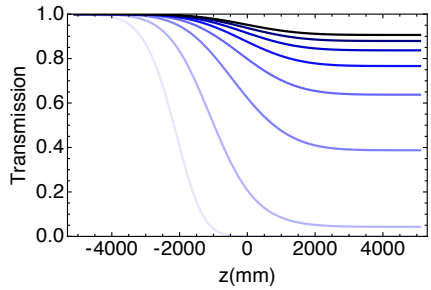

Figure 3.7: Calculated transmission through the atomic cloud as a function of detuning. The transmission is calculated for a Gaussian distribution of the atomic cloud and for optical pumping with the detunings (from bottom to top) of $0\Gamma, ..., 7\Gamma$ to the red of the $F = 1 \rightarrow F' = 0, D_2$ line transition. For further detuning the curve is marked by darker blue colors. Radial waist in this simulation is considered to be 16.4 μm.

We calculate, for the number of atoms $N_a = 10^6$ and the distribution with $w_r = 16.4$ μm and w_z corresponds to the longitudinal FWHM of 3 mm. In the Fig. 3.7, we have shown the transmission through the atomic cloud for different detunings ranged as of the $\Delta = -\{0, 1, 2, 3, 4, 5, 6, 7\}\Gamma$. From what we have discussed above, we can conclude that 30 MHz detuning which we use for our experiments is not the best detuning to completely overcome the shadowing effect, but it allows the 80 percent transmission through the atomic cloud. Given that at further detuning, the chance of excitation will

get diluted and more optical pumping power is needed to produce the same effect. In our case, the choose of the detuning is a trade-off between the number of the photons available at each detuning and the shadowing effect produced at the corresponding detuning and the scattering rate. Since at further detuning the chance of excitation will get lower and we also have access to fewer number of photons, we decided to use 30 MHz detuned light source for optical pumping which correspond to 80 percent of transmission for the spin cooling experiment that is reported in chapter 7. For the other situation where the lower number of photons would be sufficient it would be possible to use even further detuned light source.

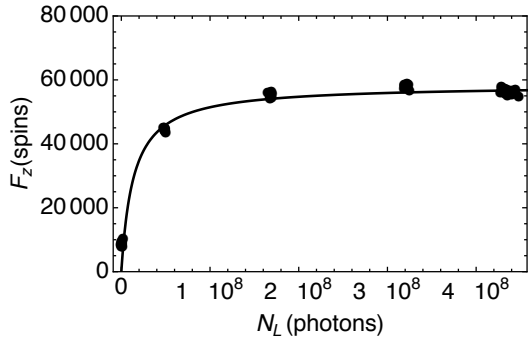

Figure 3.8: The effect of backward optical pumping with light 32 MHz red detuned from $F = 1$ to $F' = 0$ of D_2 line transition of ^{87}Rb . The graph shows the number of spin-flips caused in the atoms for different number of photons. We use the fitting model of $\frac{a(n_l - n_0)}{1 + \frac{n_l - n_0}{n_s}}$ where n_s is the maximum number of photons, $n_l - n_0$ is the number of photons and a is a constant.

3.4.2 The effect of 1 to 0 optical pumping

In this section, we apply the conclusion of the above simulation to measure the effect of optical pumping. The aim of the experiment explained in the following is to get information about the effect of optical pumping on the atomic state. In this experiment, we load the atoms from the MOT into the

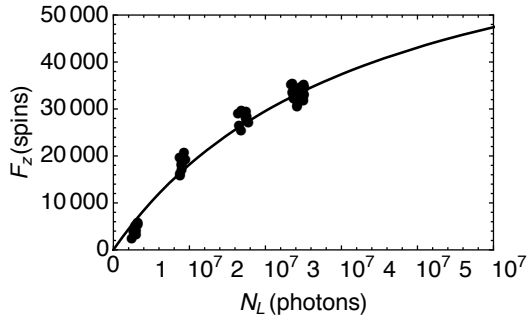

Figure 3.9: The effect of forward optical pumping with light 32 MHz red detuned from $F = 1$ to $F' = 0$ of D_2 line transition of ^{87}Rb . The graph shows the number of spin-flips caused in the atoms for different number of photons.

dipole trap. The magnetic field is set to be a few hundreds of mG along the z axis, to preserve the pumping once generated. The optical pumping is 32 MHz detuned from the $F = 1$ to $F' = 0$ transition of the D_2 line of ^{87}Rb. One beam is sent along the dipole trap propagation direction and will be called "forward optical pumping." Another beam is sent in the counter-propagating direction o the dipole trap beam , and will be called "backward optical pumping." In Fig. 3.9 we measure the number of spin flips caused by the forward optical pumping and in Fig. 3.8 we measure the number of spin flips caused by the backward optical pumping. The dark state of the forward optical pumping is a superposition of $|F = 1, m_f = 1\rangle$ and $|F = 1, m_f = 0\rangle$ and the dark state of the backward optical pumping is a superposition of $|F = 1, m_f = -1\rangle$ and $|F = 1, m_f = 0\rangle$. In our model, we fit the data that is F_z as a function of the number of photons and we used the fitting model of

$$F_z = \frac{a(n_l - n_0)}{1 + \frac{n_l - n_0}{n_s}} \tag{3.8}$$

where n_s is the maximum number of photons, $n_l - n_0$ is the number of photons and a is a constant.

3.5 The backward optical pumping set-up

In order to bring the light source prepared for backward optical pumping to the atomic ensemble, we built an opto-mechanical system in the form of a periscope as shown schematically in Fig. 3.10. We used a Galilean telescope at the beginning of the path to maximize the mode matching of this optical pumping beam to the atomic cloud. The first PBS in the path serves to clean the polarization, which is followed by a quarter-wave plate(QWP) to adjust the ratio of the number of photons that are going to the reference photodiode and the number of photons going to the atoms. The HWP and QWP are used to set the polarization of the photons to circular polarization. Later on the beam is coupled to the atomic sample after passing through two dichroic mirrors that are used to direct the dipole laser to the beam dump. Due to existence of these mirrors in the path, we have a significant loss of the photons that are sent to the atoms. The beam during transmission through the dichroic mirrors splits into two beams. Beam A has 88 percent of the total transmitted power and beam B has 12 percent of the total transmitted power. Beam A is overlapped to the atomic cloud.

3.5.1 Illumination set-up of the absorption imaging and optical pumping from the side

In order to have a more stable system, all the light sources used for various tasks of optical pumping or probing are coupled into the fibers and are brought to the trap position using the polarization-maintaining fibers. In the following I will explain the illumination setup of the absorption imaging system which we use also to do optical pumping from the side. The schematic of the setup is shown in Fig. 3.11. The setup consists of two optical paths, path A is designed to transmit the horizontal polarization which can be transformed to left circular polarization using a wave plate and path B is

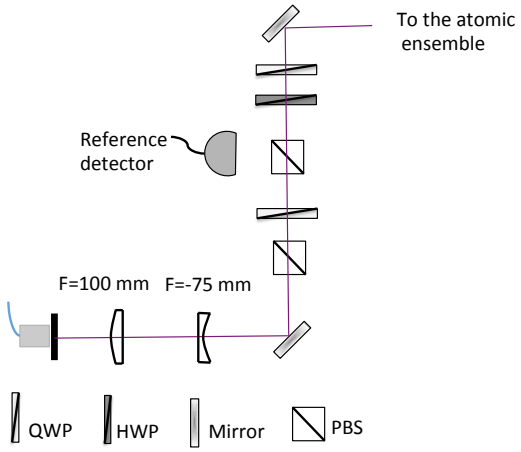

Figure 3.10: Output set-up of the backward optical pumping.

designed to illuminate with vertical polarization which can be transformed to right circular polarization by inserting a QWP in the path. These two beams are overlapped using a polarizing beam splitter. In order to match these beams to the atomic cloud distribution, we insert a Galilean telescope of a Plano-Concave Cylindrical Lens with focal length of $f_1 = -20$ mm and a Plano-Convex Round Cylindrical Lens with focal length of $f_2 = 100$ mm. The input beams to the telescope are collimated beams with Gaussian profile and FWHM of 2mm. This configuration of the telescope permits $M = -\frac{f_2}{f_1} = 5$ times magnification in the horizontal axis. After passing through the telescope, the beams stay collimated with Gaussian profile with a FWHM of 10mm in the horizontal axis and FWHM of 2mm in the vertical direction. To get a stable optical pumping/illumination system, the setup is designed to be fixed on a pillar. The systems is mounted on an adaptor which is used to fix the cage system on a XYZ translation stage.

In order to the detect the atomic state, we use a linearly polarized probe and we measure the rotation of the angle that polarization experiences due to interaction with the atoms. This rotation angle is proportional to the

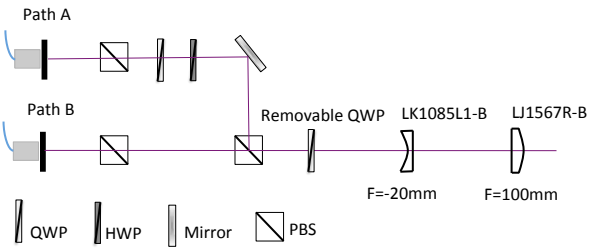

Figure 3.11: Schematic of the illumination set-up of the absorption imaging system.

collective spin of the atoms.

3.6 G_1 measurement

The interaction between light and matter presents in many optical process and applications. One important feature of this experiment is the strength of the coupling between photonics and atomic systems. Despite of the conceptual simplicity, experiments with strong, controlled interactions are hard to achieve. The interaction probability between a single atom and optical photons focused is normally quite weak. To enhance the light-matter interaction, one approach is placing the atom in a high-finesse cavity, taking advantage of the large number of round trips photon makes between the cavity mirror[55, 56]. The other approach is to use a large ensemble of the identical atoms in order to reach a high optical depth.

The coupling constant G_1 in our system is defined as per-atom rotation of the probe light polarization. In order to measure G_1, we use a completely polarized atomic spin state along the propagation direction of the probe light. In terms of atomic operators this corresponds to $\langle \hat{F}_z \rangle = N_A$. The per-atom rotation is calculated from the measured rotation angle and the number of atoms by absorption imaging.

$$G_1 = \frac{\phi}{N_A} \tag{3.9}$$

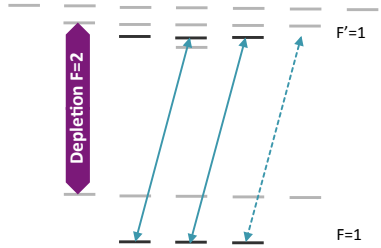

Figure 3.12: The scheme of optical pumping and optical repumping for the measurement of G_1 coupling constant.

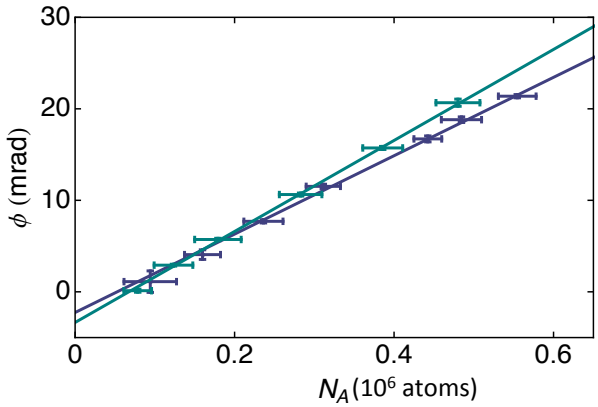

Figure 3.13: Measurement of G_1 coupling constant. The green data points refer to Faraday rotation measured by the Horizontally polarized probe, 700 MHz red detuned from $F' = 0$ of D_2 line transition of ^{87}Rb for different number of atoms. The green line is the linear fit to the data which provide the $G_{1\mathrm{H}} = 4.28 \times 10^{-8}$. The same measurement performed with vertically polarized light is shown as purple data points. The extracted $G_{1\mathrm{V}}$ is 4.45×10^{-8} . Mean G_1, is coupling constant for dual polarization is 4.38×10^{-8}.

where the rotation angle in the Poincare sphere is defined as $\phi = \langle \hat{S}_{\mathrm{y}}^{out} \rangle / \langle \hat{S}_{\mathrm{x}}^{in} \rangle = G_1 N_A$, assuming the input light is completely polarized along the vertical direction, i.e., $\langle \hat{S}_{\mathrm{x}}^{(in)} \rangle = N_L/2$ and $\langle \hat{S}_{\mathrm{y}}^{(in)} \rangle = 0$. The number of atoms is determined using absorption imaging. For the experiment we load atoms into the dipole trap. The ensemble is polarized by illuminating atoms along the quantization axis with circularly polarized light, which is resonant to transition $F = 1 \rightarrow F' = 1$. A small guide field along the z direction defines the quantization axis and prevents the depolarization of the state through stray magnetic fields. To avoid losing atoms into $F = 2$ ground state during the optical pumping process, the ensemble is illuminated with circular polarized light that is resonant to transition $F = 2 \rightarrow F' = 2$, through the path of the MOT beams. We then measure the polarization rotation of the vertically and horizontally polarized light along the trap axis in the balanced polarimeter. In this experiment the detuning of the probe laser is 700 MHz to the red from $F' = 0$ of D_2 line transition of ^{87}Rb. The data related to H and V polarization are shown in Fig. 3.13. $G_{1\mathrm{H}}$ is 4.28×10^{-8} rad/atom and $G_{1\mathrm{V}}$ is 4.45×10^{-8} rad/atom.

3.7 G_2 measurement

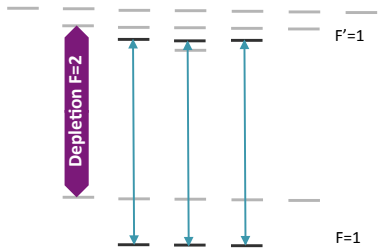

Figure 3.14: The scheme of optical pumping and optical repumping for the measurement of G_2 coupling constant.

In previous section, I described the measurement that we performed to measure G_1 coupling constant. We now describe the details of measuring

the G_2 coupling constant. In order to measure G_2, the ensemble is polarized by illuminating atoms from the side with linearly polarized light, that is resonant to transition $F = 1 \rightarrow F' = 1$. A small guide field of about 100 mG along the x direction prevents depolarization of the state through stray magnetic fields. To avoid losing atoms into $F = 2$ ground state during the optical pumping process, the ensemble is illuminated with circular polarized light which is resonant to the transition $F = 2 \rightarrow F' = 2$, through the path of the MOT beams. The magnetic field also defines the quantization axis. The linear polarization of the optical pumping is parallel to the quantization axis which results in a Π polarization as shown in Fig. 3.14. Since the transition from $|F = 1, m_f = 0\rangle$ to $F' = 1, m_{f'} = 0\rangle$ is forbidden, the dark state of this optical pumping would be $|F = 1, m_f = 0\rangle$ in x quantization axis that is equivalent to $\hat{J}_{\mathrm{x}}$ polarized state in z quantization axis. We then measure

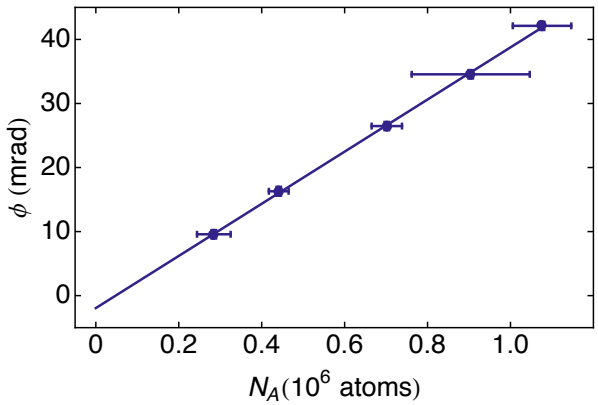

Figure 3.15: G_2 measurement at, circular probe 190 MHz detuning from $F = 1 \rightarrow F' = 0$ transition. The measurement result in G_2 of 4.05×10^{-8} radians per atom.

the polarization rotation of a circularly polarized light along the trap axis in the balanced polarimeter. In this experiment, the detuning of the dispersive probe laser is 190 MHz to the red from $F' = 0$ of D_2 line transition of ^{87}Rb .

The dispersive probing of the collective alignment is calibrated against a measurement of the atom number made by absorption imaging. We measure $G_2 = 4.05 \times 10^{-8}$ radians per spin. G_2 value is extracted from the linear fit to the data in Fig. 3.15.

3.8 Three-axis QND measurement

We have developed a technique for three-axis QND measurement. Traditionally in our lab, we measure the collective spin $\hat{F}_z$ by paramagnetic Faraday rotation probing with 1μs pulses of linearly polarized light. To access sequentially $\hat{F}_x, \hat{F}_y$ and $\hat{F}_z$, we use a combination of coherent control and QND measurement. In this scenario, **F** precesses about a magnetic field (**B**) along the direction [111] making all components accessible to measurement through stroboscopic probing. Faraday rotation gives a high-sensitivity measurement of $\hat{F}_z$. To access $\hat{F}_x$ and $\hat{F}_y$, we apply a static magnetic field of B of few tens of mG along [111] axis to induce $\hat{F}_z \rightarrow \hat{F}_x \rightarrow \hat{F}_y$ precession, and probe at $T_L/3$ intervals, where T_L is the Larmor period as shown in Fig. 3.16. We measure the collective spin components $\hat{F}_i$ with 1µs long pulses of linearly polarized light with on average N_L photons per pulse at a detuning of about 1 GHz to red of the $F = 1 \rightarrow F' = 0$ transition. A shot-noise-limited balanced polarimeter detects $\hat{S}_y^{(out)}$ while a reference detector before the atoms measures $\hat{S}_x^{(in)}$.

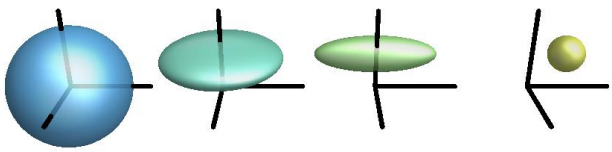

Figure 3.16: Schematic of three-axis QND measurement on a thermal spin state. **F** processes about a magnetic field (**B**) along the direction[111]. Three consecutive QND measurements are performed at $T_L/3$ intervals to access $\hat{F}_x, \hat{F}_y$ and $\hat{F}_z$ components of angular momentum.

3.9 Thermal spin state preparation

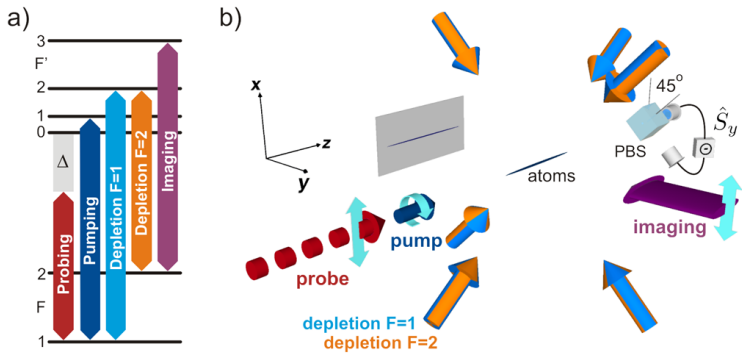

Figure 3.17: (a) Atomic transitions for probing, Pumping and imaging light fields are marked. (b) Atomic ensemble with probing, pumping, and imaging light fields. The polarimeter measures in the 45 basis, i.e., the Stokes component S_y. The figures credits goes to M. Koschorreck [57].

In our trap, we are working with a cold atomic ensemble that is loaded from the magneto optical trap into the dipole trap. The process of cooling can be divided to three stages, the first stage is the cooling in the MOT in the presence of the cooler laser and repumper laser and the gradient of the magnetic field. This stage of cooling will bring the temperature of the atoms to 144μ K. The second stage of cooling is the sub-Doppler cooling to bring the atoms to the lower temperature than what can be achieved with the MOT and to increase the number of atoms in the trap. At this stage we reduce the quadrupole gradient gradually to zero. In the third stage, we allow the atoms to fall into the dipole trap and the atoms which are not cold enough to escape from the trap. The last stage include a waiting time of 400μs, to allow the atoms to thermalize. From the trapping strategy, one would expect that the atoms loaded into the trap are unpolarized. However, what we observed is a small net polarization that exists in the atoms loaded from the MOT into the trap which would be different in day to day operation

scenario.

Here I will describe different strategies that we have used to produce the unpolarized state(Thermal spin state), which in chapter 9, I describe its application in generating macroscopic singlet state.

The thermal spin state is a completely mixed state, with the density matrix:

$$\rho_{\mathrm{TSS}} = \rho_{\mathrm{cms}}^{\bigotimes \mathrm{N_A}} \tag{3.10}$$

where $\rho_{\mathrm{cms}} = \frac{\mathbb{I}_{2F+1}}{2F+1}$ is the density matrix of completely mixed state of a single atom.

To produce this state, we followed different strategies as listed below:

1. Relaxation of the spins via different gradients of the field. Knowing that after dephasing the system will end up in thermal spin state distribution, one candidate method to reach such a mixed spin distribution would be to use the gradient of the magnetic field along and vertical to the trap axis via combination of the eight wires to speed up the relaxation to the thermal spin state.

2. Using a strong gradient of the magnetic field in the presence of a magnetic field few hundreds of mG along [111] direction and weak optical pumping +/- $\hat{F}_z$ direction depend on the measured offset by the QND probe.

3. Multi step sequences of optical pumping and optical repumper pulses through via the MOT beams.

   The first and second strategies, even though they help us to get close to the thermal spin state, they are not sufficient for our purpose. At the end of these procedures, there are some offset polarization left in the collective atomic spin. The most successful strategy for producing thermal spin state has been the last strategy listed above and in the following I explain it in detail.

We actively produce thermal spin states in F = 1 by repeatedly optically pumping atoms from F = 1 to F = 2 and back, using lasers tuned to the

$F = 1 \rightarrow F' = 2$ and $F = 2 \rightarrow F' = 2$ transitions and applied via the MOT beams. Each pumping cycle takes 300 µs. To avoid any residual polarization, we apply bias fields of a few hundreds of mG along z, y, and x during the three back-and-forth cycles. Then the magnetic field is set along the [111] direction. A small final adjustment is made by another round of optical pumping. This optical pumping is applied for 100 µs and followed by the further depletion of the $F = 2$ manifold with a 200 µs pulse of resonant light on the by pumping on the $F = 2 \rightarrow F' = 2$ transition.To check that the atoms in fact end up in F=1 (a significant fraction could remain in F=2 if we are not careful about the powers and durations of the repumping cycles), we use the absorption imaging . In this test, we switch off the repumper during the phase of absorption imaging, to avoid recycling the atoms back to F=1 ground state. We also switch off the QND probe after the thermal spin state preparation step to avoid excitation caused by the probing. The absorption imaging will provide the number of atoms that are in F=2 ground state and for a good TSS preparation, the number of the atoms in the F=2 should not exceed 8×10^4 which is the level of the noise of the absorption imaging measurement.

3.9.1 Thermal spin state measurement and scaling

In order to check that this preparation is providing a state with characteristic of thermal spin state that we desire, we look at the noise scaling of the thermal spin state by varying the number of atoms. The properties of TSS is that in terms of collective spin $\hat{\mathbf{F}}$, it has zero average value, and a noise of

$$\mathrm{var}(\hat{\mathbf{F}}) = \mathrm{V_1 N_A} \tag{3.11}$$

where $\mathrm{var}(\hat{\mathbf{F}})$ is the total variance and $\mathrm{V_1} = \mathrm{F(F+1)}$ is the variance of a single atom.

The result of Thermal Spin State (TSS) scaling with number of atoms (N_A) is shown in Fig. 3.18.

To measure the prepared TSS, we use three-axis QND measurement technique as explained in section 3.8 for a magnetic field of 20 mG amplitude

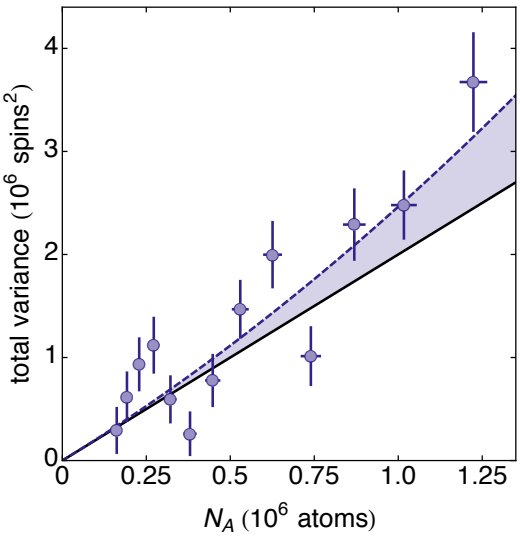

Figure 3.18: Noise scaling of total variance var($\hat{\mathbf{F}}$) of the QND measurement of the atomic spin(blue circles). The black solid line is the expected noise scaling of total variance of TSS versus number of atoms in the trap, which scales as $2N_A$. Dashed line is a quadratic fit, indicating the presence of technical noise in the input atomic state (blue shaded region).

and Larmor period of $T_L = 69.19\mu s$. The probe light with this experiment has $N_L = 8.6 \times 10^7$ photon per pulse at a detuning of 700 MHz to red of the $F = 1 \rightarrow F' = 0$ transition.

3.10 Atom "loss" due to probing

In the process of the probing, some of the atoms will get excited and decay back to the $F = 2$ ground state. Those atoms are much farther from resonance than $F = 1$ atoms, and are effectively lost from the system. To get an order of magnitude, we note that the $F = 1 \rightarrow F' = 0$ transition is closed, and can only return atoms to F=1. In contrast, the $F = 1 \rightarrow F' = 1, 2$ transitions are open and a fraction of the scattering events take the atoms to F=2. We can compare the branching ratios for a detuning of 700 MHz (114 natural linewidths) from the $F = 1 \rightarrow F' = 0$ transition, which is then 773, 930 MHz (126, 152 natural linewidths) from the $F = 1 \rightarrow F' = 1, 2$ transitions, respectively. The $F = 1 \rightarrow F' \rightarrow F = 1$ channel has contributions

$$\frac{1}{(114)^2} S_{10}^2 + \frac{1}{(126)^2} S_{11}^2 + \frac{1}{(152)^2} S_{12}^2 = 2.0 \times 10^{-5} \tag{3.12}$$

where $S_{FF'}$ is the matrix element from single ground state sub level to the levels in a particular F' energy level. The values for S_{10}, S_{11} and S_{12} are $\frac{1}{6}$, $\frac{5}{12}$ and $\frac{5}{12}$ respectively [36] . The $F = 1 \rightarrow F' \rightarrow F = 2$ channel has contributions

$$0 + \frac{1}{(126)^2} S_{11} S_{21} + \frac{1}{(152)^2} S_{12} S_{22} = 5.82 \times 10^{-6} \tag{3.13}$$

where S_{21} and S_{22} are $\frac{1}{2}$ and $\frac{1}{4}$ [36]. These branching ratios favor scattering back into F=1 by a ratio of 3.5 : 1.

The atom loss due to probing can be calculated from 2.18 as has been explained in section 2.2.1. For most of experiments explained in this thesis $\Gamma/2\pi = 6.1$MHz is the natural linewidth of the transition, Δ is the detuning from $F = 1 \rightarrow F' = 0$ transition, $\sigma_0 \equiv \frac{\lambda^2}{\pi}$ and $A = 2.6 \times 10^{-9}$ is the effective atom-light interaction area. Including the branching ratio, the atom loss due

to probing for each pulse of 8.6×10^7 photons at 700 MHz detuning is about 1.5 percent.

4

Background for vector magnetometry experiment

This chapter presents the background material related to the vector magnetometry experiment presented in chapter 5. We present the covariance matrix approach to atomic ensemble, our main theoretical technique for describing light-matter interaction and the theory of the free induction decay and the decoherence due to presence of inhomogeneity of the magnetic field.

4.1 Covariance matrix approach

This approach is valid within Gaussian approximation. Gaussian states can be described by mean values and variances. The ensemble of large number of atoms as the one that we are dealing with, can be described with Gaussian approximation and the evolution of the components operator, $\mathbf{V}$ is fully characterized by its average and by its covariance matrix $\Gamma_{\mathbf{V}}$

$$\Gamma_{\mathbf{V}} = \frac{1}{2}\langle \mathbf{V} \wedge \mathbf{V} + (\mathbf{V} \wedge \mathbf{V})^T \rangle - \langle \mathbf{V} \rangle \wedge \langle \mathbf{V} \rangle \tag{4.1}$$

where $\wedge$ indicates the outer product. Many groups had followed this approach to describe the collective atom and light interaction variable and their interaction including Kraus et al [58], Madsen and Mølmer[59], Hammerer et al[60], Mølmer and Madsen[61], Koschorreck et al[62] and Colangelo et al[40].

In the experiments that are reported in this thesis, there are some experiments that uses the covariance matrix approach and some that use the input-output operator approach.

4.2 Conditional probabilities and conditional variance

In all of the experiments explained in this thesis, we are using the conditional measurement and conditional variance. In one case, we want to predict (retrodict) the magnetic field during an experiment run immediately after (before) the magnetic field measurement. In other case, it is used to quantify how good the measurement scheme is. In chapter 2, we have already defined what is a quantum non-demolition measurement and the characteristics of such measurement. In this part, we will explain the conditional uncertainty and conditional measurement, that is used to define how good has been a QND measurement. For this, we analyze the conditional uncertainty between consecutive pairs of measurements m_1 and m_2.

In the Gaussian approximation, after performing the first measurement the wave function of the measured value will collapse to a smaller Gaussian distribution within the first distribution. Performing the second QND measurement after the collapse of the wave function in the first measurement provides the same output similar to the first measurement within the Gaussian distribution of the first measurement output. The conditional measurement that analyze the second measurement based on the output of the first measurement, will provide information about the projective nature of QND measurement. This concept has been described by successive measurements in quantum theory.

The theory of successive measurement was initiated by von Neumann 's theory [63] , via his 'projection postulate'. Based on this postulate, if an ensemble of systems in state ρ is subjected to a measurement of the observable A, then the post measurement state (unnormalized) of the subensemble of systems, which have given outcomes in subset E of the real line,

is given by

$$\rho' = \sum_{\lambda_i \in E} P_i \rho P_i. \tag{4.2}$$

In particular, the state of the sub ensemble of those systems which have given the outcome λ_i is $P_i \rho P_i$ and the state of the entire ensemble, irrespective of the outcome after the $A-$measurement will be

$$\rho' = \sum_i P_i \rho P_i \tag{4.3}$$

which correspond to the mixed state in general. A more detailed discussion can be found in [64]. In this situation, if the measurement of the observable A in a state ρ, is found to lie in the set E, then an immediate repetition of the measurement will lead to the same result. Based on the projection postulate of von Neumann one can get information on statistical correlation between successive measurements.

4.2.1 Conditional distribution

In a typical calculation using the covariance matrix formalism, most of the transformations of $\mathbf{V}$ and $\Gamma_{\mathbf{V}}$ are due to dynamical processes, e.g. interaction with a magnetic field, light-matter interaction, or decoherence. In contrast, measurement transforms the state through a change in our knowledge of the value of $\mathbf{V}$.

Consider a system described by operators $\mathbf{V} = \mathbf{V}_1 \oplus \mathbf{V}_2$, with a covariance matrix

$$\Gamma = \begin{pmatrix} \Gamma_{11} & \Gamma_{12} \\ \Gamma'_{12} & \Gamma_{22} \end{pmatrix} \tag{4.4}$$

where Γ'_{12} is the transpose of Γ_{12}. For example, $\mathbf{V}_2$ might describe the Stokes operators of a light pulse, while $\mathbf{V}_1$ describes the atomic variables and all the subsequent light pulses. If we measure $\mathbf{V}_2$, what effect does this have on $\langle \mathbf{V}_1 \rangle$ and Γ_{11} ?

Upon obtaining a measurement result $\mathbf{V}_2 = \mathbf{v}_{\text{meas}}$, the following changes

occur, reflecting an update to our knowledge:

$$\langle \mathbf{V}_1 \rangle \rightarrow \langle \mathbf{V}_1 \rangle + \Gamma_{12}\Gamma_{22}^{-}(\mathbf{v}_{\text{meas}} - \langle \mathbf{V}_2 \rangle) \tag{4.5}$$

$$\Gamma_{11} \rightarrow \Gamma_{11} - \Gamma_{12}\Gamma_{22}^{-}\,\Gamma_{12}' \tag{4.6}$$

where A^{-} indicates the generalized inverse, also known as the Moore-Penrose pseudo-inverse of the matrix A. Note that the transformation of Γ_{11} does not depend on the measurement outcome; the change in the covariance matrix is deterministic. The generalized inverse or Moore-Penrose pseudo inverse is the generalization of the inverse matrix. Generalized inverse of A is defined as a matrix A^{-} satisfying all the following criteria:

1. $AA^{-}A = A$
2. $A^{-}AA^{-} = A^{-}$
3. $(AA^{-})^{\dagger} = AA^{-}$
4. $(A^{-}A)^{\dagger} = A^{-}A$.

$A^{\dagger}$ denotes the adjoint of matrix A. It has application in dealing with optimisation problem, with data analysis, with the solution of linear integral equations, etc [65]. The generalized Inverse, allows for solving least square systems, even with rank deficient matrices, in such a way that each column vector of the solution has a minimum norm. In our case, we are dealing with $m \times m$ matrices and the Moore-Penrose pseudo inverse matrix is given by

$$\Gamma^{-} = \begin{cases} \sum_{\mathrm{i}} \lambda_{\mathrm{i}}^{-1} \mathrm{v}_{\mathrm{i}} \wedge \mathrm{v}_{\mathrm{i}} & \text{for} : \lambda_{\mathrm{i}} \neq 0 \\ \lambda_{\mathrm{i}} = 0 & \text{for} : \lambda_{\mathrm{i}} \geq 0 \end{cases}$$

where λ_{i} is the eigenvalue and v_{i} is eigenvector of matrix Γ.

This "update rule" is used in nearly all covariance matrix calculations, and a recipe appears already in the first discussions of the method [59]. The detail of the proof is given in appendix A.

4.3 Conditional variance

The probability of knowing the outcome x_2, given that we know the outcome x_1 is given by bayesian formalism

$$P(x_2|x_1) = \frac{P(x_1, x_2)}{P(x_1)} \tag{4.7}$$

Given a measurement outcome x_1, we want to make the best prediction we can for the second measurement x_2. We define an estimator $\hat{x}_g(x_1) = Ax_1+B$ that estimates the measurement result x_2 from the knowledge of measurement result x_1. An optimal estimator minimizes $|\hat{x}_g(x_1) - x_2|^2$. So the problem is just to find A that minimizes the contribution from fluctuations.

$$\mathrm{var}(\hat{x}_g(x_1) - x_2) = A^2\mathrm{var}(x_1) - 2A\mathrm{cov}(x_1, x_2) + \mathrm{var}(x_2) \tag{4.8}$$

from minimizing the Eq. 4.8 for A, we get $A = \frac{\mathrm{cov}(x_1,x_2)}{\mathrm{var}(x_1)}$. So our best estimator would be

$$\hat{x}_g(x_1) = \frac{\mathrm{cov}(x_1, x_2)}{\mathrm{var}(x_1)}x_1 + B. \tag{4.9}$$

this lead us to the conditional variance equation that is used to quantify the experimental readout noise.

$$\mathrm{var}(Ax_1 - x_2) = \mathrm{var}(x_2) - A^2\mathrm{var}(x_1) \tag{4.10}$$

For most of experiment reported in this thesis, the signal is multi-dimensional. In the following we generalize the concept of conditional variance from scalar measurement to vector measurement. Given a vector measurement result $\mathbf{x}_1$, we want to make the best prediction we can for a second vector measurement $\mathbf{x}_2$. The vectors have dimension N. We define a linear function $\mathbf{x}_g = A\mathbf{x}_1 + B$ which will be our guess. We define the error in terms of a metric (a squared-distance function) $s^2 = (\mathbf{x}_g - \mathbf{x}_2)'C(\mathbf{x}_g - \mathbf{x}_2)$, where C is a positive real matrix (that means the eigenvalues are positive, and the entries are real). This means the matrix is real Hermitian, i.e., symmetric.

We want to minimize the mean squared distance

$$\langle S^2 \rangle = \langle (A\mathbf{x}_1 + B - \mathbf{x}_2)' C (A\mathbf{x}_1 + B - \mathbf{x}_2) \rangle \tag{4.11}$$

The constant contribution is minimized by $B = \langle A\mathbf{x}_1 - \mathbf{x}_2 \rangle$, so the problem is just to find A that minimizes the contributions from fluctuations. From now on, we assume that $B = \langle \mathbf{x}_1 \rangle = \langle \mathbf{x}_2 \rangle = 0$.

By proper choice of basis, we can reduce this to N^2 independent minimizations. We first identify the eigenvectors of C, as $\mathbf{v}_s^{(i)}$, so that $C = \sum_i c_i \mathbf{v}_s^{(i)} \wedge \mathbf{v}_s^{(i)}$. This gives

$$\langle S^2 \rangle = \sum_i c_i \langle |\mathbf{v}_s^{(i)} \cdot (A\mathbf{x}_1 - \mathbf{x}_2)|^2 \rangle \tag{4.12}$$

The proper basis for $\mathbf{x}_1$ is the eigenvectors $\mathbf{v}_1^{(j)}$ of the covariance matrix Γ_{x1}. Note that projections onto the eigenvectors $\mathbf{v}_1^{(j)} \cdot \mathbf{x}_1$ are uncorrelated, because Γ_{x1} diagonal in this basis. We write A in a mixed basis

$$A = \sum_{ij} A_{ij} \mathbf{v}_s^{(i)} \wedge \mathbf{v}_1^{(j)} \tag{4.13}$$

we see that

$$\begin{aligned} \langle S^2 \rangle &= \sum_i c_i \left\langle (\sum_j A_{ij} \mathbf{v}_s^{(j)} \cdot \mathbf{x}_1 - \mathbf{v}_s^{(i)} \cdot \mathbf{x}_2)^2 \right\rangle \\ &= \sum_{ij} c_i \left\langle (A_{ij} \mathbf{v}_s^{(j)} \cdot \mathbf{x}_1 - \mathbf{v}_s^{(i)} \cdot \mathbf{x}_2)^2 \right\rangle \end{aligned}$$

Note that we can only pass from the first line to the second because of our choice of basis for $\mathbf{x}_1$: the elements $\mathbf{v}_1^{(j)} \cdot \mathbf{x}_1$ are uncorrelated, so the different contributions simply add in quadrature. Eq. **??** describes N^2 independent optimization problems for the elements A_{ij}, each of which has the usual 1D

solution

$$A_{ij} = \frac{\mathrm{cov}(\mathbf{v}_s^{(i)} \cdot \mathbf{x}_2, \mathbf{v}_1^{(j)} \cdot \mathbf{x}_1)}{\mathrm{var}(\mathbf{v}_1^{(j)} \cdot \mathbf{x}_1)} \tag{4.14}$$

If we substitute back into Eq. 4.13, we find

$$A = \sum_{ij} \frac{\mathrm{cov}(\mathbf{v}_s^{(i)} \cdot \mathbf{x}_2, \mathbf{v}_1^{(j)} \cdot \mathbf{x}_1)}{\mathrm{var}(\mathbf{v}_1^{(j)} \cdot \mathbf{x}_1)} \mathbf{v}_s^{(i)} \wedge \mathbf{v}_1^{(j)} \tag{4.15}$$

We use the fact that $\Gamma_{\mathbf{x}_1}^{-1} = \sum_j \mathrm{var}(\mathbf{v}_1^{(i)} \cdot \mathbf{x}_1)^{-1} \mathbf{v}_1^{(j)} \wedge \mathbf{v}_1^{(j)}$, and we arrive to a very simple formula analogous to the 1D expression:

$$A = \Gamma_{\mathbf{x}_2,\mathbf{x}_1} \Gamma_{\mathbf{x}_1}^{-1} \tag{4.16}$$

where $\Gamma_{\mathbf{x}_2,\mathbf{x}_1}$ is the generalized covariance matrix for $\mathbf{x}_1$ and $\mathbf{x}_2$.

4.4 Theory of free induction decay

In chapter 5, we will discuss the experimental method that uses the atoms to get information about all components of the magnetic field. Here we describe more in detail the theory behind the free induction decay signal obtained from atoms.

The Hamiltonian that we are going to describe in this part, is the interaction Hamiltonian between **F** and **B**, where **F** is the angular momentum operator and **B** is the magnetic field vector. In the absence of the magnetic field, the magnetic sublevels that determine the angular distribution of the electron wave function are degenerate. In presence of an external magnetic field, their degeneracy is broken. The Hamiltonian describing the atom-magnetic field interaction is given by

$$H_B = \frac{\mu_B}{\hbar}(g_s \mathbf{S} + g_l \mathbf{L} + g_I \mathbf{I}) \cdot \mathbf{B} \tag{4.17}$$

In the above equation μ_B is the Bohr magneton and the g_s, g_L and g_I are respectively the electron spin, electron orbital, and nuclear g-factors. If the energy shift due to the magnetic field is small compared to the fine-structure

splitting, the atom-magnetic field interaction Hamiltonian becomes

$$H_B = \mu_B g_F \mathbf{F} \cdot \mathbf{B} = \gamma \mathbf{F} \cdot \mathbf{B} \tag{4.18}$$

and will cause the coherent evolution of the density matrix where γ is the gyromagnetic ratio, $\mathbf{B}$ and $\mathbf{F}$ correspond to magnetic field vector and angular momentum vector. The interaction of the atoms with the magnetic field is linear, so the precession by large angles can be described in a single step. At the same time, inhomogeneities in the magnetic field introduce dephasing which we describe in this section.

The effect of the interaction of the atoms with the magnetic field can be described by unitary matrix as has been described in [40]. Since the trap is elongated along z direction, the main component of the gradient of the magnetic field affecting the atoms is the gradient along Z direction. Hence, we describe $\mathbf{B}(z)$ as $\mathbf{B}_0 + \mathbf{B}_1(z)$. Local rotation under $\mathbf{B}(z) = \mathbf{B}_0 + \mathbf{B}_1(z)$ can be described by unitary operator

$$U(z,t) = \exp[i\gamma t B(z) \hat{f}_{\mathbf{B}}(z)] \tag{4.19}$$

where $\hat{f}_{\mathbf{B}}(z)$ is the component of $\hat{\mathbf{F}}$ parallel to the local field. We note that $\hat{f}^{n+2}_{\mathbf{B}}(z) = \hat{f}^{n}_{\mathbf{B}}(z)$ which is true for any $F = 1$ spin component. So that a Taylor expansion of U gives

$$U(z,t) = 1 + \hat{f}_{\mathbf{B}}(z) \sin(\gamma |B(z)| t) + \hat{f}^2_{\mathbf{B}}(z)[\cos(\gamma |B(z)| t) - 1]. \tag{4.20}$$

The evolution of operators $\hat{\mathbf{f}}(z)$ that describe an atom at position z can be obtained from Heisenberg equations of motion and the commutation relation of equation (2.7) which lead to equation

$$\frac{d}{dt}\hat{\mathbf{f}}(z) = -\mu_B g_F |\mathbf{B}(z)| A_{B_0} . \hat{\mathbf{f}}(z) \tag{4.21}$$

where

$$A_{B_0} = \begin{pmatrix} 0 & -\hat{B}_z & \hat{B}_y \\ \hat{B}_z & 0 & -\hat{B}_x \\ -\hat{B}_y & \hat{B}_x & 0 \end{pmatrix}. \tag{4.22}$$

4.4.1 Decoherence and dephasing mechanism due to magnetic field inhomogeneity

The main decoherence mechanism in the experiment described in chapter 5, is dephasing , i.e. differential precession due to field inhomogeneity. The detailed description of the dephasing effect can be found in [40].

In the language of magnetic resonance, we expect longitudinal relaxation to be much slower than transverse relaxation due to field inhomogeneity. Expanding the field as $\mathbf{B}(z) \approx \mathbf{B}_0 + (\mathbf{B}'_{\parallel} + \mathbf{B}'_{\perp})z + O(z^2)$, where z is the axial coordinate (with the origin at the centre of the cloud), $\mathbf{B}_0$ is the homogeneous part of the field and $\mathbf{B}'_{\parallel} + \mathbf{B}'_{\perp}$ are the inhomogeneous part of the field, $\mathbf{B}'_{\parallel}$ is parallel to $\mathbf{B}_0$ and $\mathbf{B}'_{\perp}$ is perpendicular. The effect of $\mathbf{B}'_{\parallel}$ is to change $|\mathbf{B}|$ and thus the precession frequency, causing a deviation from the behaviour under $\mathbf{B}_0$ that accumulate with time. In contrast, $\mathbf{B}'_{\perp}$ principally changes the direction of the parallel component of $\mathbf{F}$ and produces a non-accumulative effect.

Considering the field to first order in z, and integrating over the spatial distribution of atoms, described by the linear density $\rho(z) = L/\pi(z^2 + L^2)$, where $L \approx 48\mu$m is the full-width half-maximum (FWHM) extent of the ensemble, we find the standard result

$$\mathbf{F}(t) \quad = \quad \int dz \rho(z) \exp(\gamma_F t |\mathbf{B}(z)| A_{B_0}) \mathbf{f}(0) \tag{4.23}$$

$$\mathbf{F}(t) = [I + A_{B_0}^2]\mathbf{F}(0) + e^{-L\gamma_F |\mathbf{B}'_{||}| t}(A_{B_0} \sin\omega_0 t - A_{B_0}^2 \cos\omega_0 t)\mathbf{F}(0) \tag{4.24}$$

where $I + A_{B_0}^2$ describes a projector onto the direction of $\mathbf{B}_0$. The second term describes a decaying oscillation of the transverse components. The Free

Induction Decay (FID) on $F_z(t)$ for different initial states is:

$$\begin{aligned} F_z(t) &= \frac{1}{|B|^2}\Bigg(\left[B_x B_z \left(1-\cos(\gamma|B|t)e^{-t/T_2}\right) + B_y|B|\sin(\gamma Bt)e^{-t/T_2}\right] F_x(0) \\ &+ \left[B_y B_z \left(1-\cos(\gamma|B|t)e^{-t/T_2}\right) + B_x|B|\sin(\gamma Bt)e^{-t/T_2}\right] F_y(0) \\ &+ \left[B_z^2 + [B_x^2+B_y^2]\cos(\gamma|B|t)e^{-t/T_2}\right] F_z(0)\Bigg) \end{aligned} \tag{4.25}$$

where the transverse time $T_2 = 1/L\gamma|B'_{||}|$.

5

Vector magnetometry

Atoms are very sensitive to magnetic fields. This property makes them a suitable candidate to be used as a highly sensitive magnetometer. But is also means that experiments such as spin squeezing and spin singlet generations require a good control of the magnetic field. In our experiments we have used atoms as a sensor to probe the magnetic field in the atomic trap. By near-resonant Faraday rotation we record the free-induction decay following optical pumping to obtain the three field components and one gradient component. This technique can be used for fast three- axis optical magnetometry. A single measurement achieves shot-noise limited sub-nT sensitivity in 1ms, with transverse spatial resolution of $\sim$20 μ m.

5.1 Background

Control of magnetic fields is critical to many applications, for example high-sensitivity instruments [66] and atomic physics experiments [67]. Hot-atom optical magnetometers [68] offer sub-fT sensitivity at the cm scale [68] and sub-pT at the mm scale [69]. Cold atom magnetometers have demonstrated 10 pT gradient sensitivity at the 10 µm scale [70, 71] and 100 pT gradient sensitivity at the 3 µm scale. [72] A single-ion narrow-band (2×10^{-3} Hz) magnetometer [73] showed 10 pT sensitivities. Many of these systems are designed for sensing of one field or gradient component. In contrast, precise control of fields requires simultaneous knowledge of all field components and possibly gradients as well. Recent work with hot-atom magnetometers has

demonstrated three-axis sensing and control with nT precision at cm scales, [74, 75] while a three-axis modulated cold-atom magnetometer has shown nT sensitivity at 300 μm scales [76].

Here we demonstrate sub-nT sensitivity at 50 μm length-scale in a cold-atom magnetometer employing near-resonant Faraday rotation probing [41]. The instrument gives three-axis field information plus one gradient component, obtained by free-induction decay (FID) after optical pumping. A full measurement requires 1 ms, and can be repeated with zero dead-time, allowing high-bandwidth recording and control of the vector field. No external magnetic fields need be applied, so the technique can be used for real-time monitoring during field-sensitive processes. Our implementation is shot-noise limited and we give explicit expressions for its shot-noise-limited sensitivity.

5.2 Method

The experiment is shown schematically in Figure 5.1(a). An ensemble of atoms is held in an elongated optical trap, and subject to an unknown field **B**. The atoms are first optically pumped along the z direction, so that the collective atomic spin **F** achieves the value $(0, 0, F_z(0))$, and then allowed to precess around **B**. Off-resonance Faraday-rotation probing measures the rotation angle $\theta = GF_z$, where G is a coupling constant, known from independent measurements [41]. We observe the FID signal [77]

$$\theta_1(t) = \frac{G}{|B|^2}\left[B_z^2 + [B_x^2 + B_y^2]\cos(\gamma|B|t)e^{-t/T_2}\right]F_z(0), \tag{5.1}$$

where $\gamma = \mu_B g_F/\hbar$ is the gyromagnetic ratio, μ_B is the Bohr magneton, g_F is the Landé factor, and $\hbar$ is Planck's constant. The transverse relaxation time $T_2 = 1/(L\gamma|B'_\parallel|)$ is due to the field-parallel gradient component $B'_\parallel \equiv \partial|B|/\partial_z$, and a Lorentzian distribution (full-width at half-maximum L) of atoms along z, the trap axis [78]. The process is then repeated with the

spins initially polarized $(0, F_y(0), 0)$, to give

$$\theta_2(t) = \frac{G}{|B|^2}\left[B_y B_z\left(1-\cos(\gamma|B|t)e^{-t/T_2}\right) + B_x|B|\sin(\gamma B t)e^{-t/T_2}\right]F_y(0). \quad (5.2)$$

Fitting the composite signal from the two FID measurements gives the three $\mathbf{B}$ components up to a global sign and T_2. The ambiguity can be lifted by applying a known field, if necessary. Representative traces are shown in Figure 5.1(c). Relative to other vector magnetometry techniques, [74, 75, 76] this method is simple both in procedure and in interpretation and requires no applied B-fields, making it attractive for work with field-sensitive systems. [79]

To derive Equations (5.1) and (5.2) we note that the microscopic spin operators evolve as $\mathbf{f}^i(t) = R(z_i, t)\mathbf{f}^i(0)$, where $\mathbf{f}^i$ is the spin of the i'th atom with position z_i and $R(z,t) = \exp[\gamma_F t|\mathbf{B}(z)|A_B]$, where

$$A_B \equiv \begin{pmatrix} 0 & -\hat{B}_z & \hat{B}_y \\ \hat{B}_z & 0 & -\hat{B}_x \\ -\hat{B}_y & \hat{B}_x & 0 \end{pmatrix}, \quad (5.3)$$

is the generator of rotations about $\mathbf{B}$ and $\hat{\mathbf{B}} \equiv \mathbf{B}/|\mathbf{B}|$.

Possible decoherence mechanisms include atomic motions and collisions, tensorial light shifts due to the probe light, and decoherence due to gradient of the field. In our experiment the effect of tensorial term of probe is negligible, since we are far detuned from D_2 transition line and we are using few photons for detection. For the time-scales involved in this experiment, decoherence due to collisions is negligible, whereas dephasing, i.e. differential precession due to field inhomogeneity, typically is not. In the language of magnetic resonance, we expect longitudinal relaxation to be much slower than transverse relaxation due to field inhomogeneity.

Expanding the field as $\mathbf{B}(z) \approx \mathbf{B}_0 + (\mathbf{B}'_\parallel + \mathbf{B}'_\perp)z + O(z^2)$, where $\mathbf{B}'_\parallel$ is parallel to $\mathbf{B}_0$ and $\mathbf{B}'_\perp$ is perpendicular. We note that a change in the magnitude of $\mathbf{B}$ has an accumulating effect on the spin precession, i.e., the

change in $\mathbf{f}$ grows with t. In contrast, a change in the direction of $\mathbf{B}$ has a fixed effect: From the perspective of the measurement, a rotation of $\mathbf{B}$ is equivalent to a rotation of both the initial state and the measured component F_z. For small gradients $\partial_z \mathbf{B} \ll \mathbf{B}/l_{\text{atoms}}$, where l_{atoms} is the length of the cloud, we can ignore $\mathbf{B}'_\perp$. This approximation, along with the fact that $A_B^{n+2} = -A_B^n$, allows us to write

$$R(z,t) \approx \mathbb{I} + A_{B_0} \sin\omega(z)t + A_{B_0}^2[1 - \cos\omega(z)t] \tag{5.4}$$

where $\omega(z) = \gamma_F|\mathbf{B}_0 + z\mathbf{B}'_\parallel|$.

In our trap, we observe an atomic density $\rho(z)$ well approximated by a Lorenzian $\rho(z) = L/\pi(z^2 + L^2)$ where $L \approx 48$ μm is the full-width half-maximum extent of the ensemble. The collective spin $\mathbf{F} \equiv \sum_i f^i$ then evolves as

$$\begin{aligned} \mathbf{F}(t) &= \int dz\, \rho(z) R(z,t)\mathbf{f}(0) && (5.5)\\ &= [\mathbb{I} + A_{B_0}^2]\mathbf{F}(0) && (5.6)\\ &\quad + e^{-L\gamma_F|\mathbf{B}'_\parallel|t}(A_{B_0}\sin\omega_0 t - A_{B_0}^2\cos\omega_0 t)\mathbf{F}(0) \end{aligned}$$

In the first term $\mathbb{I} + A_{B_0}^2$ describes a projector onto the direction of $\mathbf{B}_0$. This is the steady-state polarization. The second line describes a decaying oscillation of the transverse components, i.e., those perpendicular to $\mathbf{B_0}$.

5.3 Experiment

Our experimental apparatus has been described in detail elsewhere. [41] Briefly, we work with ensemble of up to 2×10^5 laser cooled ^{87}Rb atoms in the $F = 1$ hyperfine ground state. The atoms are held in a single-beam optical dipole trap with beam waist 56 μm, which sets the minimum distance at which the field can be measured. The atom cloud itself has 20 μm lateral dimension, defining the transverse resolution. The atoms are probed with μs duration pulses of linearly polarized light at 10 μs intervals, red detuned by 1.5 GHz from resonance with the $F = 1 \rightarrow F' = 0$ transition of the D_2

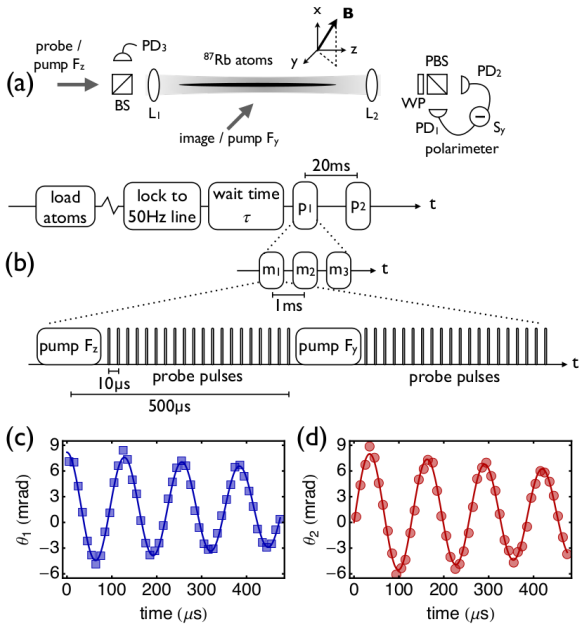

Figure 5.1: (a) Experimental geometry. PD: photodiode; L: lens; BS: beam-splitter; PBS: polarizing beam-splitter; WP: waveplate. (b) Schematic of the experimental sequence: the atoms are initially polarized along F_z via optical pumping and then probed with a sequence of 1 μs long pulses of light at 10 μs intervals. The resulting FID signal is recorded over 500 μs. We then immediately re–polarize the atoms along F_y with an orthogonal optical pumping beam and record a second FID signal. A single shot is thus acquired in 1 ms. We fit the two measurements together to a simple model to extract the magnetic field components B_i. Typical data from a single composite FID measurement are shown in (c) for an initially F_z-polarized state and (d) for an initially F_y-polarized state. For these data the field components extracted from the fit were $\mathbf{B} = (941, 310, 511)$ nT and the coherence time $\tau_c = 1.3$ ms.

line. Each pulse contains on average 10^7 photons. After passing through the atoms, the light pulses are detected by a shot–noise–limited balanced polarimeter[48]. The experimental geometry is illustrated in Fig. 5.1(a).

The detuning and photon number are chosen so that both probe–induced decoherence due to spontaneous emission and the perturbation due to tensorial light shifts are negligible during the measurement cycle. [41] This allows us to use the simple model described by Equations (5.1) and (5.2) to fit the data. We note that the measurement sensitivity could be increased by using more photons and/or reducing the detuning, at the cost of more elaborate data analysis. [41, 7]

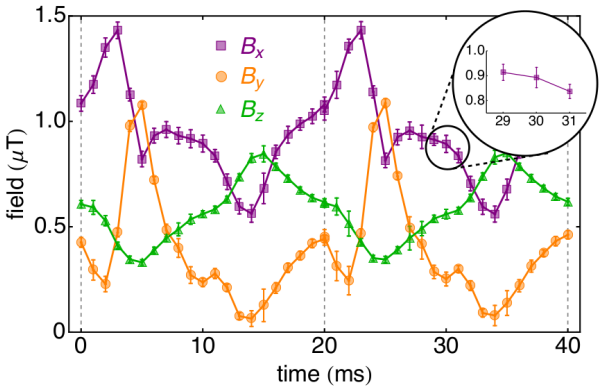

Figure 5.2: Recording of low frequency laboratory magnetic field noise, acquired with one sample point per cycle and varying phase with respect to the 50 Hz signal of the laboratory mains line, as in equivalent–time sampling with a digital oscilloscope. We plot the field components estimated from the three measurement m_j at each point p_i. Inset: Three consecutive measurements are made at each point. Here we plot the B_x component estimated from the three measurements. Error bars are $\pm 1\sigma$ statistical errors.

The initial atomic spin state is prepared via optical pumping with a single 5 μs duration circularly polarized pulse on resonance with the $F = 1 \rightarrow F' = 1$ transition of the D_2 line and propagating either along the trap

axis, i.e. the z-axis, to prepare an F_z-polarized state, or along the y-axis, to prepare an F_y-polarized state. During the optical pumping, the atoms are uniformly illuminated with randomly polarized light on resonance with the $F = 2 \rightarrow F' = 2$ transition of the D_2 line to prevent atoms accumulating the $F = 2$ hyperfine state. A single *composite FID measurement* consists of first preparing an F_z-polarized state and measuring the FID signal over 500 µs, then immediately preparing an F_y-polarized state and again making a FID measurement. A single shot is thus acquired in 1 ms.

To illustrate the technique, we first record the laboratory magnetic noise at the trap, shown in Figure 5.2. Laser cooled atoms are first loaded into the dipole trap during ~ 2 s via a two–stage magneto–optical trap (MOT). A small field is applied with three pairs of Helmholtz coils, and the experiment is triggered on the 50 Hz signal of the laboratory mains line. The field is sampled at a sequence of points p_i at 20 ms intervals, with a variable wait time T before the first point. At each p_i we make three consecutive composite FID measurements m_j, as shown in the inset of Figure 5.2. The entire sequence is repeated 300 times to collect statistics.

The results show good predictability of the field from one cycle to the next, with a typical statistical uncertainty of $\sigma_{B_i} = 40$ nT for each field component. Note that the experiment has no magnetic shielding, so that the observed variance is dominated by magnetic field noise from the laboratory environment. We observe $T_2 \approx 1.5$ ms, which sets a limit on the coherence time and is important for design of future experiments. The FID signals give information about one gradient component, the one along the average field. With three FIDs, with applied bias fields along different directions, we can obtain $\partial\mathbf{B}/\partial z$, all the gradient components affecting the experiment.

5.4 Field Prediction

We are interested in our ability to predict (or retrodict) the magnetic field at a moment shortly after (or before) the magnetic field measurement. This ability determines the precision of corrections for, or control of, the field seen by the atoms. To quantify this precision, we analyze the conditional uncer-

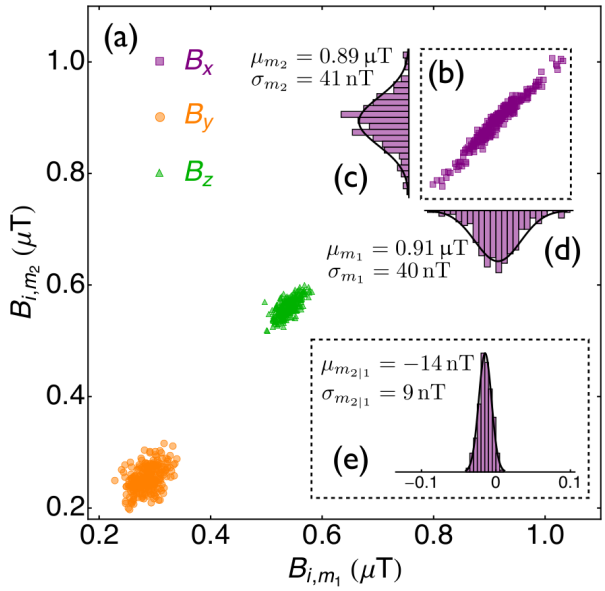

Figure 5.3: (a) Correlation plot of the field components B_i estimated from consecutive measurements m_1 and m_2 of the field. Marginal distributions from the B_x component (b) are shown in histograms (c) and (d). Each has a standard deviation of $\sigma_{B_x} \simeq 40\,\mathrm{nT}$. Solid lines are gaussians with the indicated mean and standard deviation, suggesting that the field noise is approximately normally distributed. The conditional uncertainty of the measurement m_2 given the outcome of measurement m_1 is equivalent to the dispersion of the residuals of a linear regression of m_2 on m_1, shown in inset (e), and has a standard deviation $\sigma_{m_2|m_1} = 9\,\mathrm{nT}$.

tainty between consecutive measurements m_1, m_2 at $T = 29,\ 30$ ms, shown in Figure 5.2, inset. Typical experimental data are shown in Figure 5.3. For a single parameter, the conditional variance is $\mathrm{var}(y|x) \equiv \mathrm{var}(y - ax)$, where the correlation parameter $a \equiv \mathrm{cov}(x, y)/\mathrm{var}(x)$ minimizes the conditional variance. This is equivalent to minimizing the residuals of a linear regression $y = ax + b$, and is illustrated for a single parameter in Figure 5.3(b)–(e). For the data shown, the conditional uncertainty is $\sigma_{m_2|m_1} = 9$ nT.

This analysis is readily extended to multivariate data. If $\mathbf{x}$ and $\mathbf{y}$ are vectors of parameters, with covariance matrices $\Gamma_{\mathbf{x}} \equiv \mathrm{cov}(x_i, x_j)$, and $\Gamma_{\mathbf{x},\mathbf{y}} \equiv \mathrm{cov}(x_i, y_j)$, then the conditional covariance matrix is given by

$$\Gamma_{\mathbf{y}|\mathbf{x}} = \Gamma_{\mathbf{y}} - \Gamma_{\mathbf{y},\mathbf{x}}\Gamma_{\mathbf{x}}^{-1}\Gamma_{\mathbf{x},\mathbf{y}}. \tag{5.7}$$

The matrix of coefficients $A = \Gamma_{\mathbf{x}}^{-1}\Gamma_{\mathbf{x},\mathbf{y}}$ minimizes the mean squared error of the linear regression $\mathbf{y} = A\mathbf{x} + B$. [80]

For the data shown in Figure 5.3, the covariance matrix for the first measurement is

$$\Gamma_{\mathbf{x}} = \begin{pmatrix} 1.60 & 0.21 & -0.14 \\ 0.21 & 0.42 & 0.00 \\ -0.14 & 0.00 & 0.24 \end{pmatrix} \times 10^{-15}\ \mathrm{T}^2. \tag{5.8}$$

The corresponding conditional covariance matrix is

$$\Gamma_{\mathbf{y}|\mathbf{x}} = \begin{pmatrix} 5.6 & -8.0 & -6.0 \\ -8.0 & 36.0 & 1.5 \\ -6.0 & 1.5 & 12.0 \end{pmatrix} \times 10^{-17}\ \mathrm{T}^2. \tag{5.9}$$

This shows strong correlations among the different B components, and it is interesting to diagonalize $\Gamma_{\mathbf{y}|\mathbf{x}}$ to find uncertainties $(\delta B_1, \delta B_2, \delta B_3) = (19.5, 12.0, 3.0)$ nT along the directions $\mathbf{e}_1 = (-0.26, 0.96, 0.11)$, $\mathbf{e}_2 = (-0.41, -0.22, 0.89)$ and $\mathbf{e}_3 = (0.87, 0.18, 0.45)$, respectively. We note that $\mathbf{e}_3$ is nearly the field direction, indicating good predictability for the magnitude of the field. We observe similar results if we analyze the correlation between two measurements p_i at the same phase on different cycles of the 50 Hz mains

line. It should be noted that these results include readout noise, which we now compute.

5.5 Sensitivity

Faraday rotation measurement at or near the shot-noise limit has been demonstrated with a variety of cold atom systems, including released MOTs, [81, 82, 83] optical lattices, [76] and optical dipole traps. [84, 85] Our experiment is shot-noise limited by 10 dB at 10^7 photons/pulse. [6, 86] We compute the shot-noise-limited sensitivity using Fisher Information (FI) theory.[87] For a normally-distributed random variable $\tilde{\theta}$ with fixed variance σ^2 and mean $\theta(\mathbf{x})$, where $\mathbf{x}$ is a vector of parameters, the FI matrix is $\mathcal{I}_{ij} = \sigma^{-2}[\partial_i\theta]\partial_j\theta$, where ∂_a represents $\partial/\partial x_a$. This directly gives the covariance matrix for $\mathbf{x}$ as $\Gamma_{\mathbf{x}} = \mathcal{I}^{-1}$. Due to shot noise, the measured rotation angles are normally distributed with $\sigma_\theta^2 = 1/N_\mathrm{p}$ and means $\theta_{1,2}$ from Eqs. (5.1), (5.2). Also, the FI is additive over independent measurements, so the FI matrix from FID is

$$\mathcal{I}_{ij} = N_\mathrm{p} \sum_{k,l} [\partial_i \theta_l(t_k)] \partial_j \theta_l(t_k). \tag{5.10}$$

where $\mathbf{x} \equiv [B_x, B_y, B_z, T_2, F_z(0), F_y(0)]$ and $\{t_k\}$ are the measurement times.

Considering $\gamma = 2\pi \times 7$ GHz/T for the ground states of ^{87}Rb, and typical values from the data of Figure 5.3: $(B_x, B_y, B_z) = (910, 285, 540)$ nT, $T_2 = 1.48$ ms, $F_z(0) = F_y(0) = 10^5$ spins, $G = 0.89 \times 10^{-7}$ rad/spin and $N_\mathrm{p} = 10^7$ photons, we find the covariance matrix (**B** portion only)

$$\Gamma_\mathrm{SN} = \begin{pmatrix} 1.30 & -2.43 & -1.00 \\ -2.43 & 11.87 & -1.61 \\ -1.00 & -1.61 & 2.57 \end{pmatrix} \times 10^{-17}\ \mathrm{T}^2. \tag{5.11}$$

If we diagonalize Γ_SN we find uncertainties $(\delta B_1, \delta B_2, \delta B_3) = (11.2, 5.6, 0.6)$ nT, along the directions $\mathbf{e}_1 = (0.2, -0.97, 0.14), \mathbf{e}_2 = (0.5, -0.02, -0.86)$ and $\mathbf{e}_3 = (0.84, 0.24, 0.48)$, respectively.

We can now correct the measured field noise of Eq. (5.9) for the measurement noise, to find the field noise $\Gamma_{\mathrm{B}} = \Gamma_{\mathbf{y}|\mathbf{x}} - \Gamma_{\mathrm{SN}}$ of

$$\Gamma_{\mathrm{B}} = \begin{pmatrix} 4.30 & -5.50 & -5.00 \\ -5.50 & 24.00 & 3.10 \\ -5.00 & 3.10 & 9.50 \end{pmatrix} \times 10^{-17}\ \mathrm{T}^2 \tag{5.12}$$

or $\delta B_i \simeq 10$ nT integrated over the kHz bandwidth of the measurement.

The FI analysis also reveals that $\delta F_z(0)$ and $\delta F_y(0)$, the noises in the atomic state preparation, are only very weakly coupled into the estimates of $\mathbf{B}$ and T_2, making the measurement insensitive to, e.g., atom number fluctuations and variation in the optical pumping efficiency.

We have demonstrated a cold-atom magnetometer with sub-nT sensitivity, 20 μm transverse spatial resolution and 1 ms temporal resolution. The instrument gives simultaneous information about the three field components plus one gradient component and requires no additional applied fields, making it very attractive for non-disturbing field monitoring and control. We note that sensitivity can be improved by increasing the number of atoms (in our system a five-fold improvement to 10^6 atoms is readily achievable [41]) and/or the number of photons, although tensor light shifts should be taken into account for larger photon numbers [88, 82, 41].

6

Background for spin cooling experiment

This chapter presents the background material related to the spin cooling experiment presented in chapter 7. I present the different noise terms that must be taken into account due to spontaneous emission, inhomogeneity of the field and the noise added due to optical feedback.

The theory of spin cooling is closely related to quantum control theory. There are two general concepts in quantum control, open-loop control and closed-loop control. Our quantum control problem is in the category of closed-loop controls and more specifically related to quantum feedback control. The goal of such quantum feedback control is to achieve active manipulation and control of quantum system. Some example of experimental demonstration of quantum coherence using quantum feedback control can be found in [89, 90, 56]. The theories that are describing quantum feedback control are either looking at conditional stochastic differential equations which are generalized by incorporating the measurement back-action[91, 33] or following the generalization of a model by Madsen and Mølmer [59] as has been described by Toth and Mitchell [92]. We describe the light-matter interaction via input-output relation approach which we later use to describe the theory of one dimension spin cooling and later generalize it to 3-D spin cooling.

In the following we describe the input-output relation that we have used to study the effect of feedback in the atomic system. In this approach, we describe the feedback mechanism as producing a change in the collective

atomic spin proportional to the measured error signal, which here is the Sy component of a probe pulse. The aim of feedback cooling is to reduce the entropy of the atomic system. In our case, we have tried to reduce the collective atomic spin to zero, starting from a very noisy initial distribution. In order to achieve this goal, we also studied the contribution of noises added due to feedback and decoherence as has been described in this chapter.

6.1 Input-output relation

In input-output relation approach, the evolution of the components of the vector operators $\mathbf{V} = (\hat{F}_\mathrm{x}, \hat{F}_\mathrm{y}, \hat{F}_\mathrm{z}, \hat{S}_\mathrm{x}, \hat{S}_\mathrm{y}, \hat{S}_\mathrm{z})^T$ can be determined from the Heisenberg equation of motion

$$\frac{dV_i}{dt} = \frac{1}{i}[V_i, H_I] \tag{6.1}$$

for the situation where the effective Hamiltonian is the QND Hamiltonian $H_\mathrm{int} = \frac{1}{\tau} G_1 \hat{S}_\mathrm{z} \hat{F}_\mathrm{z}$, the input-output relations for the vector operator $\mathbf{V}$ are as follows:

$$\hat{F}_\mathrm{x}^\mathrm{out} = \hat{F}_\mathrm{x}^\mathrm{in} - G_1 \hat{F}_\mathrm{y} \hat{S}_\mathrm{z}, \qquad \hat{S}_\mathrm{x}^\mathrm{out} = \hat{S}_\mathrm{x}^\mathrm{in} - G_1 \hat{F}_\mathrm{z} \hat{S}_\mathrm{y}, \tag{6.2}$$

$$\hat{F}_\mathrm{y}^\mathrm{out} = \hat{F}_\mathrm{y}^\mathrm{in} + G_1 \hat{F}_\mathrm{x} \hat{S}_\mathrm{z}, \qquad \hat{S}_\mathrm{y}^\mathrm{out} = \hat{S}_\mathrm{y}^\mathrm{in} + G_1 \hat{F}_\mathrm{z} \hat{S}_\mathrm{x}, \tag{6.3}$$

$$\hat{F}_\mathrm{z}^\mathrm{out} = \hat{F}_\mathrm{z}^\mathrm{in}, \qquad \hat{S}_\mathrm{z}^\mathrm{out} = \hat{S}_\mathrm{z}^\mathrm{in}, \tag{6.4}$$

As we can see from the above $\hat{F}_\mathrm{z}$ stays unchanged in this interaction Hamiltonian and it is possible to infer information about $\hat{F}_\mathrm{z}$ with the measurement of $\hat{S}_\mathrm{y}$ components of light. Changes in $\hat{S}_\mathrm{x}$ and $\hat{S}_\mathrm{z}$ components of the light are negligible since $\hat{S}_\mathrm{z}$ would not change due to interaction and $\hat{S}_\mathrm{x}$ is classical value, since the probe light are linearly polarized. So the changes due to measurement on $\hat{S}_\mathrm{x}$ are negligible. It would be enough to measure $\hat{S}_\mathrm{y}$ to get information about $\hat{F}_\mathrm{z}$ component of angular momentum.

6.1.1 Noise added due to spontaneous emission

In the experiments explained in chapters 7,9 there are other decoherence term present during the experiment. One of these noise terms is the noise added to the system due to spontaneous emission events $\hat{\mathbf{N}}^{(S)}$.

For this decoherence term, the process of spontaneous scattering is treated as removal of a fraction η of the N_A atoms, followed by the re-addition of a fraction of the removed atoms, with random polarization incorporated as noise operators $\hat{\mathbf{N}}^{(S)}$.

$$\mathbf{F}^{(1)} = (1-\eta)\mathbf{F}^{(0)} + \hat{\mathbf{N}}^{(S)}. \tag{6.5}$$

$\hat{\mathbf{N}}^{(S)}$ is necessary, otherwise var($\mathbf{F}$) (not just $\langle\mathbf{F}\rangle$) would go to zero for large t, while we expect it rather to go to a thermal state. To estimate the noise contribution due to the spontaneous emission we use the covariance matrix approach similar to the approach of [59, 62] . We assume that the decoherence can be modeled as removing a fraction η of the N_A atoms, scrambling their polarizations, and returning them to the ensemble.

$$F \to F' = (1-\eta)F + N \tag{6.6}$$

where N is by definition uncorrelated with F, i.e., $\mathrm{cov}(F_a, N_b) = 0$ which lead to

$$\Gamma_{F'} \quad = \quad (1-\eta)^2\Gamma_F + \Gamma_N \tag{6.7}$$

The covariance matrix for the spin ensemble is $\Gamma_F = \mathcal{C}(\mathbf{F},\mathbf{F})$ where

$$\mathcal{C}(\mathbf{A},\mathbf{B}) \quad \equiv \quad \frac{1}{2}\langle\mathbf{A}\wedge\mathbf{B} + (\mathbf{B}\wedge\mathbf{A})\rangle - \langle\mathbf{A}\rangle\wedge\langle\mathbf{B}\rangle \tag{6.8}$$

where as usual $\mathbf{F} = \sum_i \mathbf{f}^{(i)}$ summed over the atoms. We assume the exchange symmetry $\langle\mathbf{f}^{(i)}\wedge\mathbf{f}^{(j)}\rangle = \langle\mathbf{f}^{(1)}\wedge\mathbf{f}^{(2)}\rangle$ for all $i \neq j$ and $\langle\mathbf{f}^{(i)}\wedge\mathbf{f}^{(i)}\rangle = \langle\mathbf{f}^{(1)}\wedge\mathbf{f}^{(1)}\rangle$ for all i, i.e., all atoms are statistically equivalent. We then have

$$\Gamma_F \quad = \quad N_A\mathcal{C}(\mathbf{f}^{(1)},\mathbf{f}^{(1)}) + N_A(N_A-1)\mathcal{C}(\mathbf{f}^{(1)},\mathbf{f}^{(2)}) \tag{6.9}$$

which we solve for $\mathcal{C}(\mathbf{f}^{(1)}, \mathbf{f}^{(2)})$ to get

$$\mathcal{C}(\mathbf{f}^{(1)}, \mathbf{f}^{(2)}) = \frac{\Gamma_F - N_A \mathcal{C}(\mathbf{f}^{(1)}, \mathbf{f}^{(1)})}{N_A(N_A - 1)} \tag{6.10}$$

We can now understand the effect of reducing the number of atoms by a fraction η. Instead of summing i and j from 1 to N_A we sum from 1 to xN_A where $x = 1 - \eta$, reducing Γ_F to

$$\begin{aligned}
\Gamma_F &\rightarrow xN_A\mathcal{C}(\mathbf{f}^{(1)}, \mathbf{f}^{(1)}) + xN_A(xN_A - 1)\mathcal{C}(\mathbf{f}^{(1)}, \mathbf{f}^{(2)}) \\
&= xN_A\mathcal{C}(\mathbf{f}^{(1)}, \mathbf{f}^{(1)}) \\
&\quad + xN_A(xN_A - 1)\frac{\Gamma_F - N_A\mathcal{C}(\mathbf{f}^{(1)}, \mathbf{f}^{(1)})}{N_A(N_A - 1)} \\
&= \Gamma_F \frac{x(xN_A - 1)}{N_A - 1} \\
&\quad + \mathcal{C}(\mathbf{f}^{(1)}, \mathbf{f}^{(1)}) \left(xN_A - \frac{x(xN_A - 1)N_A}{N_A - 1} \right) \\
&= \Gamma_F \frac{x(xN_A - 1)}{N_A - 1} + \mathcal{C}(\mathbf{f}^{(1)}, \mathbf{f}^{(1)}) \left(\frac{x(1-x)N_A^2}{N_A - 1} \right)
\end{aligned} \tag{6.11}$$

Dropping terms of order $1/N_A$ and smaller,

$$\begin{aligned}
\Gamma_F &\rightarrow \Gamma_F x^2 + \mathcal{C}(\mathbf{f}^{(1)}, \mathbf{f}^{(1)}) x(1-x)N_A \\
&= \Gamma_F x^2 + \Gamma_{\mathbf{f}} x(1-x)N_A
\end{aligned} \tag{6.12}$$

This accounts for the change in Γ_F due to removing η fraction of atoms. Note that the first term is due to reduction of the size of the system, while the second term is the change due to breaking of correlations. We must also account for the noise of the decohered atoms. We assume they are completely random, and thus add the noise of a thermal state (i.e. variance $f(f+1)/3$ per atom).

$$\Gamma_{F'} \rightarrow \Gamma_F x^2 + \Gamma_{\mathbf{f}} x(1-x)N_A + (1-x)N_A \mathbb{1} \frac{f(f+1)}{3}. \tag{6.13}$$

From this we find

$$\Gamma_N = \Gamma_f x(1-x)N_A + (1-x)N_A \mathbb{1} f(f+1)/3. \tag{6.14}$$

From the above discussion we conclude:

$$\Delta^2 N_i^{(S)} = \Delta^2 f_i^{(1)} \eta(1-\eta)N_A + \eta N_a f(f+1)/3 \tag{6.15}$$

For unpolarized state $\Delta^2 f_i^{(1)} = f(f+1)/3$, which leads to

$$\Delta^2 N_i^{(S)} = N_A \eta(2-\eta) f(f+1)/3 \tag{6.16}$$

for the noise added to due to spontaneous emission events.

6.1.2 Noise added due to field inhomogeneities

As has been described in section 4.4.1, decoherence due to inhomogeneity of the field has the accumulative effect for the inhomogenous field parallel to the direction of the homogenous field $\mathbf{B}_0$. The randomized fraction due to the field inhomogeneities is $\eta_D = 1 - \exp[\theta/(2\pi \mathrm{T_L})]$ which gives noise $\Delta^2 N_i^{(\theta)} = N_A \eta_D (2/3 - \eta_D) f(f+1)/3$.

6.1.3 Noise added due to incoherent feedback

In the incoherent feedback process used in the spin cooling experiment, we first measure the angular momentum $\hat{\mathbf{F}}^{(1)}$ and then we apply an optical pumping feedback proportional to the first measurement.

Here we provide the quantitive numbers for the example of applying the optical feedback to an initial thermal spin state. The variance of each component of angular momentum in this case is equal to $\frac{2}{3}N_A$ where N_A is the number of atoms. Given that the umber of atoms involved in the experiment is 10^6, we get $\mathrm{var}(\hat{F}_\mathrm{z}) = \frac{2}{3} \times 10^6$ and since our initial state is a fully mixed state, the variance of other components is equal to the $\mathrm{var}(\hat{F}_\mathrm{z})$. This corresponds to $\hat{F}_\mathrm{z} \approx 1000$ spins. During the feedback, we apply an optical pumping proportional to the spin value $\hat{F}_\mathrm{z}$. The noise added due to

change of this 1000 spins is equal to $\sqrt{1000} \sim 30$ spins which add a 3 percent noise due to feedback to the total spin and thus it is negligible compared to the amount of noise reduction due to feedback.

6.2 Theory of spin cooling

We use the approach of input-output relation to study the quantum control problem of spin cooling as has been discussed in chapter 7. This quantum control problem includes measurement, rotation and incoherent feedback. To model this experiment, we use multi-step input-output relation.

6.2.1 Feedback cooling in one dimension

Because there will be several steps, we give them numbers, so we have $\hat{S}_{\rm y}^{(0)}, \hat{S}_{\rm y}^{(1)}$, etc. The effect of the measurement on light can be described by:

$$\hat{S}_{\rm y}^{(1)} = \hat{S}_{\rm y}^{(0)} + G_1 \hat{S}_{\rm x} \hat{F}_{\rm z}^{(0)} \tag{6.17}$$

For the effect of measurement on spin, we also considered the noise term due to spontaneous emission caused by measurement.

$$\hat{F}_{\rm z}^{(1)} = (1-\eta)\hat{F}_{\rm z}^{(0)} - i\tau[\mathbf{F}^{(0)}, \hat{F}_{\rm z}^{(0)}] + \hat{\mathbf{N}}^{(S)} \tag{6.18}$$

and when there is feedback with gain g, the effect on the spins is

$$\hat{F}_{\rm z}^{(2)} = \hat{F}_{\rm z}^{(1)} + g\hat{S}_{\rm y}^{(1)} + \hat{\mathbf{N}}^{(FB)}. \tag{6.19}$$

In this situation, we are calculating the effect of the feedback including the decoherence in one direction, which will immediately lead to

$$\hat{F}_{\rm z}^{(2)} = (1-\eta)\hat{F}_{\rm z}^{(0)} - i\tau[\mathbf{F}^{(0)}, \hat{F}_{\rm z}^{(0)}] + g\hat{S}_{\rm y}^{(1)} + \hat{\mathbf{N}}^{(S)} + \hat{\mathbf{N}}^{(FB)}. \tag{6.20}$$

As has been described in preceding section, the noise added due to feedback is negligible and moreover since we are considering the one dimensional feedback $i\tau[\mathbf{F}^{(0)}, \hat{F}_{\mathrm{z}}^{(0)}] = 0$. We can rewrite the above equation as

$$\hat{F}_{\mathrm{z}}^{(2)} = ((1-\eta) + gG_1\hat{S}_{\mathrm{x}})\hat{F}_{\mathrm{z}}^{(0)} + g\hat{S}_{\mathrm{y}}^{(0)} + \hat{\mathbf{N}}^{(S)}. \tag{6.21}$$

If we choose $gG_1\hat{S}_{\mathrm{x}} = -1$ then we remove any prior contribution from $\hat{F}_{\mathrm{z}}$, and leave just the noise of the measurement times the gain of the feedback and the noise of the scattering. Note that this is not optimum in terms of cooling: Consider

$$\mathrm{var}\hat{F}_{\mathrm{z}}^{(2)} = ((1-\eta)gG_1\hat{S}_{\mathrm{x}})^2\mathrm{var}\hat{F}_{\mathrm{z}}^{(0)} + g^2\hat{S}_{\mathrm{y}}^{(0)} + \eta(2-\eta)\mathrm{var}\hat{F}_{\mathrm{z}}^{(0)} \tag{6.22}$$

assuming that $\hat{S}_{\mathrm{y}}$ and $\hat{F}_{\mathrm{z}}^{(0)}$ are uncorrelated. The minimum

$$\begin{aligned}\min[\mathrm{var}\hat{F}_{\mathrm{z}}^{(2)}] = \frac{1}{((G_1^2\hat{S}_{\mathrm{x}}^2\mathrm{var}\hat{F}_{\mathrm{z}}^{(0)} + \mathrm{var}\hat{S}_{\mathrm{y}}^{(0)})^2)}\big((-\eta^2+2\eta)G_1^4\hat{S}_{\mathrm{x}}^4(\mathrm{var}\hat{F}_{\mathrm{z}}^{(0)})^3 \\ + (3\eta^2-6\eta+5)G_1^2\hat{S}_{\mathrm{x}}^2(\mathrm{var}\hat{F}_{\mathrm{z}}^{(0)})^2\mathrm{var}\hat{S}_{\mathrm{y}}^{(0)} + (\mathrm{var}\hat{S}_{\mathrm{y}}^{(0)})^2\mathrm{var}\hat{F}_{\mathrm{z}}^{(0)}\big)\end{aligned} \tag{6.23}$$

is achieved for

$$g_{opt} = \big(2\mathrm{var}\hat{S}_{\mathrm{y}}^{(0)} - (1-\eta)2G_1\hat{S}_{\mathrm{x}}\mathrm{var}\hat{F}_{\mathrm{z}}^{(0)}\big)/2G_1^2\hat{S}_{\mathrm{x}}^2 \tag{6.24}$$

Already in this model we see a basic feature of the control theory: the optimum is a trade-off between removing the noise from the system, and introducing noise via feedback.

6.2.2 Feedback cooling in three dimensions

To extend the method of the one dimensional spin cooling to three dimensional spin cooling, we included the rotation of the state between measurements as described in chapter 7.

7

Spin Cooling

7.1 Introduction

We apply entropy removal by measurement and feedback to a cold atomic spin ensemble. Using quantum non-demolition probing by Faraday rotation measurement, and feedback by weak optical pumping, we drive the initially random collective spin variable $\hat{\mathbf{F}}$ toward the origin $\hat{\mathbf{F}} = 0$. We use input-output relations and ensemble quantum noise models to describe this quantum control process and identify an optimal two-round control procedure. We observe 12 dB of spin noise reduction, or a factor of 63 reduction in phase-space volume. The method offers a non-thermal route to generation of exotic entangled states in ultracold gases, including macroscopic singlet states and strongly correlated states of quantum lattice gases.

Many physical phenomena are accessible only at low temperatures, with examples ranging from superfluidity [93, 94] and the fractional quantum Hall effect [95] to quantum computing [96, 97], quantum-enhanced sensing [98, 99, 100, 86], and quantum simulation [101, 102, 9]. Traditional cooling couples the system of interest to a cold reservoir, allowing energy and entropy to leave the system. In contrast, feedback cooling [103] is a non-thermal process employing non-destructive measurement and feedback to remove entropy. This circumvents the requirements for a cold reservoir and for thermalization, which can be limiting in systems with finite lifetimes, e.g. atomic quantum simulators [79].

Feedback cooling has been applied to particle beams [103], trapped electrons [104], nano-mechanical resonators[105, 106], single ions [107], single atoms [108], dielectric microspheres[109, 110] and quantum fields in cavity QED[56, 111]. In addition to preparing a low-entropy state, feedback cooling on a many-body system has the potential to generate large-scale entanglement. For example, recent proposals for employing quantum non-demolition (QND) measurement of spin ensembles describe the generation of macroscopic singlet states [92, 112], and also structured quantum correlations[20, 21] characteristic of high-temperature superconductors [17]. Quantum correlations in the measurement-feedback process can be described by quantum control theory [113, 114].

Here we experimentally demonstrate feedback cooling of the collective spin $\hat{\mathbf{F}}$ of an ^{87}Rb atomic ensemble using quantum non-demolition (QND) measurement [6, 7, 8] by near-resonant Faraday rotation measurement and feedback by weak optical pumping. Starting from a high-entropy state, i.e., a distribution occupying a large volume of collective spin phase space, measurement plus feedback moves the system toward zero phase-space volume which has $|\hat{\mathbf{F}}|^2 = 0$. We analyze this quantum control problem using input-output relations and ensemble-based noise models [62, 40], to identify an optimal two-round feedback protocol. Applying this strategy we observe spin noise reduction by 12 dB and phase-space volume reduction by a factor of 63, in good agreement with theory.

7.2 System

The experiment is shown schematically in Figure 7.1(a). Our atomic spin ensemble consists of $N_{\mathrm{A}} \approx 10^6$ rubidium-87 atoms in the $f = 1$ ground hyperfine level, held in an optical dipole trap elongated in the z direction. Interactions among the atoms due to collisions and magnetic dipolar couplings are negligible at our density of $\sim 10^{11}\mathrm{cm}^{-3}$. We define the collective spin operator $\hat{\mathbf{F}} \equiv \sum_i \hat{\mathbf{f}}^{(i)}$, where $\hat{\mathbf{f}}^{(i)}$ is the spin of the i'th atom. The collective spin obeys commutation relations $[\hat{F}_{\mathrm{x}}, \hat{F}_{\mathrm{y}}] = i\hat{F}_{\mathrm{z}}$ (we take $\hbar = 1$ throughout).

Probe pulses are described by the Stokes operator $\hat{\mathbf{S}}$ defined as $\hat{S}_i \equiv \frac{1}{2}(\hat{a}_+^\dagger, \hat{a}_-^\dagger)\sigma_i(\hat{a}_+, \hat{a}_-)^T$, where the σ_i are the Pauli matrices and $\hat{a}_\pm$ are annihilation operators for $\sigma_\pm$ polarization. As with $\hat{\mathbf{F}}$, the components of $\hat{\mathbf{S}}$ obey $[\hat{S}_\mathrm{x}, \hat{S}_\mathrm{y}] = i\hat{S}_\mathrm{z}$ and cyclic permutations. The input pulses are fully $\hat{S}_\mathrm{x}$-polarized, i.e. with $\langle \hat{S}_\mathrm{x} \rangle = N_\mathrm{L}/2$, $\langle \hat{S}_\mathrm{y} \rangle = \langle \hat{S}_\mathrm{z} \rangle = 0$ and $\Delta^2 S_i = N_\mathrm{L}/4$, $i \in \{x, y, z\}$ where N_L is the number of photons in the pulse. While passing through the ensemble, the probe pulses experience the interaction hamiltonian $\hat{H}_\mathrm{eff} = \kappa_1 \tau^{-1} \hat{S}_\mathrm{z} \hat{F}_\mathrm{z}$, where κ_1 is a coupling coefficient for vector light shifts [38, 40]. This rotates the pulse by an angle $\phi = \kappa_1 \hat{F}_\mathrm{z} \ll 1$, so that a measurement of $\hat{S}_\mathrm{y}^{(\mathrm{out})}/\hat{S}_\mathrm{x}^{(\mathrm{in})}$ indicates $\hat{F}_\mathrm{z}$ with a shot-noise-limited sensitivity of $\Delta\hat{F}_\mathrm{z} = \Delta\hat{S}_\mathrm{y}/\kappa_1$. Tensor light shifts are negligible in this work [7].

7.3 Control strategy

Our aim is to reduce the state's phase space volume $\Delta^2\hat{\mathbf{F}} \equiv \langle|\hat{\mathbf{F}}|^2\rangle - |\langle\hat{\mathbf{F}}\rangle|^2$ using measurement and feedback to sequentially set $\hat{F}_\mathrm{z}$, $\hat{F}_\mathrm{y}$ and $\hat{F}_\mathrm{x}$ to desired values. In this experiment, the desired values are zero mean value for all components of angular momentum. This is possible using QND measurements and non-destructive feedback, which we implement with weak optical pumping. The spin uncertainty relations, $\Delta F_i \Delta F_j \geq |\langle F_k \rangle|/2$ even allow $\Delta^2\hat{\mathbf{F}}$ to approach zero for the macroscopic singlet state [92]. Faraday rotation gives high-sensitivity measurement of $\hat{F}_\mathrm{z}$. To access $\hat{F}_\mathrm{x}$ and $\hat{F}_\mathrm{y}$, we apply a static magnetic field of $B \approx 14$ mG along the $[1, 1, 1]$ axis (Larmor period $T_L \simeq 120$ µs) to induce $\hat{F}_\mathrm{z} \to \hat{F}_\mathrm{x} \to \hat{F}_\mathrm{y}$ precession, and probe at $T_L/3$ intervals. The optical pumping performs a controlled displacement of the spin state (a rotation would leave $|\hat{\mathbf{F}}|$ unchanged) toward a desired value. For increased accuracy, we repeat the three-axis measurement and feedback. The experimental sequence is illustrated in Fig. 7.1(b).

7.4 QND Measurement

We measure the collective spin component F_z by paramagnetic Faraday rotation probing with 1 µs long pulses of linearly polarized light with on average

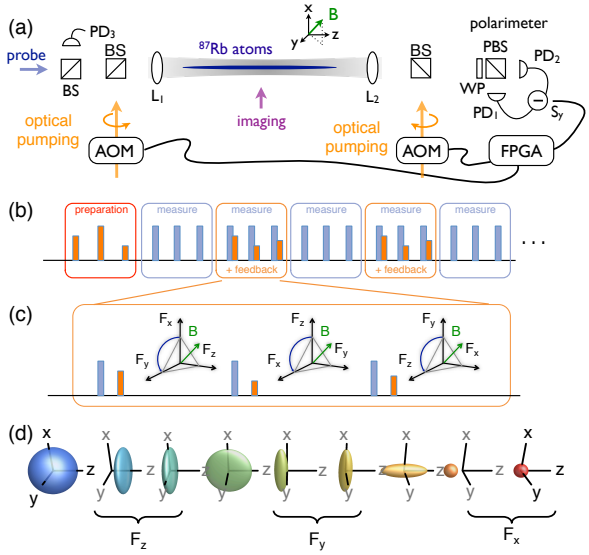

Figure 7.1: Experimental schematic, pulse sequence, and control diagram for spin cooling by QND measurement + feedback. **(a)** Experimental geometry. Near-resonant probe pulses pass through a cold cloud of ^{87}Rb atoms and experience a Faraday rotation by an angle proportional to the on-axis collective spin $\hat{F}_z$. The pulses are initially polarized with maximal Stokes operator $\hat{S}_x$ recorded on reference detector (PD_3). Rotation toward $\hat{S}_y$ is detected by a balanced polarimeter consisting of a wave-plate (WP), polarizing beam-splitter (PBS), and photodiodes ($PD_{1,2}$). A field-programmable gate array (FPGA)-based controller interprets the polarimeter signal and reference and produces optical feedback pulses via acousto-optic modulators (AOM)s. $\hat{\mathbf{F}}$ precesses about a magnetic field ($\mathbf{B}$) along the direction [1,1,1] making all components accessible to measurement and feedback through stroboscopic probing. **(b-c)** Pulse sequence: A first QND measurement measures the F_z angular momentum component and the FPGA calculates the Faraday rotation angle in ≈11 μs. The FPGA applies a control pulse, proportional to the Faraday rotation angle, to an AOM to generate optical-pumping feedback. At the appropriate times in the Faraday rotation cycle, the same process is applied to also to F_y and F_x. **(d)** Evolution of the state in $\hat{\mathbf{F}}$ phase space as it is transformed by successive measurement, feedback and precession steps.

$N_{\mathrm{L}} = 5.4 \times 10^7$ photons per pulse at a detuning of 700 MHz to the red of the $f = 1 \rightarrow f' = 0$ transition. Measurements are made at $T_L/3 \simeq 40$ µs intervals, to access sequentially $\hat{F}_{\mathrm{z}}$, $\hat{F}_{\mathrm{y}}$ and $\hat{F}_{\mathrm{x}}$. A shot-noise limited balanced polarimeter detects $\hat{S}_{\mathrm{y}}^{(\mathrm{out})}$ while a reference detector before the atoms measures $\hat{S}_{\mathrm{x}}^{(\mathrm{in})}$ [6] . Both signals are collected by a real–time FPGA–based controller, which computes the measurement result $\mathcal{F} \equiv \hat{S}_{\mathrm{y}}^{(\mathrm{out})}/(\kappa_1 \hat{S}_{\mathrm{x}}^{(\mathrm{in})})$ and generates timing signals to control the optical pumping feedback.

7.5 Optical pumping and feedback

The optical pumping is performed in a nearly-linear regime, i.e. with few photons, such that only a small fraction of the atoms changes state. We use circularly polarized light 30 MHz red detuned from the $f = 1 \rightarrow f' = 0$ transition on the D_2 line with an intensity ~ 7 W/m^2, propagating along the trap axis and chopped into ∼µs pulses by acousto-optic modulators (AOMs). Two beams in opposite directions allow rapid switching between the two circular polarizations. As with the QND measurement, Larmor precession allows feedback to $\hat{F}_{\mathrm{z}}$, $\hat{F}_{\mathrm{y}}$ and $\hat{F}_{\mathrm{x}}$ by $\hat{F}_{\mathrm{z}}$ pumping at different points in the cycle. In the feedback step the AOMs are gated by the FPGA after a latency of $t_{\mathrm{lat}} = 11$ µs for computation. The FPGA determines the polarization and pulse duration $t_{\mathrm{FB}} \propto \mathcal{F}$, which in turn determines the displacement of $\hat{\mathbf{F}}$. Typical feedback pulses are 1–2 µs, i.e., much shorter than the Larmor precession period, and much longer than the ~ 100 ns rise time of the AOMs. An independent AOM amplitude control determines the overall gain of the feedback.

7.6 Initialization procedure

We first generate a fully mixed $f = 1$ state as described in [6], apply the magnetic field along [1,1,1] direction, then sequentialy optically pump $\hat{F}_{\mathrm{z}}$, $\hat{F}_{\mathrm{y}}$ and $\hat{F}_{\mathrm{x}}$ with 5 µs pulses. The amplitude A and polarization sign s of the pulses are randomly chosen so that sA is zero-mean normally distributed. This generates a statistically-reproducible distribution of initial states with

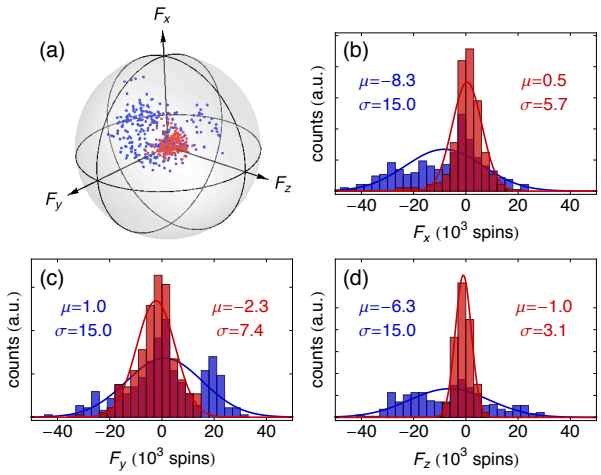

Figure 7.2: Input and output spin distributions. (a) Measured input spin distribution (blue data) following the initialization procedure described in the main text, and measured output spin distribution (red data) following a single feedback step with the optimum feedback gain setting. The gray sphere has a radius of 6×10^4 spins. (b)–(d) Histograms of the measurements of each of the three spin components before (blue) and after (red) feedback. See text for details.

initial spin covariance matrix $\Gamma_F \equiv \frac{1}{2}\langle F_i F_j + F_j F_i\rangle - \langle F_i\rangle\langle F_j\rangle$ of

$$\Gamma_F = \begin{pmatrix} 2.70 & -0.03 & -1.20 \\ -0.03 & 2.30 & -0.65 \\ -1.20 & -0.65 & 2.20 \end{pmatrix} \times 10^8\,\mathrm{spins}^2, \tag{7.1}$$

i.e., with noises $N_{\mathrm{A}}^{1/2} \ll \Delta F_i \ll N_{\mathrm{A}} \simeq 10^6$.

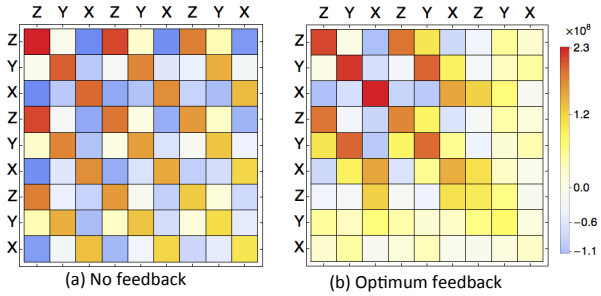

Figure 7.3: Correlation between consecutive three–component collective spin measurements. (a) Covariance matrix for 9 consecutive stroboscopic measurements with no feedback showing strong correlations between all three measurements of each spin component F_i (red and orange squares). (b) Covariance matrix for 9 consecutive stroboscopic measurements with feedback after measurements 4–6 with the optimal gain setting. The first two measurements of each spin component F_i remain strongly correlated, but the correlation is removed by the feedback and the third set of measurements is not correlated with the first two. Also apparent is the noise reduction after feedback.

7.7 Control and characterization sequence

For a given normalized gain $g \equiv G/G_0$, where G is the feedback gain and G_0 is the naïve gain, i.e. optimal gain for the noiseless case, we characterize the cooling process with the sequence shown in Fig. 7.1(b): initial state preparation, measurement without feedback, measurement with feed-

back and measurement without feedback. We then remove the atoms from the trap and repeat the same sequence to record the measurement read–out noise. The entire cycle is run 300 times to collect statistics.

In Fig. 7.2(a) we plot the input spin distribution (blue) following our initialization procedure, and the output spin distribution (red) after feedback with the optimum feedback gain setting. The input state is distributed around the origin, with a mean deviation of 2.4×10^4 spins and a total variation of $\Delta^2\hat{\mathbf{F}} = 6.7 \times 10^8\,\mathrm{spins}^2$. Histograms of the measurements are shown in Fig. 7.2(b)–(d). After feedback (red data) the total variation of the spin distribution is $\Delta^2\hat{\mathbf{F}} = 9.7 \times 10^7\,\mathrm{spins}^2$, an 8 dB reduction in a single feedback step. The dispersion of all three spin components is reduced by a factor of 3–5, and the average of each spin component remains centered within one standard deviation of the origin.

7.8 Correlations analysis

Covariance matrices describing all nine measurements, for $g = 0$ (null case) and gains $g = -0.75$ (optimal case) are shown in Fig. 7.3. Three features are noteworthy: 1) Both null and optimal cases show strong correlations between the first and second measurement groups, confirming the non-destructive nature of the Faraday rotation measurement. 2) the correlations of one component, e.g. $\hat{F}_\mathrm{y}$, persist even after feedback to another component, e.g. $\hat{F}_\mathrm{z}$, indicating the non-destructive nature of the optical feedback. 3) While the control case shows some reduction of total variance (due to spin relaxation), the feedback control is far more effective.

7.9 Modeling

We use a multi-step input-output model of the collective spin operators to describe the feedback cooling process. During a step of length Δt, an operator $\hat{O}$ experiences $\hat{O}^{(i+1)} = \hat{O}^{(i)} - i\Delta t[\hat{O}^{(i)}, \hat{H}_\mathrm{eff}^{(i)}] + \mathcal{N}$, where superscripts $^{(i)}$,$^{(i+1)}$ indicate prior and posterior values, respectively, and $\mathcal{N}$ is a noise operator. Starting from atomic and optical inputs $\hat{\mathbf{F}}^{(0)}$, $\hat{\mathbf{S}}^{(0)}$, respectively, a

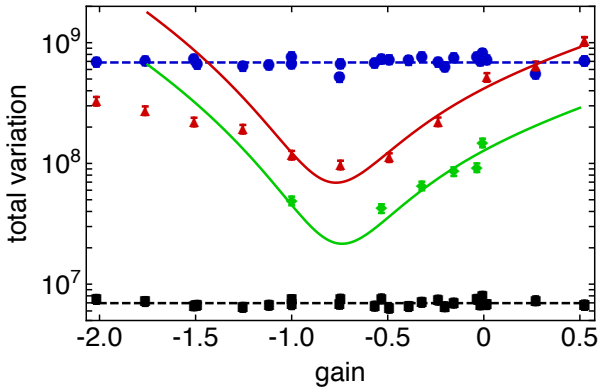

Figure 7.4: Spin cooling via optical feedback. Measured total variation $\Delta^2\hat{\mathbf{F}}$ following one (red triangles) and two (green diamonds) feedback steps. We compare this to the theory described in the text (red and green solid curves) fit to the $g \geq -1.0$ data. Also shown is the noise of the input spin state following the initialization procedure (blue circles), with an average total variation $\Delta^2\hat{\mathbf{F}} = 6.7 \times 10^8\,\text{spins}^2$ (blue dashed line), and the measurement read–out noise (black squares), with an average total variation $\Delta^2\hat{\mathbf{F}} = 7.0 \times 10^6\,\text{spins}^2$ (black dashed line). Error bars represent $\pm 1\sigma$ statistical errors.

Faraday rotation measurement produces

$$\hat{S}_{\rm y}^{(1)} = \hat{S}_{\rm y}^{(0)} + \kappa_1 \hat{S}_{\rm x}^{(\rm in)} \hat{F}_{\rm z}^{(0)} \tag{7.2}$$

$$\hat{\mathbf{F}}^{(1)} = (1-\eta)\hat{\mathbf{F}}^{(0)} - i\tau[\hat{\mathbf{F}}^{(0)}, \hat{F}_{\rm z}]\hat{S}_{\rm z}^{(0)} + \hat{\mathbf{N}}^{(\rm S)} \tag{7.3}$$

with $\hat{S}_{\rm x}, \hat{S}_{\rm z}$ changing negligibly. Measurement back-action on the atoms $-i\tau[\hat{\mathbf{F}}^{(0)}, \hat{F}_{\rm z}]\hat{S}_{\rm z}^{(0)}$ is small provided $|\langle \hat{F}_{\rm x}\rangle|, |\langle \hat{F}_{\rm y}\rangle| \ll N_{\rm A}$. $\hat{\mathbf{N}}^{(\rm S)}$ arises from the fraction η of atoms that suffer spontaneous emission (see below). During latency, precession by an angle $\theta = 2\pi t_{\rm lat}/T_{\rm L}$ about $[1,1,1]$ causes coherent rotation $R_{\mathbf{B}}(\theta)$ and dephasing due to field inhomogeneities [115, 40]:

$$\hat{\mathbf{F}}^{(2)} = X(\theta)\hat{\mathbf{F}}^{(1)} + \hat{\mathbf{N}}^{(\theta)}, \tag{7.4}$$

$$X(\theta) \equiv P_{\mathbf{B}} + \exp[-\frac{\theta}{\omega_L T_2}] R_{\mathbf{B}}(\theta)(\mathbb{1} - P_{\mathbf{B}}) \tag{7.5}$$

where $P_{\mathbf{B}}$ is a projector onto the $[1,1,1]$ direction and T_2 is the transverse relaxation time. Longitudinal relaxation is negligible on the time-scale of the experiment. Feedback modifies the collective spin as

$$\hat{\mathbf{F}}^{(3)} = G\mathbb{f}_z \hat{S}_{\rm y}^{(2)} + \hat{\mathbf{F}}^{(2)} + \hat{\mathbf{N}}^{(\rm FB)} \tag{7.6}$$

where G is the feedback gain and $\mathbb{f}_z$ is a unit vector in the z direction. Precession by $\bar{\theta} = 2\pi/3 - \theta$ completes the $1/3$ Larmor rotation, giving

$$\begin{aligned}\hat{\mathbf{F}}^{(4)} = {} & X(\bar{\theta})\Big[G\mathbb{f}_z(\hat{S}_{\rm y}^{(0)} + \kappa_1 \hat{S}_x \hat{F}_{\rm z}^{(0)}) + X(\theta)\hat{\mathbf{F}}^{(0)} \\ & + \hat{\mathbf{N}}^{(\rm FB)} + \hat{\mathbf{N}}^{(\theta)} + \hat{\mathbf{N}}^{(\rm S)}\Big] + \hat{\mathbf{N}}^{(\bar{\theta})}.\end{aligned} \tag{7.7}$$

for measurement+feedback for one component.

The vector feedback procedure is the composition of three transformations as in Eq. (7.7). These correct sequentially for all three components of $\hat{\mathbf{F}}$, and introduce a total of twelve noise terms analogous to $\hat{S}_{\rm y}^{(0)}$, $\hat{\mathbf{N}}^{(\rm FB)}$, $\hat{\mathbf{N}}^{(\theta)}$ and $\hat{\mathbf{N}}^{(\bar{\theta})}$, given in the section 7.12.

7.10 Optimized multi-step cooling

We define the normalized gain $g \equiv G/|G_0|$ where $G_0 \equiv -1/(\kappa_1 \hat{S}_x)$ is the naïve gain, i.e., the optimal gain for when noise, dephasing and latency are zero. Minimizing $\Delta^2\hat{\mathbf{F}}^{(4)}$ requires $-1 < g < 0$ because of competition between the $G\mathbb{f}_z\hat{S}_y^{(0)}$ and $G\mathbb{f}_z\kappa_1\hat{S}_x\hat{F}_z^{(0)} - X(\theta)\hat{\mathbf{F}}^{(0)}$ contributions in Eq. (7.7). Moreover, the optimal g increases with increasing signal-to-noise ratio $\Delta^2\hat{\mathbf{F}}^{(0)}/\Delta^2\hat{S}_y^{(0)}$. This suggests a multi-round feedback strategy employing successive three-axis feedback steps, with decreasing $|g|$, to approach the limiting entropy set by $\Delta^2\hat{S}_y^{(0)}$ and $\Delta^2\hat{\mathbf{N}}^{(S)}$.

We demonstrate this optimized multi-step cooling with results shown in Fig. 7.4. Again following the sequence of Fig. 7.1, we initialize to give measured total spin variance $\Delta^2\hat{\mathbf{F}} \approx 6.7 \times 10^8\,\text{spins}^2$, shown as blue circles. In a first experiment we apply a single round of three-axis measurement+feedback, then measure the resulting state, and compute total variance (red triangles). As expected, an optimum is observed at $g \simeq -0.75$, with variance $9.7 \times 10^7\,\text{spins}^2$ or 8 dB reduction in the spin noise. In a second experiment we apply a first round with $g = -0.75$ followed by a second round with variable g, shown as green diamonds. This gives a further 4 dB reduction, to $4.2 \times 10^7\,\text{spins}^2$. Model predictions, with $\kappa_1 = 1.1 \times 10^{-7}$, $N_A = 10^6$, $N_L = 5.4 \times 10^7$, $T_2 = 1.3$ ms from independent measurements are fit to the global data set to calibrate the optical pumping efficiency (effectively g), and the initial noise $\Delta^2\hat{\mathbf{F}}^{(0)}$. Good agreement is observed except for $g \leq -1.5$, a region in which the strong feedback is expected to invert and amplify the initial $\hat{\mathbf{F}}$.

7.11 Conclusion

Using Faraday-rotation quantum non-demolition measurements and feedback by optical pumping, we have reduced the spin variance of a laser-cooled ^{87}Rb atomic ensemble. The total spin variance $\Delta^2\hat{\mathbf{F}}$ is reduced by 12 dB, or a reduction in phase-space volume by a factor of 63, using an optimized two-step procedure informed by a realistic quantum control theory incorporating

experimental imperfections. The procedure has potential application to on-demand generation of quantum-correlated states of ultra-cold atomic gases, for example generation of macroscopic singlet states and arbitrary quantum correlations in lattice-bound degenerate quantum gases.

7.12 Noise terms

Readout noise is $\Delta^2 \hat{S}_y^{(0)} = N_L/4$, as above. $\hat{\mathbf{N}}^{(S)}$ arises from spontaneous emission events, which randomize the spins of a fraction $\eta_S \approx 2\kappa_1^2 N_A N_L/(3\alpha_0)$ of the atoms [59, 62], introducing a noise $\Delta^2 N_i^{(S)} = \Delta^2 f_i^{(1)} \eta_S (1-\eta_S) N_A + \eta_S N_A f(f+1)/3$ where $\hat{\mathbf{f}}_i^{(1)}$ is the mean single-atom spin vector. For unpolarized states $\Delta^2 N_i^{(S)} \approx N_A \eta_S (2-\eta_S) f(f+1)/3$. Similarly, dephasing randomizes the transverse polarizations of a fraction $\eta_D \equiv 1 - \exp[\theta/(2\pi T_L)]$ giving noise $\Delta^2 N_i^{(\theta)} \approx N_A \eta_D (2-\eta_D) f(f+1)/3$. The optical pumping process is stochastic but uncorrelated among the atoms, leading to a multinomial distribution in the displacement $\hat{\mathbf{F}}^{(FB)} \equiv \hat{\mathbf{F}}^{(2)} - \hat{\mathbf{F}}^{(1)}$ and a noise $\hat{\mathbf{N}}^{(FB)} \propto |\langle \hat{\mathbf{F}}^{(FB)} \rangle|^{1/2}$, which is $\ll |\langle \hat{\mathbf{F}}^{(FB)} \rangle|$ except if $|\langle \hat{\mathbf{F}}^{(FB)} \rangle| \sim 1$. In this experiment with large α_0 and small N_L, only $\hat{S}_y^{(0)}$ and $\hat{\mathbf{N}}^{(S)}$ make a significant contribution.

8

Background for the singlet state experiment

This chapter presents the background material related to the singlet state experiment presented in chapter 9. We present the spin squeezing inequality which is our main criterion to verify the generation of macroscopic spin singlet in cold atomic ensemble.

8.1 Spin squeezing inequality

One of the methods developed to verify the existence of entanglement in a many body system is the spin squeezing inequality [116]. Spin squeezed states for spin-$\frac{1}{2}$ systems have created in numerous experiments in cold atoms and trapped ions [117, 6, 118, 119, 120, 121, 122, 123, 124]. The relevant spin squeezing inequalities in our case, is the spin squeezing inequality for spin-1 systems. In [125], Vitagliano, et al discussed a complete set of inequalities for arbitrary spin. For fully separable states of spin-f particles, all the following inequalities are fulfilled

$$\langle F_x^2\rangle + \langle F_y^2\rangle + \langle F_z^2\rangle \leq Nf(Nf+1) \tag{8.1}$$

$$(\Delta F_x)^2 + (\Delta F_x)^2 + (\Delta F_x)^2 \geq Nf \tag{8.2}$$

$$\langle \tilde{F}_k^2\rangle + \langle \tilde{F}_l^2\rangle - N(N-1)f^2 \leq (N-1)(\tilde{\Delta}F_m)^2 \tag{8.3}$$

$$(N-1)[(\tilde{\Delta}F_k)^2 + (\tilde{\Delta}F_l)^2] \geq \langle \tilde{F}_m^2 \rangle - N(N-1)f^2 \tag{8.4}$$

where N is the number of spin-f particles, k, l, m take all possible permutation of x, y, z, $F_l = \sum_{n=1}^{N} f_l^{(n)}$ for $l = x, y, z$ are the collective angular momentum components and $f_l^{(n)}$ are the single angular momentum components acting on $n^{(th)}$ atom. $\langle \tilde{F}_k^2 \rangle = \langle F_k^2 \rangle - \langle \sum_n (f_k^{(n)})^2 \rangle$ is the modified second moment and $(\tilde{\Delta}F_m)^2 = (\Delta F_m)^2 - \langle \sum_n (f_k^{(n)})^2 \rangle$ is the modified variance. Violation of any of these inequalities implies entanglement. The proof has been discussed in [125, 126, 127, 128, 129, 130, 92].

In our case, we have used the second inequality of the list above. We thus define a spin-squeezing parameter as

$$\xi_s^2 = \frac{(\Delta F_x)^2 + (\Delta F_y)^2 + (\Delta F_z)^2}{Nf}. \tag{8.5}$$

$\xi_s^2 < 0$ is not consistent with a separable state and thus implies entanglement.

9

Macroscopic spin singlet

9.1 Introduction

Generating and detecting large-scale spin entanglement in many-body quantum systems is of fundamental interest [10, 9] and motivates many experiments with cold atoms [11, 12, 13, 14, 15] and ions [16]. For example, macroscopic singlet states appear as ground states of many fundamental spin models [17, 18], and even in quantum gravity calculations of black hole entropy [19]. Here we report the production of a macroscopic spin singlet (MSS) in an atomic system using collective quantum non-demolition (QND) measurement [6, 7, 8] as a global entanglement generator.

QND measurement is a well-established technique for generating conditional spin squeezing in polarized atomic samples [121, 98, 83, 99, 131, 118, 86], where the state-of-the-art is 10 dB of squeezing in a cavity-enhanced measurement [132]. In our experiment we apply QND measurement techniques to an unpolarized sample. The QND measurement first generates large-scale atom-light entanglement by passing a macroscopic optical pulse through the entire ensemble. The optical pulse is then measured, transferring the entanglement onto the atoms and leaving them in an entangled state [92]. Subsequent measurements on the ensemble confirm the presence of a MSS with a singlet fraction of approximately one half. Our techniques are closely related to proposals for using QND measurement to detect [21, 133] and generate [20] long-range correlations in quantum lattice gases and spinor

condensates.

A MSS has a collective spin $\hat{\mathbf{F}} = 0$, where $\hat{\mathbf{F}} \equiv \sum_i \hat{\mathbf{f}}^{(i)}$ and $\hat{\mathbf{f}}^{(i)}$ is the spin of the i'th atom. This implies that fluctuations in the collective spin vanish, i.e. $\Delta\hat{\mathbf{F}} = 0$, suggesting that we can both produce and detect a macroscopic singlet via QND measurement induced spin squeezing [92, 20]. Indeed, it has been shown that a macroscopic spin singlet can be detected via the generalized spin squeezing parameter

$$\xi^2 = \frac{\sum_k (\Delta \hat{F}_k)^2}{f N_A} \tag{9.1}$$

where $\xi^2 < 1$ indicates spin squeezing in the sense of noise properties not producible by any separable state, and thus detects entanglement among the atoms [127, 134, 126, 92, 125, 135]. The standard quantum limit (SQL) for unpolarized atoms is set by $\xi^2 = 1$, i.e. $\sum_k (\Delta \hat{F}_k)^2 = f N_A$. The number of atoms that are at least pairwise entangled in such a squeezed state is lower-bounded by $(1-\xi^2)N_A$ [92]. In the limit $\xi^2 \to 0$, the macroscopic many-body state is a true spin singlet. Another criterion for detecting entanglement in non-polarized states has recently been applied to Dicke-like spin states [136]. Our results complement recent work with quantum lattice gases [11, 13, 15], and are analogous to the generation of macroscopic singlet Bell states with optical fields [2, 137].

Since the collective spin obeys spin uncertainty relations $(\Delta \hat{F}_i)^2 (\Delta \hat{F}_j)^2 \geq |\langle \hat{F}_k \rangle|^2/4$ (we take $\hbar = 1$ throughout), squeezing all three spin components requires maintaining an unpolarized atomic sample with $\langle \hat{F}_k \rangle \simeq 0$. Our experiment starts from a thermal spin state (TSS), i.e. a completely mixed state described by a density matrix $R = \rho^{\otimes N_A}$, where $\rho = \frac{1}{3}\mathbb{1}_{3\times 3}$ and $\mathbb{1}_{3\times 3}$ is the identity matrix. This state has $\langle \hat{F}_k \rangle = 0$ and $(\Delta \hat{F}_k)^2 = (2/3)N_A$. It is symmetric under exchange of atoms, and mixed at the level of each atom.

We probe the atoms via paramagnetic Faraday rotation using pulses of near-resonant propagating along the trap axis to give a high-sensitivity measurement of $\hat{F}_z$. The optical pulses are described by Stokes operators $\hat{\mathbf{S}}$, which obey $[\hat{S}_x, \hat{S}_y] = i\hat{S}_z$ and cyclic permutations. The input pulses are fully $\hat{S}_x$-polarized, i.e. with $\langle \hat{S}_x \rangle = N_L/2$, where N_L is the number of pho-

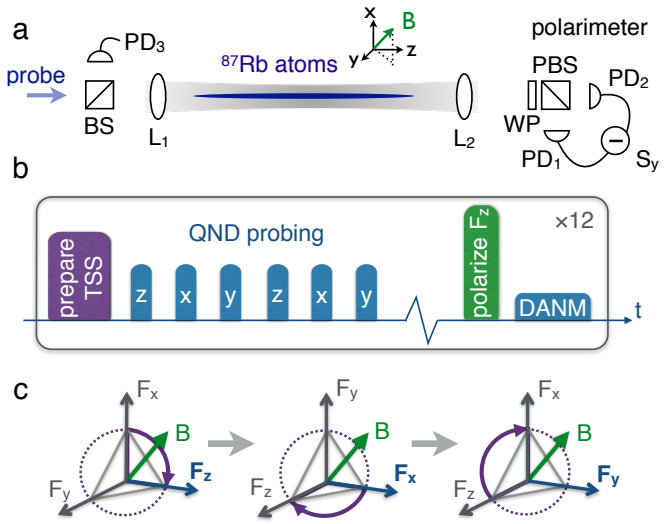

Figure 9.1: (a) Experimental geometry. Near-resonant probe pulses pass through a cold cloud of ^{87}Rb atoms and experience a Faraday rotation by an angle proportional to the on-axis collective spin $\hat{F}_z$. The pulses are initially polarized with maximal Stokes operator $\hat{S}_x$ recorded on reference detector (PD3). Rotation toward $\hat{S}_y$ is detected by a balanced polarimeter consisting of a wave plate (WP), polarizing beam splitter (PBS), and photodiodes (PD1,2). (b) Pulse sequence: A first QND measurement measures the $\hat{F}_z$ angular momentum component of the input atomic state, and the second and third QND measurements in 1/3 and 2/3 of Larmor precession cycles measure $\hat{F}_y$ and $\hat{F}_x$ respectively. (c) $\hat{\mathbf{F}}$ precesses about a magnetic field ($\mathbf{B}$) along the direction [111] making all components accessible to measurement via stroboscopic probing.

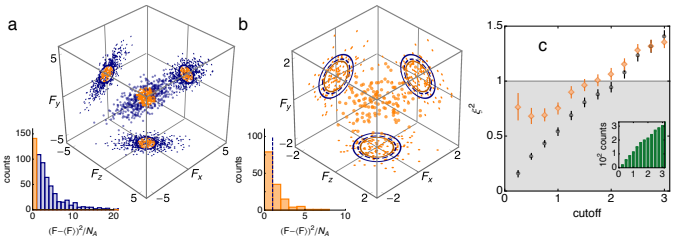

Figure 9.2: Selection of a macroscopic spin singlet. From the initial spin distribution (blue data in figure (a)), we select data with $|\hat{\mathbf{F}}^{(1)} - \langle\hat{\mathbf{F}}^{(1)}\rangle|^2/N_A < C$ (orange data in figure (a)), where C is a chosen cutoff parameter. We then analyze the second QND measurement $\hat{\mathbf{F}}^{(2)}$ of the same data (orange data in figure (b)) to detect spin squeezing and entanglement. We illustrate this with data from a sample with $N_A = 1.1 \times 10^6$ atoms and $C = 1$. Axes in (a) & (b) have units of 10^3 spins. In (a), the solid blue circle has a radius $\sqrt{CN_A}$. In (b), the solid blue circle has a radius equal to the 1σ Gaussian RMS of an input ideal TSS with $\xi^2 = 2$, including detection noise, and the dashed blue circle the same for a state with $\xi^2 = 1$. The solid orange circles in (b) indicates the measured 1σ Gaussian RMS of the selected data. In the insets we plot a histogram of the first and second measurements. The selected data are plotted in orange, and the dashed blue line in (b) indicates the cutoff. (c) Spin squeezing parameter ξ^2 (orange diamonds) calculated from the second QND measurement of the selected data as a function of the cutoff parameter C. The shaded region indicates $\xi^2 < 1$, i.e. spin squeezing according to the criterion given in Eq. (9.1). For reference, the same parameter calculated from the first QND measurement is also plotted (black circles). Inset: number of selected data points included as a function of the cutoff parameter.

tons in the pulse. During a measurement pulse, the atoms and light interact via a light-matter interaction Hamiltonian.The full light-atom interaction Hamiltonian has been described in section 2.2.1. The first term of the Hamiltonian in Eq. 2.15 describes Paramagnetic Faraday rotation: it rotates the polarization in the $\hat{S}_\mathrm{x}$, $\hat{S}_\mathrm{y}$ plane by an angle $\phi = G_1\hat{F}_\mathrm{z} \ll 1$, and leaves $\hat{F}_\mathrm{z}$ unchanged. It rotates the atomic state about $\hat{F}_\mathrm{z}$, by an angle proportional to $\hat{S}_\mathrm{z}$. A measurement of $\hat{S}_\mathrm{y}^{(\mathrm{out})}/\hat{S}_\mathrm{x}^{(\mathrm{in})}$ indicates $\hat{F}_\mathrm{z}$ with a shot-noise-limited sensitivity of $\Delta\hat{F}_\mathrm{z} = \Delta\hat{S}_\mathrm{y}/G_1$. Acting alone, this describes a QND measurement of $\hat{F}_\mathrm{z}$, i.e., with no back-action on $\hat{F}_\mathrm{z}$. The second term, in contrast, leads to an optical rotation $\hat{S}_\mathrm{x} \to \hat{S}_\mathrm{z}$ (due to the birefringence of the atomic sample), and drives a rotation of the atomic spins in the $\hat{F}_\mathrm{z}$, $\hat{J}_y$ plane (alignment-to-orientation conversion) by an angle $\tan\theta = G_2\hat{S}_\mathrm{x}/2$ [86, 40]. For the experiments described here $\theta \approx 0.3$, so that $S_y^{(\mathrm{out})}$ includes significantly more F_z than J_y. For this reason, we will ignore the G_2 term. A way to include the effects of the G_2 term is described in [86, 138]. We thus arrive to the effective Hamiltonian

$$\tau\hat{H}_\mathrm{eff} = G_1\hat{S}_\mathrm{z}\hat{F}_\mathrm{z} \tag{9.2}$$

Eq. (9.2) describes a QND measurement of $\hat{F}_\mathrm{z}$, i.e., a measurement with no back-action on $\hat{F}_\mathrm{z}$. We detect the output

$$\hat{S}_\mathrm{y}^{(\mathrm{out})} = \hat{S}_\mathrm{y}^{(\mathrm{in})} + G_1\hat{S}_\mathrm{x}^{(\mathrm{in})}\hat{F}_\mathrm{z}^{(\mathrm{in})} \tag{9.3}$$

which leads to measurement-induced conditional spin squeezing of the $\hat{F}_\mathrm{z}$ component by a factor $1/(1+\zeta)$, where $\zeta = \frac{2}{3}G_1^2 N_L N_A$ is the signal-to-noise ratio (SNR) of the measurement [60].

To measure and squeeze the remaining spin components, we follow a stroboscopic probing strategy described in Refs. [115, 28]. We apply a magnetic field along the [1,1,1] direction so that the collective atomic spin rotates $\hat{F}_\mathrm{z} \to \hat{F}_\mathrm{x} \to \hat{F}_\mathrm{y}$ during one Larmor precession cycle. We then time our probe pulses to probe the atoms at $T_L/3$ intervals, allowing us to measure all three components of the collective spin in one Larmor period. Note that the probe

duration $\tau \ll T_L$, so that we can neglect the rotation of the atomic spin during a probe pulse.

This measurement procedure respects the exchange symmetry of the input TSS, and generates correlations among pairs of atoms independent of the distance between them, leading to large-scale entanglement of the atomic spins. The resulting state has $(1-\xi^2)N_A$ spins entangled in a MSS, and $\xi^2 N_A$ spin excitations (spinons).

Our experimental apparatus, illustrated in Fig. 9.1(a), is described in detail in Refs. [41]. In each cycle of the experiment we trap up to 1.5×10^6 ^{87}Rb atoms in a weakly focused single beam optical dipole trap. The atoms are laser-cooled to a temperature of 20 μK, and optically pumped into the $f = 1$ hyperfine ground state. A shot-noise-limited balanced polarimeter detects $\hat{S}_{\rm y}^{(\rm out)}$ while a reference detector before the atoms measures $\hat{S}_{\rm x}^{(\rm in)}$. The trap geometry produces a large atom-light interaction for light pulses propagating along the axis of the trap, quantified by the effective optical depth $d_0 = (\sigma_0/A)N_A$, where $\sigma_0 = \lambda^2/\pi$ and $A = 2.7\times10^{-9}$ m is the effective atom-light interaction area [41], giving $d_0 = 69.5$ with $N_A = 1.5\times10^6$ atoms. We measure an atom-light coupling constant $G_1 = 9.0 \pm 0.1 \times 10^{-8}$ radians per spin [139]. The measured sensitivity of the Faraday rotation probing is $\Delta F_z = 515$ spins [6], allowing projection-noise-limited probing of an input TSS with $N_A > 1.75 \times 10^5$ atoms. The measurement sequence is illustrated in Figs. 9.1(b),(c). For each measurement, the atoms are initially prepared in a TSS via repeated optical pumping of the atoms between $f = 1$ and $f = 2$, as described in Ref. [6]. We then probe the atomic spins using a train of $\tau = 1$ μs long pulses of linearly polarized light, detuned by 700 MHz to red of the $f = 1 \rightarrow f' = 0$ transition of the D_2 line. Each pulse contains on average $N_L = 2.8 \times 10^8$ photons. To access also $\hat{F}_{\rm x}$ and $\hat{F}_{\rm y}$, we apply a magnetic field with a magnitude $B = 16.9\pm0.1$ mG along the direction [111]. The atomic spins precess around this applied field with a Larmor period of $T_L = 85$ μs $\gg \tau$, and we probe the atoms at $T_L/3 = 28.3$ μs intervals for two Larmor periods, allowing us to analyze the statistics of repeated QND measurements of the collective spin.

After the QND probing, the number of atoms N_A is quantified via dis-

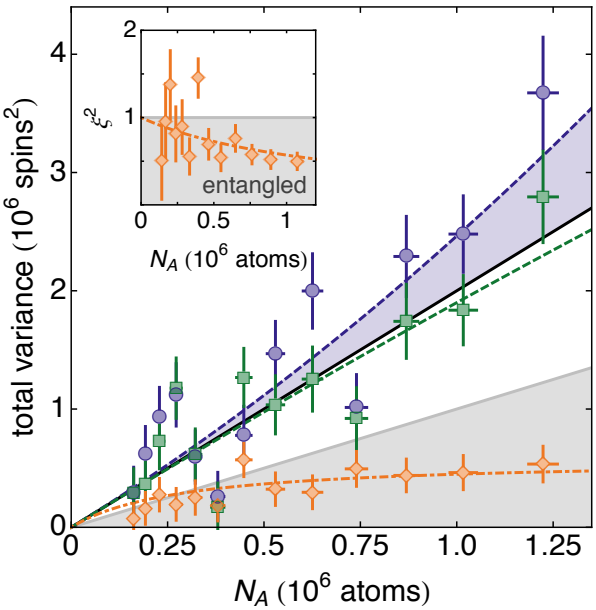

Figure 9.3: Noise scaling of total variance $\widetilde{\mathcal{V}}(N_A)$ of the first (blue circles) and second (green squares) QND measurement of the atomic spin distribution, and conditional variance $\widetilde{\mathcal{V}}_{2|1}$ (orange diamonds). Dashed lines are a quadratic fit, indicating the presence of technical noise in the input atomic state (blue shaded region). Black line indicates the expected quantum noise $\widetilde{\mathcal{V}} = 2fN_A$ due to an ideal TSS. Shaded area represents region with $\widetilde{\mathcal{V}}_{2|1} < fN_A$, indicating spin squeezing and entanglement. Orange dot-dashed curve is a fit to the expected conditional noise reduction with the SNR of the QND measurement as a free parameter. Inset: Semi-log plot of detected spin squeezing parameter. Dot-dashed curve is the expected spin squeezing calculated from the fitted SNR. Horizontal and vertical error bars represent 1σ statistical errors, and read-out noise has been subtracted from the data [139].

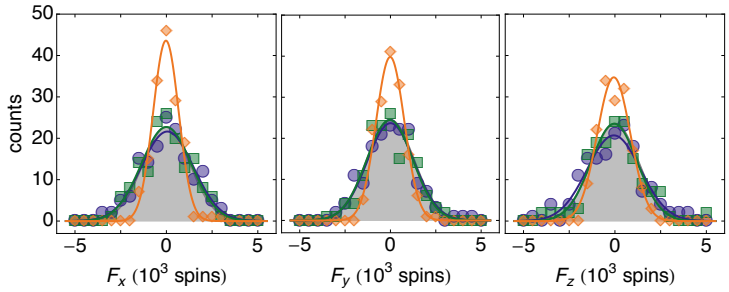

Figure 9.4: Individual spin measurements. Histograms of the measurements of each of the three spin components in the first round (blue circles) and second round (green squares) of the stroboscopic probe. We also show the conditional spin distribution $F_k^{(2)} - \chi F_k^{(1)}$ (orange diamonds), where $\chi \equiv \mathrm{cov}(F_k^{(1)}, F_k^{(2)})/(\Delta F_k^{(1)})^2$ is the degree of correlation. The gray shaded region indicates the expected distribution for an ideal input TSS, including detection noise. For presentation purposes an offset (between 5 and 10×10^3 spins) has been subtracted from the data [139].

persive atom number measurement (DANM) [6, 7] by applying a bias field $B_z = 100$ mG and optically pumping the atoms into $|f = 1, m_f = 1\rangle$ with circularly-polarized light propagating along the trap axis resonant with the $f = 1 \rightarrow f' = 1$ transition, and then probing with the Faraday rotation probe. The sequence of state-preparation, stroboscopic probing and DANM is repeated 12 times per trap loading cycle. In each sequence $\sim 15\%$ of the atoms are lost, mainly during the state-preparation, so that different values of N_A are sampled during each loading cycle. At the end of each cycle the measurement is repeated without atoms in the trap. The loading cycle is repeated 602 times to gather statistics.

To detect the MSS, we make two successive measurements of the collective spin vector $\hat{\mathbf{F}}$ for each state preparation. The first measurements give us a record of the input spin-distribution (blue points in Fig. 9.2(a)). The spread of these data includes contributions from technical noise in the atomic state preparation, and read-out noise in the detection system. We

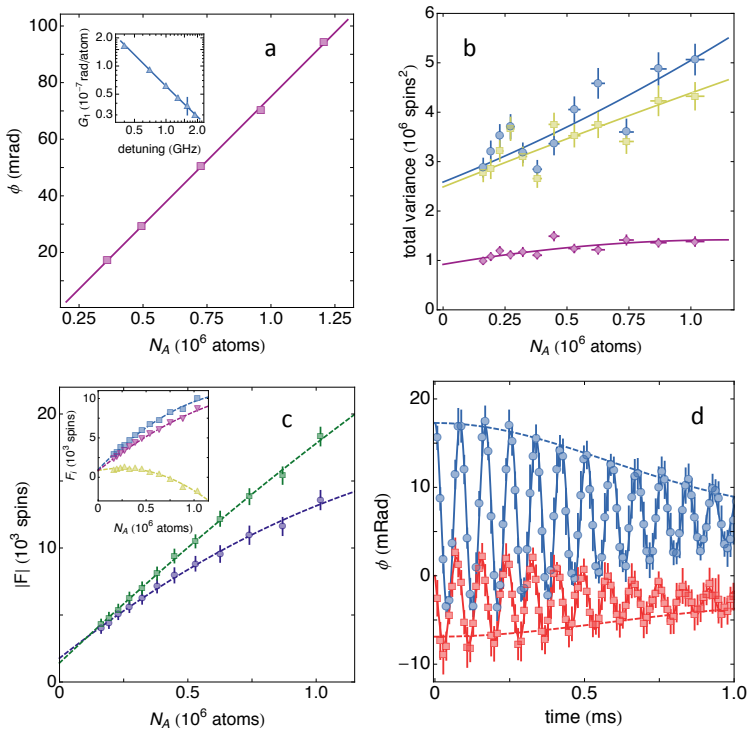

Figure 9.5: (a) Calibration of the G_1 coupling constant. We correlate the observed rotation angle ϕ against an independent measurement of atom number N_A via absorption imaging. Inset: from a fit to G_1 vs. the probe detuning Δ we estimate the effective atom-light interaction area A and tensor light shift G_2. (b) Noise scaling of total variance $\mathcal{V}_p = \mathrm{Tr}(\Gamma_p)$ of the first two QND measurements, and conditional variance $\mathcal{V}_{2|1} = \mathrm{Tr}(\Gamma_{2|1})$. Blue circles: first measurement. Green squares: second measurement. Purple diamonds: conditional variance. (c) Length of spin vector $|\hat{F}|$ detected by the first (blue circles) and second (green squares) measurement. Inset: Mean of individual spin components $\hat{F}_i$ detected by the first measurement. Blue square: mean $\hat{F}_\mathrm{z}$. Purple diamonds: mean $\hat{F}_\mathrm{y}$. Green triangles: mean $\hat{F}_\mathrm{x}$. (d) Free induction decay (FID) measurement of the applied magnetic field using atoms as an in-situ vector magnetometer. Blue circles: input $\hat{F}_\mathrm{z}$-polarized atomic state. Red circles: input $\hat{F}_\mathrm{y}$-polarized atomic state. Solid line: fit described by Eq. (9.4). Dashed line: gaussian envelope of FID signal.

select from the first measurements the events near the mean (orange points in Fig. 9.2(a)), i.e. a low-dispersion subset of our data [140]. The second measurement of these selected events, shown in Fig. 9.2(b), is analyzed to determine if the selected subset satisfies the criterion for a MSS.

The selection procedure is illustrated in Figs. 9.2(a) & (b). We select data from the first QND measurement of the collective spin vector using the criterion $|\hat{\mathbf{F}} - \langle\hat{\mathbf{F}}\rangle|^2/N_A < C$, where C is a chosen cutoff parameter. We calculate $\xi^2 = \widetilde{\mathcal{V}}_2/(fN_A)$ from the second QND measurement, where $\widetilde{\mathcal{V}}_2$ is the total variance after subtraction the read-out noise, $\widetilde{\mathcal{V}}_2 \equiv \mathcal{V}_2 - \mathcal{V}_0$. Here $\mathcal{V}_2 \equiv \mathrm{Tr}(\Gamma_2)$, where Γ_2 is the covariance matrix corresponding to the second QND measurement, and the read-out noise $\mathcal{V}_0 \equiv \mathrm{Tr}(\Gamma_0)$ is quantified by repeating the measurement without atoms in the trap and calculating the corresponding covariance matrix Γ_0. For this experiment $\mathcal{V}_0 = 9.2 \pm 0.3 \times 10^5$ spins^2. This selection procedure is a form of measurement-induced spin squeezing [86], verified by the second QND measurement. In Fig. 9.2(c) we show ξ^2, computed on the second measurements of the selected events, as a function of the cutoff parameter C for data from a sample with $N_A = 1.1 \times 10^6$. With a cutoff $C = 0.75$ we measure $\xi^2 = 0.69 \pm 0.05$, detecting entanglement with 5σ significance.

We cross-check our results by repeating the experiment under near-identical conditions and analyzing the conditional covariance between successive vector spin measurements. This allows us to deterministically prepare a MSS without filtering our data. For these measurements the applied magnetic field had a magnitude $B = 15.9$ mG, giving a Larmor period of $T_L = 90 \pm 3$ μs, and we repeated the experiment 155 times. Correlations between successive measurements of the same spin component $\hat{F}_k$ allows us to predict the outcome of the second measurements $F_k^{(2)}$ with a reduced conditional uncertainty. For a single parameter, the conditional variance is $\mathrm{var}(F_k^{(2)}|F_k^{(1)}) \equiv \mathrm{var}(F_k^{(2)} - \chi F_k^{(2)})$, where the correlation parameter $\chi \equiv \mathrm{cov}(F_k^{(1)}, F_k^{(2)})/\mathrm{var}(F_k^{(1)})$ minimizes the conditional variance [86]. This is illustrated in Fig. 9.4.

Conditional noise reduction is quantified via $\mathcal{V}_{2|1} = \mathrm{Tr}(\Gamma_{2|1})$, i.e. the total variance of the conditional covariance matrix $\Gamma_{2|1} \equiv \Gamma_2 - \Gamma_{2,1}\Gamma_1^{-1}\Gamma_{1,2}$

where $\Gamma_{1,2} \equiv \mathrm{cov}(\hat{F}_i^{(1)}, \hat{F}_j^{(2)})$ [80]. To estimate the atomic noise contribution we fit the polynomial $\mathcal{V}_\alpha(N_A) = \mathcal{V}_0 + 2N_A + cN_A^2$ to the measured data for the two QND measurements and the conditional variance [139]. We then calculate $\widetilde{\mathcal{V}}_\alpha = \mathcal{V}_\alpha - \mathcal{V}_0$, subtracting the read-out noise from the measured total variances.

In Fig. 9.3(a) we plot $\widetilde{\mathcal{V}}_{1,2}(N_A)$, the total measured variance as a function of the number of atoms in the trap for the first two QND measurements (blue circles and green squares). An ideal TSS has a total variance $\widetilde{\mathcal{V}} = \langle F^2 \rangle - \langle F \rangle^2 = 2N_A$ (black line in Fig. 9.3(a)). Due to technical noise contribution, the measured variance are higher than the ideal variance for TSS. The technical noise contribution to $\widetilde{\mathcal{V}}_1$ is indicated by the blue shaded region. A conditional variance $\widetilde{\mathcal{V}}_{2|1} < fN_A$ (shaded region) indicates spin squeezing and detects entanglement among the atoms [134, 126, 92, 125]. The measured conditional variance $\widetilde{\mathcal{V}}_{2|1}$ (orange diamonds) indicates that we produce spin squeezed states for $N_A > 5 \times 10^5$ atoms. The conditional noise for an ideal QND measurement is $\widetilde{\mathcal{V}}_{2|1} = 2N_A/(1+\zeta)$, where $\zeta = \frac{2}{3}G_1^2 N_L N_A$ is the signal-to-noise ratio (SNR) of the measurement [60, 86]. A fit to our data (orange dot-dashed line) gives $\widetilde{\mathcal{V}}_{2|1} = 2N_A/(1+b\zeta)$ with $b = 0.75 \pm 0.1$, where the reduction in SNR is due to technical noise in the detection system. In the inset of Fig. 9.3(a) we show the calculated spin squeezing parameter $\xi^2 = \widetilde{\mathcal{V}}_{2|1}/fN_A$.

With $N_A = 1.1 \times 10^6$ atoms we measure $\xi^2 = 0.50 \pm 0.09$, or 3dB of spin squeezing detected with 5σ significance.This level of squeezing implies that at least 5.5×10^5 atoms are entangled with at least one other atom in the ensemble [92]. While multi-partite entanglement may also be generated in the ensemble [26], it is not detected by our spin-squeezing inequality [141]. We have demonstrated the conditional preparation of a macroscopic singlet state (MSS) via stroboscopic QND measurement in an unpolarized ensemble with more than one million laser-cooled atoms. We observe 3dB of spin squeezing and detect entanglement with 5σ statistical significance using a generalized spin squeezing inequality, indicating that at least half the atoms in the sample have formed singlets [134, 126, 92, 125]. Our techniques complement existing experimental methods [11, 12, 14, 13, 15], can

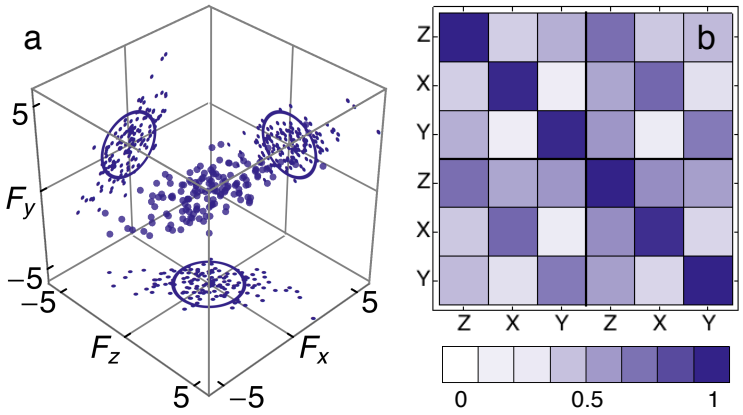

Figure 9.6: (a) Measured spin distribution (in units of 10^3 spins) of the input TSS following the state preparation procedure described in the main text. (b) Correlation matrix between two consecutive three-component collective spin measurements showing strong correlations between measurements of each spin component $\hat{F}_i$.

be readily adapted to measurements of quantum lattice gases [21, 20] and spinor condensates [133]. In future work we aim to combine our measurement with quantum control techniques [28] to produce an unconditionally squeezed macroscopic singlet centered at the origin [92], and to use our spatially extended MSS for magnetic field gradiometry [27]. Due to its SU(2) invariance, the MSS is a good candidate for storing quantum information in a decoherence–free subspace [142] and for sending information independent of a reference direction [143].

9.1.1 Probe calibration

The light-atom coupling constant G_1 is calibrated by correlating the DANM signal with an independent count of the atom number via absorption imaging [41, 6, 86]. In Fig. 9.5(a) we show the calibration data. We find $G_1 = 9.0 \pm 0.1 \times 10^{-8}$ radians per spin at the detuning $\Delta = -700$ MHz. In

the inset of Fig. 9.5(a) we plot G_1 vs. Δ. We fit this data to find the effective atom-light interaction area A [41], from which we estimate the tensor light shift $G_2 = -4.1^{+0.4}_{-0.5} \times 10^{-9}$ radians per spin at $\Delta = -700$ MHz.

9.1.2 Noise scaling & Read-Out Noise

To estimate the atomic noise contribution to the observed total variance $\mathcal{V} = \mathrm{Tr}(\Gamma)$ of the QND measurements we fit the polynomial $\mathcal{V}(N_A) = \mathcal{V}_0 + 2N_A + cN_A^2$ to the measured data, and calculate $\widetilde{\mathcal{V}}_p = \mathcal{V}_p - \mathcal{V}_0$, subtracting the read-out noise $\mathcal{V}_0$ from the measured total variances. The data and resulting fits are shown in Fig. 9.5(b). The fit to the first (second) measurement yields $\mathcal{V}_0 = 2.59 \pm 0.08 \times 10^6$ ($2.49 \pm 0.08 \times 10^6$) and $c = 4 \pm 2 \times 10^{-7}$ ($1 \pm 2 \times 10^{-7}$). We fit the polynomial $\mathcal{V}_{2|1}(N_A) = \mathcal{V}_0 + aN_A + cN_A^2$ to the measured conditional variance, giving $\mathcal{V}_0 = 9.2 \pm 0.8 \times 10^5$, $a = 0.9 \pm 3$ and $c = -4 \pm 2 \times 10^{-7}$, indicating the presence of some correlated technical noise in the detection system.

9.1.3 Residual polarization

We observe a small residual atomic polarization due to atoms that are not entangled in the mascroscopic singlet state. In Fig. 9.5(c) we plot the length of the spin vector $|\hat{F}|$ detected in the two measurements. With $N_A = 1.1 \times 10^6$ atoms, we observe a maximum $|F| = 13.3 \pm 0.2 \times 10^3$ ($18.3 \pm 0.2 \times 10^3$) spins for the first (second) measurement, i.e. a residual polarization $|\hat{F}|/(fN_A) = 1.66 \pm 0.02 \times 10^{-3}$. In principle with these values we could achieve 20dB of spin squeezing, entangling up to 99% of the atoms in a macroscopic singlet, before back-action due to the spin uncertainty relations limits the achievable squeezing. This residual polarization could be removed by adding a feedback loop to the measurement sequence [28], which would produce an unconditionally squeezed macroscopic singlet centered at the origin.

9.1.4 Magnetic field calibration

We measure the applied magnetic field using the atoms as an in-situ vector magnetometer. Our technique is described in detail in Ref. [115]. We polarize the atoms via optically pumping along first $\hat{F}_\mathrm{z}$ and then $\hat{F}_\mathrm{y}$, and observe the free induction decay (FID) of the resulting Larmor precession using the Faraday rotation probe. We model density distribution along the length of the trap with a gaussian $A\exp(-(z-z_0)^2/2\sigma^2)$, with an RMS width $\sigma = 2.68 \pm 0.3$ mm. A typical density profile and gaussian fit is shown in Fig. 9.5(d). This leads to observed signals for the two input states

$$\theta(t) = \frac{G_1}{B^2}\begin{cases} \left(B_z^2 + \left(B_x^2 + B_y^2\right)\cos\omega \exp\left(-t^2/T_2^2\right)\right) F_z(0) \\ \left(B_y B_z \left(1 - \cos\omega \exp\left(-t^2/T_2^2\right)\right) + B_x B \sin\omega \exp\left(-t^2/T_2^2\right)\right) F_y(0) \end{cases} \tag{9.4}$$

where $\omega = \gamma B t$, $B = |\mathbf{B}|$, and $\gamma = \mu_B g_f/\hbar$ is the atomic gyromagnetic ratio. By fitting theses signals, we extract the vector field $\mathbf{B}$ and the FID transverse relaxation time $T_2 = 1/(\sigma\gamma\partial B/\partial z)$. For the data shown we find $B_x = 9.6 \pm 0.4$ mG, $B_y = 9.7 \pm 0.4$ mG, $B_z = 9.9 \pm 0.1$ mG and $T_2 = 745 \pm 45$ μs.

9.1.5 Input state

In Fig. 9.6(a) we plot the spin distribution $\mathbf{F}^{(1)}$ of the collective spin of a sample with $N_A = 1.4 \times 10^6$ atoms measured by the first three probe pulses. We measure an initial spin covariance matrix of

$$\Gamma_1 = \begin{pmatrix} 1.90 & 1.10 & 1.10 \\ 1.10 & 1.40 & 0.81 \\ 1.10 & 0.81 & 1.30 \end{pmatrix} \times 10^6 \,\mathrm{spins}^2. \tag{9.5}$$

For comparison, an ideal TSS would have $\Gamma = \mathrm{diag}(0.93, 0.93, 0.93) \times 10^6$ spins^2 with the same number of atoms. The larger measured variances, and non-zero covariances, in Γ_1 indicate the presence of atomic technical noise due to imperfect state preparation and shot-to-shot fluctuations in the atom

number and applied magnetic field.

9.1.6 Measurement correlations

In Fig. 9.6(b) we plot the correlations $\rho_{ij} \equiv \mathrm{cov}(\hat{F}_i, \hat{F}_j)/\Delta\hat{F}_i\Delta\hat{F}_j$ between the first six QND measurements. The off-diagonal elements indicate that successive measurements of the same spin component $\hat{F}_k$ are well correlated. This allows us to predict the outcome of the second measurements $F_k^{(2)}$ with a reduced conditional uncertainty. The residual correlation between measurements of different spin components is due to correlated technical noise in the atomic state preparation, and in the detection system.

10
Conclusions and outlook

The main feature which is common in all the experiments presented in this dissertation is the light-atom interaction. Then we can divide what we have studied in two categories. The first is the magnetormetry and high precision measurement where we use atoms as sensitive devices to measure the magnetic field with high spatial resolution and the other is the measurement induced generation of entanglement and manipulation of the atomic states to generate new exotic quantum states in cold atomic ensembles.

Atoms are magnetically sensitive system which make them interesting for various tasks. One of them would be to use atoms as a sensor to measure the magnetic field. We have demonstrated a cold-atom magnetometer with sub-nT sensitivity, 20 μm transverse spatial resolution and 1 ms temporal resolution. The technique is using free induction decay signal to get simultaneous information about the three field components plus one gradient component. This technique is useful for experiments where inferring information about the field in a non-destructive manner is of interest.

Developing this technique to measure all components of angular momentum was essential to pursue spin cooling and macroscopic spin singlets experiments. Having access to control and monitor three components of the magnetic field made it possible to apply a coherent rotation scheme to the atomic spins. This allow us to have access to all components of angular momentum.

We demonstrate that incoherent feedback cooling can be used as a way to reduce the entropy of the atomic spin. The difference from the traditional

cooling is that in traditional cooling, the system of interest is coupled to a cold reservoir which allow the energy and entropy to leave the system. Feedback cooling, as we have used, is a non-thermal process to remove entropy, which make the cooling not dependent on reservoir temperature. We reached reduction of 12 dB in the total variance or a reduction in phase-space volume by a factor of 63. We also developed a realistic quantum control theory to incorporate experimental imperfection. This technique can be used to generate on-demand unconditional spin squeezing and generation of quantum correlated states of ultra-cold atomic gases.

The other experiment presented in this thesis which also involves light-atom interaction is the macroscopic spin singlet generation in a cold atomic ensemble. Such states are of fundamental interest since they are appearing as ground state of many fundamental spin model systems such as high-temperature superconductors and anti ferromagnetic materials. We generalized the technique of quantum non-demolition measurement that has been used to perform spin squeezing on one component of angular momentum for all components of angular momentum. To reach this goal we have used thermal spin state as initial state which is a state with total angular momentum equal to zero. This characteristic of the initial state would allow the reduction of the uncertainty for all components of angular momentum simultaneously. We observe 3 dB of spin squeezing in total angular momentum with 5σ statistical significance.

As mentioned before, generating such state is of interest both in fundamental and applied science. One immediate application of such states is to use them as gradiometer. Their invariance under rotation and their sensitivity to the inhomogeneous magnetic field make them a sensitive tool to get information about gradient of field with high spatial resolution. Spin squeezing via QND measurements in such systems implies entanglement of a macroscopic number of atoms. ability to generate such long range entanglement is of fundamental interest and as outlook it would be interesting to investigate the type of entanglement generated in such states. Moreover one can apply the feedback control scheme to reach unconditional squeezing in generating macroscopic spin singlets.

A
Appendix

In this appendix, we discuss the proof of the update rule of the measurement. This update rule is used in nearly all covariance matrix calculations. We are, however, unaware of a detailed explanation, which we provide here.

A.1 preliminaries

The proof comes from statistics and requires us to define some statistical concepts. Our proof follows that given in [144]. We will distinguish between random variables, written with capital letters, and the values they take on, written with lowercase letters. For example, given a random variable X with probability distribution (technically the probability density function) $P(X)$, we would write the probability of obtaining a value $X = x$ in the range $0 \leq x \leq 1$ as $\int_0^1 P(X = x)dx$.

The expectation $E[X]$, which in physics is written $\langle X \rangle$, is defined as

$$E[X] = \int P(X = x)xdx. \tag{A.1}$$

More generally, the expectation value for a function of a random variable $f(X)$ is

$$E[f(X)] = \int P(X = x)f(x)dx. \tag{A.2}$$

Given two random variables X_1 and X_2, described by a joint distribution $P(X_1, X_2)$, a conditional distribution is written $P(X_1|X_2 = x_2)$, indicating

the distribution of X_1 for the cases in which X_2 takes on the value x_2. We use the same notation to indicate the conditional expectation value:

$$E[f(X_1)|X_2 = x_2] \equiv \int P(X_1|X_2 = x_2)f(x_1)dx_1. \tag{A.3}$$

The conditional expectation is simply the expectation computed using the conditional distribution.

The Fourier transform of a distribution, known as the characteristic function, is very useful and will be central to the proof of the update rule. For a single variable Z, the characteristic function is defined as

$$\phi(t) = E[e^{itZ}] = \int P(Z = z)e^{itz}dz. \tag{A.4}$$

The generalization is straightforward: For a random vector $\mathbf{X}$ of dimension n, the characteristic function is

$$\phi(\mathbf{k}) = E[e^{i\mathbf{k}\cdot\mathbf{X}}] = \int P(\mathbf{X} = \mathbf{x})e^{i\mathbf{k}\cdot\mathbf{x}}d^n x. \tag{A.5}$$

Because the Fourier transform is invertible, the characterization function is unique.

All of our distributions will be Gaussian, i.e. "normal" in statistical language. The Gaussian distribution for a single variable Z is

$$G(Z = z, \mu, \sigma) \equiv \frac{1}{\sigma\sqrt{2\pi}} \exp(-\frac{(z-\mu)^2}{2\sigma^2}) \tag{A.6}$$

where the parameter μ is the mean or expectation of the distribution, the parameter σ is its standard deviation; the variance of distribution is σ^2. The characteristic function for this distribution is

$$\phi(t) = \int e^{-itz}G(z, \mu, \sigma)dz = \exp[i\mu t - \frac{1}{2}\sigma^2 t^2] \tag{A.7}$$

A Gaussian distribution for a vector random variable $\mathbf{X}$ is similarly defined:

$$G(\mathbf{X}, \boldsymbol{\mu}, \Gamma) \propto \exp[(\mathbf{X} - \boldsymbol{\mu}) \cdot \Gamma^{-1} \cdot (\mathbf{X} - \boldsymbol{\mu})]. \tag{A.8}$$

We can express this using as a basis $\mathbf{V}_l$, the orthonormal eigenvectors of Γ, so that Γ is diagonal in this basis. Writing $X_l \equiv \mathbf{X} \cdot \mathbf{V}_l$ and $\mu_l \equiv \mathbf{V} \cdot \boldsymbol{\mu}_l$, we have

$$\begin{aligned} G(\mathbf{X}, \boldsymbol{\mu}, \Gamma) &\propto \prod_l \exp[(X_l - \mu_l)\Gamma_{ll}^{-1}(X_l - \mu_l)] \\ &= \prod_l G(X_l, \mu_l, \Gamma_{ll}) \end{aligned} \tag{A.9}$$

The characteristic function for this distribution is

$$\begin{aligned} \phi(\mathbf{k}, \boldsymbol{\mu}, \Gamma) &= \int e^{i\mathbf{k}\cdot\mathbf{x}} G(\mathbf{X}, \boldsymbol{\mu}, \Gamma) d^n x. \\ \phi(\mathbf{k}, \boldsymbol{\mu}, \Gamma) &= \prod_{i=1}^{n} \phi(k_i, \mu_i, \Gamma_{ii}) \end{aligned} \tag{A.10}$$

where

$$\phi(k_i, \mu_i, \Gamma_{ii}) = \exp[(i\mu_i k_i - \frac{1}{2}\Gamma_{ii} k_i^2)]. \tag{A.11}$$

From equations A.10 and A.11, it is straightforward to extract the generalized characteristic function as

$$\phi(\mathbf{k}, \boldsymbol{\mu}, \Gamma) = \exp[i\mathbf{k} \cdot \boldsymbol{\mu} - \frac{1}{2}\mathbf{k} \cdot \Gamma \cdot \mathbf{k}]. \tag{A.12}$$

In probability theory, to say that two events are independent means that the occurrence of one does not affect the probability of the other. Similarly, two random variables X, Y are independent if the realisation of one does not affect the probability distribution of the other, so that the joint distribution factors $P(X, Y) = P(X)P(Y)$. Two variables are said to be uncorrelated if their covariance $\mathrm{cov}(X, Y)$ vanishes. For Gaussian distributions, uncorrelation implies independence.

We now show that for random variables A, B, with covariance matrices $\mathrm{cov}(A, A) \equiv \Gamma_{AA}$, $\mathrm{cov}(B, B) \equiv \Gamma_{BB}$ and $\mathrm{cov}(A, B) \equiv \Gamma_{AB}$, that B and $A - \Gamma_{AB}\Gamma_{BB}^{-}B$ are uncorrelated, i.e., that $\mathrm{cov}(B, A - \Gamma_{AB}\Gamma_{BB}^{-}B) = 0$.

Proof: The covariance follows the rules of the linear algebra, so we can

write

$$\mathrm{cov}(B_i, A_j - [\Gamma_{AB}\Gamma_{BB}^{-}B]_j) = \mathrm{cov}(B_i, A_j) - \mathrm{cov}(B_i, [\Gamma_{AB}\Gamma_{BB}^{-}B]_j) \quad \text{(A.13)}$$

where $(\Gamma_{AB})_{jk} = \mathrm{cov}(A_j, B_k)$ and $(\Gamma_{BB}^{-})_{kl} = \delta_{kl}[\mathrm{cov}(B_l, B_l)]^{-1}$, giving

$$[\Gamma_{AB}\Gamma_{BB}^{-}B]_j = \mathrm{cov}(A_j, B_k)\delta_{kl}\frac{1}{\mathrm{cov}(B_l, B_l)}B_l \quad \text{(A.14)}$$

and thus

$$\begin{aligned} \mathrm{cov}(B_i, [\Gamma_{AB}\Gamma_{BB}^{-}B]_j) &= \mathrm{cov}(A_j, B_k)\delta_{kl}\frac{1}{\mathrm{cov}(B_l, B_l)}\mathrm{cov}(B_i, B_l) \\ &= \Gamma_{AB}\Gamma_{BB}^{-}\Gamma_{BB} \\ &= \Gamma_{AB} \end{aligned} \quad \text{(A.15)}$$

From equation A.13 and A.15, we conclude that $\mathrm{cov}[B, A - \Gamma_{AB}\Gamma_{BB}^{-}B] = 0$ and B and $A - \Gamma_{AB}\Gamma_{BB}^{-}B$ are uncorrelated and thus independent.

Here we will show that $\mathrm{cov}(A - \Gamma_{12}\Gamma_{22}^{-}B) = \Gamma_{11} - \Gamma_{12}\Gamma_{22}^{-}\Gamma_{21}$. Note that A is labeled with 1 and B is labeled with 2 in the covariance matrix.

The covariance between two scalar variables a and b is defined as $\mathrm{cov}(a, b) = \langle ab\rangle - \langle a\rangle\langle b\rangle$. In the case of the multi variable A, covariance of A is defined as $\mathrm{cov}(A)_{ij} = \mathrm{cov}(A_i, A_j)$. With this background material we will proceed to calculate $\Gamma_{ij} = \mathrm{cov}(A - \Gamma_{12}\Gamma_{22}^{-}B)_{ij}$. In this part we have slightly modified the notation of the indices of Γ_{12} to include indices defined in the covariance matrix definition. In this new notation we moved the subscript to superscript and added indices of the covariance matrix definition in the subscript Γ_{ij}^{12}.

$$\begin{aligned} \Gamma_{ij} &= \mathrm{cov}(A_i - \Gamma_{ib}^{12}\Gamma_{bc}^{22^-}B_c, A_j - \Gamma_{jd}^{12}\Gamma_{de}^{22^-}B_e) \\ &= \mathrm{cov}(A_i, A_j) + \mathrm{cov}(\Gamma_{ib}^{12}\Gamma_{bc}^{22^-}B_c, \Gamma_{jd}^{12}\Gamma_{de}^{22^-}B_e) - \mathrm{cov}(A_i, \Gamma_{jd}^{12}\Gamma_{de}^{22^-}B_e) \\ &\quad -\mathrm{cov}(A_j, \Gamma_{ib}^{12}\Gamma_{bc}^{22^-}B_c) \end{aligned} \quad \text{(A.16)}$$

The second term of the equation A.16 can be simplified as follows

$$\begin{aligned}
\operatorname{cov}(\Gamma^{12}_{ib}\Gamma^{22^-}_{bc}B_c, \Gamma^{12}_{jd}\Gamma^{22^-}_{de}B_e) &= \Gamma^{12}_{ib}\Gamma^{22^-}_{bc}\Gamma^{12}_{jd}\Gamma^{22^-}_{de}\operatorname{cov}(B_c, B_e) \\
&= \Gamma^{12}_{ib}\Gamma^{22^-}_{bc}\Gamma^{12}_{jd}\Gamma^{22^-}_{de}\Gamma^{22}_{ce} \\
&= \Gamma^{12}_{ib}\Gamma^{12}_{jd}\Gamma^{22^-}_{de}\delta_{be} \\
&= \Gamma^{12}_{ie}\Gamma^{12}_{jd}\Gamma^{22^-}_{de} \\
&= \operatorname{cov}(A_i, \Gamma^{12}_{jd}\Gamma^{22^-}_{de}B_e) \qquad \text{(A.17)}
\end{aligned}$$

The second term and the third term of equation A.16 cancel each other and this will lead to

$$\operatorname{cov}(A - \Gamma_{12}\Gamma^{-}_{22}B)_{ij} = \operatorname{cov}(A_i, A_j) - \operatorname{cov}(A_j, \Gamma^{12}_{ib}\Gamma^{22^-}_{bc}B_c) \quad \text{(A.18)}$$

$$\operatorname{cov}(A - \Gamma_{12}\Gamma^{-}_{22}B) = \Gamma_{11} - \Gamma_{12}\Gamma^{-}_{22}\Gamma_{21}. \qquad \text{(A.19)}$$

A.2 Conditional multivariate distribution

One can use the characteristic function of one Gaussian random vector given another Gaussian random vector, to describe the conditional Gaussian distribution.

$$\begin{aligned}
\phi(\mathbf{k}|\mathbf{X_2} = \mathbf{a}) &= E[e^{i\mathbf{k}\cdot\mathbf{X}_1}|\mathbf{X}_2 = \mathbf{a}] \\
&= E[e^{i\mathbf{k}\cdot\mathbf{X}_1 - i(\mathbf{k}\cdot\Gamma_{12}\Gamma^{-}_{22}\cdot\mathbf{X_2}) + i(\mathbf{k}\cdot\Gamma_{12}\Gamma^{-}_{22}\cdot\mathbf{X_2})}|\mathbf{X}_2 = \mathbf{a}] \\
&= e^{i(\mathbf{k}\cdot\Gamma_{12}\Gamma^{-}_{22}\cdot\mathbf{a})}E[e^{i(\mathbf{k}\cdot\mathbf{X}_1 - \mathbf{k}\cdot\Gamma_{12}\Gamma^{-}_{22}\cdot\mathbf{X_2})}|\mathbf{X}_2 = \mathbf{a}] \\
&= e^{i(\mathbf{k}\cdot\Gamma_{12}\Gamma^{-}_{22}\cdot\mathbf{a})}E[e^{i(\mathbf{k}\cdot\mathbf{X}_1 - \mathbf{k}\cdot\Gamma_{12}\Gamma^{-}_{22}\cdot\mathbf{X_2})}] \qquad \text{(A.20)} \\
&= e^{i(\mathbf{k}\cdot\Gamma_{12}\Gamma^{-}_{22}\cdot\mathbf{a})}E[e^{i\mathbf{k}\cdot(\mathbf{X}_1 - \Gamma_{12}\Gamma^{-}_{22}\cdot\mathbf{X_2})}] \qquad \text{(A.21)}
\end{aligned}$$

Where Eq. (A.20) follows from the independence of $\mathbf{X}_2$ and $\mathbf{X}_1 - \Gamma_{12}\Gamma^{-}_{22}\cdot\mathbf{X}_2$. We recognize $E[\exp[i\mathbf{k}\cdot(\mathbf{X}_1 - \Gamma_{12}\Gamma^{-}_{22}\cdot\mathbf{X_2})]]$ as the characteristic function of the random variable $\mathbf{X}_1 - \Gamma_{12}\Gamma^{-}_{22}\cdot\mathbf{X_2}$. Considering that this has mean

$\boldsymbol{\mu}_1 - \Gamma_{12}\Gamma_{22}^{-} \cdot \boldsymbol{\mu}_2$ and covariance matrix $\Gamma_{11} - \Gamma_{12}\Gamma_{22}^{-}\Gamma_{12}'$, we use Eq. (A.12) to write this as

$$\begin{aligned} \phi(\mathbf{k}|\mathbf{X_2} = \mathbf{a}) &= e^{i(\mathbf{k} \cdot \Gamma_{12}\Gamma_{22}^{-} \cdot \mathbf{a})} E[e^{i\mathbf{k} \cdot (\mathbf{X}_1 - \Gamma_{12}\Gamma_{22}^{-} \cdot \mathbf{X_2})}] \\ &= e^{i(\mathbf{k} \cdot \Gamma_{12}\Gamma_{22}^{-} \cdot \mathbf{a})} \\ &\quad \times e^{i\mathbf{k} \cdot (\boldsymbol{\mu}_1 - \Gamma_{12}\Gamma_{22}^{-} \cdot \boldsymbol{\mu}_2) - \frac{1}{2}\mathbf{k} \cdot (\Gamma_{11} - \Gamma_{12}\Gamma_{22}^{-}\Gamma_{12}') \cdot \mathbf{k}} \\ &= e^{i\mathbf{k} \cdot [\boldsymbol{\mu}_1 + \Gamma_{12}\Gamma_{22}^{-} \cdot (\mathbf{a} - \boldsymbol{\mu}_2)] - \frac{1}{2}\mathbf{k} \cdot (\Gamma_{11} - \Gamma_{12}\Gamma_{22}^{-}\Gamma_{12}') \cdot \mathbf{k}}. \end{aligned} \quad \text{(A.22)}$$

This is now recognizable, again using Eq. (A.12), as the characteristic function of the normal distribution with mean $\boldsymbol{\mu}_1 + \Gamma_{12}\Gamma_{22}^{-} \cdot (\mathbf{a} - \boldsymbol{\mu}_2)$ and covariance matrix $\Gamma_{11} - \Gamma_{12}\Gamma_{22}^{-}\Gamma_{12}'$, i.e.

$$G(\mathbf{X}_1|\mathbf{X}_2 = \mathbf{a}) = N(\boldsymbol{\mu}_1 + \Gamma_{12}\Gamma_{22}^{-}(\mathbf{a} - \boldsymbol{\mu}_2), \Gamma_{11} - \Gamma_{12}\Gamma_{22}^{-}\Gamma_{12}'). \quad \text{(A.23)}$$

This proves the "update rule" for measurements on multi-variate Gaussian distributions.

Bibliography

[1] F. Ya. Khalili V. B. Braginsky. *Quantum measurement*. Cambridge University Press, 1992.

[2] Timur Sh. Iskhakov, Maria V. Chekhova, Georgy O. Rytikov, and Gerd Leuchs. Macroscopic pure state of light free of polarization noise. *Phys. Rev. Lett.*, 106:113602, Mar 2011.

[3] Bhaskar Kanseri, Timur Iskhakov, Georgy Rytikov, Maria Chekhova, and Gerd Leuchs. Multiphoton nonclassical correlations in entangled squeezed vacuum states. *Phys. Rev. A*, 87:032110, Mar 2013.

[4] Bhaskar Kanseri, Timur Iskhakov, Ivan Agafonov, Maria Chekhova, and Gerd Leuchs. Three-dimensional quantum polarization tomography of macroscopic bell states. *Phys. Rev. A*, 85:022126, Feb 2012.

[5] Timur Sh. Iskhakov, Ivan N. Agafonov, Maria V. Chekhova, and Gerd Leuchs. Polarization-entangled light pulses of 10^5 photons. *Phys. Rev. Lett.*, 109:150502, Oct 2012.

[6] M. Koschorreck, M. Napolitano, B. Dubost, and M. W. Mitchell. Sub-projection-noise sensitivity in broadband atomic magnetometry. *Phys. Rev. Lett.*, 104:093602, Mar 2010.

[7] M. Koschorreck, M. Napolitano, B. Dubost, and M. W. Mitchell. Quantum nondemolition measurement of large-spin ensembles by dynamical decoupling. *Phys. Rev. Lett.*, 105:093602, Aug 2010.

[8] R. J. Sewell, M. Napolitano, N. Behbood, G. Colangelo, and M. W. Mitchell. Certified quantum non-demolition measurement of a macroscopic material system. *Nat Photon*, advance online publication:–, 05 2013.

[9] Maciej Lewenstein, Anna Sanpera, and Verònica Ahufinger. *Ultracold Atoms in Optical Lattices: Simulating quantum many-body systems*. OUP Oxford, Oxford, 2012.

[10] Maciej Lewenstein, Anna Sanpera, Veronica Ahufinger, Bogdan Damski, Aditi Sen(De), and Ujjwal Sen. Ultracold atomic gases in optical lattices: mimicking condensed matter physics and beyond. *Adv. Phys.*, 56(2):243–379, 2007.

[11] Stefan Trotzky, Yu-Ao Chen, Ute Schnorrberger, Patrick Cheinet, and Immanuel Bloch. Controlling and detecting spin correlations of ultracold atoms in optical lattices. *Phys. Rev. Lett.*, 105:265303, Dec 2010.

[12] Jonathan Simon, Waseem S. Bakr, Ruichao Ma, M. Eric Tai, Philipp M. Preiss, and Markus Greiner. Quantum simulation of antiferromagnetic spin chains in an optical lattice. *Nature*, 472(7343):307–312, 04 2011.

[13] S. Nascimbène, Y.-A. Chen, M. Atala, M. Aidelsburger, S. Trotzky, B. Paredes, and I. Bloch. Experimental realization of plaquette resonating valence-bond states with ultracold atoms in optical superlattices. *Phys. Rev. Lett.*, 108:205301, May 2012.

[14] Daniel Greif, Leticia Tarruell, Thomas Uehlinger, Robert Jördens, and Tilman Esslinger. Probing nearest-neighbor correlations of ultracold fermions in an optical lattice. *Phys. Rev. Lett.*, 106:145302, Apr 2011.

[15] Daniel Greif, Thomas Uehlinger, Gregor Jotzu, Leticia Tarruell, and Tilman Esslinger. Short-range quantum magnetism of ultracold fermions in an optical lattice. *Science*, 340(6138):1307–1310, 2013.

[16] R. Islam, C. Senko, W. C. Campbell, S. Korenblit, J. Smith, A. Lee, E. E. Edwards, C.-C. J. Wang, J. K. Freericks, and C. Monroe. Emergence and frustration of magnetism with variable-range interactions in a quantum simulator. *Science*, 340(6132):583–587, 2013.

[17] P. W. Anderson. The resonating valence bond state in la2cuo4 and superconductivity. *Science*, 235(4793):1196–1198, 1987.

[18] Leon Balents. Spin liquids in frustrated magnets. *Nature*, 464(7286):199–208, 03 2010.

[19] Etera R. Livine and Daniel R. Terno. Entanglement of zero-angular-momentum mixtures and black-hole entropy. *Phys. Rev. A*, 72:022307, Aug 2005.

[20] P. Hauke, R. J. Sewell, M. W. Mitchell, and M. Lewenstein. Quantum control of spin correlations in ultracold lattice gases. *Phys. Rev. A*, 87:021601, Feb 2013.

[21] Kai Eckert, Oriol Romero-Isart, Mirta Rodriguez, Maciej Lewenstein, Eugene S. Polzik, and Anna Sanpera. Quantum non-demolition detection of strongly correlated systems. *Nat Phys*, 4(1):50–54, 01 2008.

[22] Mohan Sarovar, Akihito Ishizaki, Graham R. Fleming, and K. Birgitta Whaley. Quantum entanglement in photosynthetic light-harvesting complexes. *Nat Phys*, 6(6):462–467, 06 2010.

[23] Jing Zhu, Sabre Kais, Al Aspuru-Guzik, Sam Rodriques, Ben Brock, and Peter J. Love. Multipartite quantum entanglement evolution in photosynthetic complexes. *The Journal of Chemical Physics*, 137(7), 2012.

[24] Dominik Heyers, Manuela Zapka, Mara Hoffmeister, John Martin Wild, and Henrik Mouritsen. Magnetic field changes activate the trigeminal brainstem complex in a migratory bird. *Proceedings of the National Academy of Sciences*, 107(20):9394–9399, 2010.

[25] B. P. Lanyon, J. D. Whitfield, G. G. Gillett, M. E. Goggin, M. P. Almeida, I. Kassal, J. D. Biamonte, M. Mohseni, B. J. Powell, M. Barbieri, A. Aspuru-Guzik, and A. G. White. Towards quantum chemistry on a quantum computer. *Nat Chem*, 2(2):106–111, 2010.

[26] Inigo Urizar-Lanz. *Quantum Metrology with Unpolarized Atomic Ensembles*. PhD thesis, Universidad del Pais Vasco, March 2014.

[27] I. Urizar-Lanz, Philipp Hyllus, I. Luis Egusquiza, Morgan W. Mitchell, and Géza Tóth. Macroscopic singlet states for gradient magnetometry. *Phys. Rev. A*, 88:013626, Jul 2013.

[28] N. Behbood, G. Colangelo, F. Martin Ciurana, M. Napolitano, R. J. Sewell, and M. W. Mitchell. Feedback cooling of an atomic spin ensemble. *Phys. Rev. Lett.*, 111:103601, Sep 2013.

[29] H. M. Wiseman and G. J. Milburn. Quantum theory of optical feedback via homodyne detection. *Phys. Rev. Lett.*, 70:548–551, Feb 1993.

[30] Stefano Mancini and Howard M. Wiseman. Optimal control of entanglement via quantum feedback. *Phys. Rev. A*, 75:012330, Jan 2007.

[31] Kurt Jacobs and Alireza Shabani. Quantum feedback control: how to use verification theorems and viscosity solutions to find optimal protocols. *Contemporary Physics*, 49(6):435–448, 2008.

[32] M.O. Scully and M.S. Zubairy. *Quantum Optics*. Cambridge University Press, 1997.

[33] Andrew C. Doherty, Salman Habib, Kurt Jacobs, Hideo Mabuchi, and Sze M. Tan. Quantum feedback control and classical control theory. *Phys. Rev. A*, 62:012105, Jun 2000.

[34] N. Behbood, F. Martin Ciurana, G. Colangelo, M. Napolitano, Géza Tóth, R. J. Sewell, and M. W. Mitchell. Generation of macroscopic singlet states in a cold atomic ensemble. *Phys. Rev. Lett.*, 113:093601, Aug 2014.

[35] R. Guenther. *Modern Optics*. Wiley, New York, 1990.

[36] Daniel A. Steck. Rubidium 87 D Line Data*, available online at http://steck.us/alkalidata (revision 2.1.4, 23 December 2010).*

[37] D. V. Kupriyanov, O. S. Mishina, I. M. Sokolov, B. Julsgaard, and E. S. Polzik. Multimode entanglement of light and atomic ensembles via off-resonant coherent forward scattering. *Phys. Rev. A*, 71:032348, Mar 2005.

[38] S. R. de Echaniz, M. Koschorreck, M. Napolitano, M. Kubasik, and M. W. Mitchell. Hamiltonian design in atom-light interactions with rubidium ensembles: A quantum-information toolbox. *Phys. Rev. A*, 77:032316, Mar 2008.

[39] J. M. Geremia, John K. Stockton, and Hideo Mabuchi. Tensor polarizability and dispersive quantum measurement of multilevel atoms. *Phys. Rev. A*, 73:042112, Apr 2006.

[40] Giorgio Colangelo, Robert J Sewell, Naeimeh Behbood, Ferran Martin Ciurana, Gil Triginer, and Morgan W Mitchell. Quantum atom–light interfaces in the gaussian description for spin-1 systems. *New J. Phys.*, 15(10):103007, 2013.

[41] M. Kubasik, M. Koschorreck, M. Napolitano, S. R. de Echaniz, H. Crepaz, J. Eschner, E. S. Polzik, and M. W. Mitchell. Polarization-based light-atom quantum interface with an all-optical trap. *Phys. Rev. A*, 79:043815, Apr 2009.

[42] C. J. Foot. *Atomic Physics*. Oxford University Press, 2005.

[43] Matthias Schulz. Tightly confined atoms in dipole traps*, Ph.D. thesis.* 2002.

[44] Herbert Crepaz. Trapping and cooling rubidium atoms for quantum information*, Ph.D. thesis.* 2007.

[45] Towards spin squeezing in cold atomic ensembles,*Ph.D. thesis*. ICFO-UPC, 2009.

[46] Marco Koschorreck. Generation of Spin Squeezing in an Ensemble of Cold Rubidium 87*, Ph.D. thesis*. Institute of Photonic Sciences, Mediterranean Technology Park, 08860 Castelldefels (Barcelona), Spain, 2011.

[47] Brice Dubost. Light-matter interaction with atomic ensembles,*Ph.D. thesis*. UPC-ICFO-Universite Paris Diderot, 2012.

[48] Patrick J Windpassinger, Marcin Kubasik, Marco Koschorreck, Axel Boisen, Niels Kjærgaard, Eugene S Polzik, and Jörg Helge Müller. Ultra low-noise differential ac-coupled photodetector for sensitive pulse detection applications. *Measurement Science and Technology*, 20(5):055301, 2009.

[49] Alfered Kastler. Optical methods for studying hertzian resonances. *Nobel Lectures, Physics 1963-1970, Elsevier Publishing Company, Amsterdam, 1972*, 1966.

[50] D. Budker, W. Gawlik, D. F. Kimball, S. M. Rochester, V. V. Yashchuk, and A. Weis. Resonant nonlinear magneto-optical effects in atoms. *Rev. Mod. Phys.*, 74:1153–1201, Nov 2002.

[51] D. Sheng, S. Li, N. Dural, and M. V. Romalis. Subfemtotesla scalar atomic magnetometry using multipass cells. *Phys. Rev. Lett.*, 110:160802, Apr 2013.

[52] L. Essen and J. V. L. Parry. An atomic standard of frequency and time interval: A caesium resonator. *Nature*, 176(4476):280–282, 1955.

[53] JM Geremia, John K. Stockton, and Hideo Mabuchi. Real-Time Quantum Feedback Control of Atomic Spin-Squeezing. *Science*, 304(5668):270–273, 2004.

[54] John K. Stockton, J. M. Geremia, Andrew C. Doherty, and Hideo Mabuchi. Robust quantum parameter estimation: Coherent magnetometry with feedback. *Phys. Rev. A*, 69:032109, Mar 2004.

[55] K. M. Birnbaum, A. Boca, R. Miller, A. D. Boozer, T. E. Northup, and H. J. Kimble. Photon blockade in an optical cavity with one trapped atom. *Nature*, 436(7047):87–90, 2005.

[56] Clement Sayrin, Igor Dotsenko, Xingxing Zhou, Bruno Peaudecerf, Theo Rybarczyk, Sebastien Gleyzes, Pierre Rouchon, Mazyar Mirrahimi, Hadis Amini, Michel Brune, Jean-Michel Raimond, and Serge Haroche. Real-time quantum feedback prepares and stabilizes photon number states. *Nature*, 477(7362):73–77, 2011.

[57] M. Koschorreck. *Generation of Spin Squeezing in an Ensemble of Cold Rubidium 87*. PhD thesis, Institute of Photonic Sciences (ICFO), 2010.

[58] Barbara Kraus, Klemens Hammerer, Géza Giedke, and J. Ignacio Cirac. Entanglement generation and Hamiltonian simulation in continuous-variable systems. *Phys. Rev. A*, 67:042314, Apr 2003.

[59] Lars Bojer Madsen and Klaus Mølmer. Spin squeezing and precision probing with light and samples of atoms in the gaussian description. *Phys. Rev. A*, 70:052324, Nov 2004.

[60] K. Hammerer, K. Mølmer, E. S. Polzik, and J. I. Cirac. Light-matter quantum interface. *Phys. Rev. A*, 70:044304, Oct 2004.

[61] Klaus Mølmer and Lars Bojer Madsen. Estimation of a classical parameter with gaussian probes: Magnetometry with collective atomic spins. *Phys. Rev. A*, 70:052102, Nov 2004.

[62] Marco Koschorreck and Morgan W Mitchell. Unified description of inhomogeneities, dissipation and transport in quantum light-atom interfaces. *J. Phys. B*, 42(19):195502, 2009.

[63] J. von Neumann. Matematische grandlagen der quantunmechanik. *Berlin*, 1932.

[64] M. D. Srinivas. *Measurements and quantum probabilities*. University Press (India) Limited, 2001.

[65] M. S. Hussein J. C. A. Barata. The moore-penrose pseudoinverse, a tutorial review of the theory. *ArXiv 1110.6882v1*, 2011.

[66] A. D. Ludlow, T. Zelevinsky, G. K. Campbell, S. Blatt, M. M. Boyd, M. H. G. de Miranda, M. J. Martin, J. W. Thomsen, S. M. Foreman, Jun Ye, T. M. Fortier, J. E. Stalnaker, S. A. Diddams, Y. Le Coq, Z. W. Barber, N. Poli, N. D. Lemke, K. M. Beck, and C. W. Oates. Sr lattice clock at 17th fractional uncertainty by remote optical evaluation with a Ca clock. *Science*, 319(5871):1805–1808, 2008.

[67] Han-Ning Dai, Han Zhang, Sheng-Jun Yang, Tian-Ming Zhao, Jun Rui, You-Jin Deng, Li Li, Nai-Le Liu, Shuai Chen, Xiao-Hui Bao, Xian-Min Jin, Bo Zhao, and Jian-Wei Pan. Holographic storage of biphoton entanglement. *Phys. Rev. Lett.*, 108:210501, May 2012.

[68] D Budker and M Romalis. Optical magnetometry. *Nature Phys.*, 3:227 – 234, 2007.

[69] Peter D. D. Schwindt, Svenja Knappe, Vishal Shah, Leo Hollberg, John Kitching, Li-Anne Liew, and John Moreland. Chip-scale atomic magnetometer. *Applied Physics Letters*, 85(26):6409–6411, 2004.

[70] M. Vengalattore, J. M. Higbie, S. R. Leslie, J. Guzman, L. E. Sadler, and D. M. Stamper-Kurn. High-resolution magnetometry with a spinor bose-einstein condensate. *Phys. Rev. Lett.*, 98(20):200801, May 2007.

[71] M. Koschorreck, M. Napolitano, B. Dubost, and M. W. Mitchell. High resolution magnetic vector-field imaging with cold atomic ensembles. *Appl. Phys. Lett.*, 98(7):074101, 2011.

[72] Stephan Wildermuth, S Hofferberth, I Lesanovsky, S Groth, P Krüger, Jörg Schmiedmayer, and I Bar-Joseph. Sensing electric and magnetic fields with bose-einstein condensates. *Applied Physics Letters*, 88:264103, 2006.

[73] Shlomi Kotler, Nitzan Akerman, Yinnon Glickman, Anna Keselman, and Roee Ozeri. Single-ion quantum lock-in amplifier. *Nature*, 473(7345):61–65, 05 2011.

[74] Kevin Cox, Valery I. Yudin, Alexey V. Taichenachev, Irina Novikova, and Eugeniy E. Mikhailov. Measurements of the magnetic field vector using multiple electromagnetically induced transparency resonances in rb vapor. *Phys. Rev. A*, 83:015801, Jan 2011.

[75] Jiancheng Fang and Jie Qin. In situ triaxial magnetic field compensation for the spin-exchange-relaxation-free atomic magnetometer. *Review of Scientific Instruments*, 83(10):103104, 2012.

[76] A Smith, S Chaudhury B E Anderson, and P S Jessen. Three-axis measurement and cancellation of background magnetic fields to less than 50 ug in a cold atom experiment. *J. Phys. B: At. Mol. Opt. Phys.*, 44(205002), 2011.

[77] A. Abragam. *The Principles of Nuclear Magnetism*. Oxford university press, 1961.

[78] Taquin, J. Line-shape and resolution enhancement of high-resolution f.t.n.m.r. in an inhomogeneous magnetic field. *Rev. Phys. Appl. (Paris)*, 14(6):669–681, 1979.

[79] S. Trotzky, Y-A. Chen, A. Flesch, I. P. McCulloch, U. Schollwock, J. Eisert, and I. Bloch. Probing the relaxation towards equilibrium in an isolated strongly correlated one-dimensional bose gas. *Nat Phys*, 8(4):325–330, 04 2012.

[80] M. Kendall and A. Stuart. *The advanced theory of statistics. Vol.2*. London, Griffin, 1979.

[81] J. M. Geremia, John K. Stockton, and Hideo Mabuchi. Tensor polarizability and dispersive quantum measurement of multilevel atoms. *Phys. Rev. A*, 73:042112, Apr 2006.

[82] John Kenton Stockton. *Continuous quantum measurement of cold alkali-atom spins*. PhD thesis, California Institute of Technology, Mar 2007.

[83] T. Takano, M. Fuyama, R. Namiki, and Y. Takahashi. Spin squeezing of a cold atomic ensemble with the nuclear spin of one-half. *Phys. Rev. Lett.*, 102:033601, Jan 2009.

[84] J. M. Higbie, L. E. Sadler, S. Inouye, A. P. Chikkatur, S. R. Leslie, K. L. Moore, V. Savalli, and D. M. Stamper-Kurn. Direct nondestructive imaging of magnetization in a spin-1 bose-einstein gas. *Phys. Rev. Lett.*, 95:050401, Jul 2005.

[85] Y. Liu, E. Gomez, S. E. Maxwell, L. D. Turner, E. Tiesinga, and P. D. Lett. Number fluctuations and energy dissipation in sodium spinor condensates. *Phys. Rev. Lett.*, 102:225301, Jun 2009.

[86] R. J. Sewell, M. Koschorreck, M. Napolitano, B. Dubost, N. Behbood, and M. W. Mitchell. Magnetic sensitivity beyond the projection noise limit by spin squeezing. *Phys. Rev. Lett.*, 109:253605, Dec 2012.

[87] R. A. Fisher. Theory of statistical estimation. *Mathematical Proceedings of the Cambridge Philosophical Society*, 22(05):700–725, 1925.

[88] Greg A. Smith, Souma Chaudhury, Andrew Silberfarb, Ivan H. Deutsch, and Poul S. Jessen. Continuous weak measurement and nonlinear dynamics in a cold spin ensemble. *Phys. Rev. Lett.*, 93:163602, Oct 2004.

[89] Richard J. Nelson, Yaakov Weinstein, David Cory, and Seth Lloyd. Experimental demonstration of fully coherent quantum feedback. *Phys. Rev. Lett.*, 85:3045–3048, Oct 2000.

[90] W. P. Smith, J. E. Reiner, L. A. Orozco, S. Kuhr, and H. M. Wiseman. Capture and release of a conditional state of a cavity qed system by quantum feedback. *Phys. Rev. Lett.*, 89:133601, Sep 2002.

[91] H. M. Wiseman. Quantum theory of continuous feedback. *Phys. Rev. A*, 49:2133–2150, Mar 1994.

[92] Géza Tóth and Morgan W Mitchell. Generation of macroscopic singlet states in atomic ensembles. *New Journal of Physics*, 12(5):053007, 2010.

[93] E. F. Burton. Viscosity of helium i and helium ii. *NATURE*, 135:265–265, Jan-Jun 1935.

[94] P. Kapitza. Viscosity of liquid helium below the lambda-point. *NATURE*, 141:74–74, Jan-Jun 1938.

[95] D. C. Tsui, H. L. Stormer, and A. C. Gossard. Two-dimensional magnetotransport in the extreme quantum limit. *Phys. Rev. Lett.*, 48:1559–1562, May 1982.

[96] J. Chiaverini, J. Britton, D. Leibfried, E. Knill, M. D. Barrett, R. B. Blakestad, W. M. Itano, J. D. Jost, C. Langer, R. Ozeri, T. Schaetz, and D. J. Wineland. Implementation of the semiclassical quantum fourier transform in a scalable system. *Science*, 308(5724):997–1000, 2005.

[97] T. Monz, K. Kim, A. S. Villar, P. Schindler, M. Chwalla, M. Riebe, C. F. Roos, H. Häffner, W. Hänsel, M. Hennrich, and R. Blatt. Realization of universal ion-trap quantum computation with decoherence-free qubits. *Phys. Rev. Lett.*, 103:200503, Nov 2009.

[98] J. Appel, P. J. Windpassinger, D. Oblak, et al. Mesoscopic atomic entanglement for precision measurements beyond the standard quantum limit. *Proceedings of the National Academy of Sciences*, 106:10960, 2009.

[99] Monika H. Schleier-Smith, Ian D. Leroux, and Vladan Vuletić. States of an ensemble of two-level atoms with reduced quantum uncertainty. *Phys. Rev. Lett.*, 104:073604, Feb 2010.

[100] C Gross, T Zibold, E Nicklas, J Esteve, and M K Oberthaler. Nonlinear atom interferometer surpasses classical precision limit. *Nature*, 464(7292):1165–1169, 2010.

[101] Seth Lloyd. Universal quantum simulators. *Science*, 273(5278):1073–1078, 1996.

[102] E. Jané, G. Vidal, W. Dür, P. Zoller, and J. I. Cirac. Simulation of quantum dynamics with quantum optical systems. *Quantum Info. Comput.*, 3(1):15–37, January 2003.

[103] S. van der Meer. Stochastic cooling and the accumulation of antiprotons. *Rev. Mod. Phys.*, 57:689–697, Jul 1985.

[104] B. D'Urso, B. Odom, and G. Gabrielse. Feedback cooling of a one-electron oscillator. *Phys. Rev. Lett.*, 90:043001, Jan 2003.

[105] Asa Hopkins, Kurt Jacobs, Salman Habib, and Keith Schwab. Feedback cooling of a nanomechanical resonator. *Phys. Rev. B*, 68:235328, Dec 2003.

[106] M. Poggio, C. L. Degen, H. J. Mamin, and D. Rugar. Feedback cooling of a cantilever's fundamental mode below 5 mk. *Phys. Rev. Lett.*, 99:017201, Jul 2007.

[107] Pavel Bushev, Daniel Rotter, Alex Wilson, Fran çois Dubin, Christoph Becher, Jürgen Eschner, Rainer Blatt, Viktor Steixner, Peter Rabl, and Peter Zoller. Feedback cooling of a single trapped ion. *Phys. Rev. Lett.*, 96:043003, Feb 2006.

[108] Markus Koch, Christian Sames, Alexander Kubanek, Matthias Apel, Maximilian Balbach, Alexei Ourjoumtsev, Pepijn W. H. Pinkse, and Gerhard Rempe. Feedback cooling of a single neutral atom. *Phys. Rev. Lett.*, 105:173003, Oct 2010.

[109] Tongcang Li, Simon Kheifets, and Mark G. Raizen. Millikelvin cooling of an optically trapped microsphere in vacuum. *Nat Phys*, 7(7):527–530, 07 2011.

[110] Jan Gieseler, Bradley Deutsch, Romain Quidant, and Lukas Novotny. Subkelvin parametric feedback cooling of a laser-trapped nanoparticle. *Phys. Rev. Lett.*, 109:103603, Sep 2012.

[111] X. Zhou, I. Dotsenko, B. Peaudecerf, T. Rybarczyk, C. Sayrin, S. Gleyzes, J. M. Raimond, M. Brune, and S. Haroche. Field locked to a fock state by quantum feedback with single photon corrections. *Phys. Rev. Lett.*, 108:243602, Jun 2012.

[112] I. Urizar-Lanz, P. Hyllus, I. Egusquiza, M. W. Mitchell, and G. Toth. Macroscopic singlet states for gradient magnetometry. *ArXiv e-prints*, March 2012.

[113] Hideo Mabuchi and Navin Khaneja. Principles and applications of control in quantum systems. *International Journal of Robust and Nonlinear Control*, 15(15):647–667, 2005.

[114] Souma Chaudhury, Seth Merkel, Tobias Herr, Andrew Silberfarb, Ivan H. Deutsch, and Poul S. Jessen. Quantum control of the hyperfine spin of a cs atom ensemble. *Phys. Rev. Lett.*, 99:163002, Oct 2007.

[115] N. Behbood, F. Martin Ciurana, G. Colangelo, M. Napolitano, M. W. Mitchell, and R. J. Sewell. Real-time vector field tracking with a cold-atom magnetometer. *Applied Physics Letters*, 102(17):173504, 2013.

[116] A. Sørensen, L. M. Duan, J. I. Cirac, and P. Zoller. Many-particle entanglement with bose-einstein condensates. *Nature*, 409(6816):63–66, 01 2001.

[117] Anne Louchet-Chauvet, Jürgen Appel, Jelmer J Renema, Daniel Oblak, Niels Kjaergaard, and Eugene S Polzik. Entanglement-assisted atomic clock beyond the projection noise limit. *New J. Phys.*, 12(6):065032, 2010.

[118] Zilong Chen, Justin G. Bohnet, Shannon R. Sankar, Jiayan Dai, and James K. Thompson. Conditional spin squeezing of a large ensemble via the vacuum rabi splitting. *Phys. Rev. Lett.*, 106:133601, Mar 2011.

[119] Masahiro Kitagawa and Masahito Ueda. Squeezed spin states. *Phys. Rev. A*, 47:5138–5143, Jun 1993.

[120] D. J. Wineland, J. J. Bollinger, W. M. Itano, and D. J. Heinzen. Squeezed atomic states and projection noise in spectroscopy. *Phys. Rev. A*, 50:67–88, Jul 1994.

[121] A. Kuzmich, N. P. Bigelow, and L. Mandel. Atomic quantum non-demolition measurements and squeezing. *Europhys. Lett.*, 42(5):481, 1998.

[122] C. Orzel, A. K. Tuchman, M. L. Fenselau, M. Yasuda, and M. A. Kasevich. Squeezed states in a bose-einstein condensate. *Science*, 291(5512):2386–2389, 2001.

[123] V. Meyer, M. A. Rowe, D. Kielpinski, C. A. Sackett, W. M. Itano, C. Monroe, and D. J. Wineland. Experimental demonstration of entanglement-enhanced rotation angle estimation using trapped ions. *Phys. Rev. Lett.*, 86:5870–5873, Jun 2001.

[124] J. Esteve, C. Gross, A. Weller, S. Giovanazzi, and M. K. Oberthaler. Squeezing and entanglement in a bose-einstein condensate. *Nature*, 455(7217):1216–1219, 10 2008.

[125] Giuseppe Vitagliano, Philipp Hyllus, I. L. Egusquiza, and Géza Tóth. Spin squeezing inequalities for arbitrary spin. *Phys. Rev. Lett.*, 107:240502, Dec 2011.

[126] Géza Tóth, Christian Knapp, Otfried Gühne, and Hans J. Briegel. Spin squeezing and entanglement. *Phys. Rev. A*, 79:042334, Apr 2009.

[127] Géza Tóth. Entanglement detection in optical lattices of bosonic atoms with collective measurements. *Phys. Rev. A*, 69:052327, May 2004.

[128] Marcin Wieśniak, Vlatko Vedral, and Časlav Brukner. Magnetic susceptibility as a macroscopic entanglement witness. *New Journal of Physics*, 7(1):258, 2005.

[129] Géza Tóth, Christian Knapp, Otfried Gühne, and Hans J. Briegel. Optimal spin squeezing inequalities detect bound entanglement in spin models. *Phys. Rev. Lett.*, 99:250405, Dec 2007.

[130] Géza Tóth, Christian Knapp, Otfried Gühne, and Hans J. Briegel. Spin squeezing and entanglement. *Phys. Rev. A*, 79:042334, Apr 2009.

[131] Ian D. Leroux, Monika H. Schleier-Smith, and Vladan Vuletić. Implementation of cavity squeezing of a collective atomic spin. *Phys. Rev. Lett.*, 104:073602, Feb 2010.

[132] Justin G. Bohnet, Kevin C. Cox, Matthew A. Norcia, Joshua M. Weiner, Zilong Chen, and James K. Thompson. Reduced back-action for phase sensitivity 10 times beyond the standard quantum limit. *arXiv:1310.3177*, 2013.

[133] K. Eckert, Ł. Zawitkowski, A. Sanpera, M. Lewenstein, and E. S. Polzik. Quantum polarization spectroscopy of ultracold spinor gases. *Phys. Rev. Lett.*, 98:100404, Mar 2007.

[134] Géza Tóth, Christian Knapp, Otfried Gühne, and Hans J. Briegel. Optimal spin squeezing inequalities detect bound entanglement in spin models. *Phys. Rev. Lett.*, 99:250405, Dec 2007.

[135] Giuseppe Vitagliano, Iagoba Apellaniz, Iñigo L. Egusquiza, and Géza Tóth. Spin squeezing and entanglement for an arbitrary spin. *Phys. Rev. A*, 89:032307, Mar 2014.

[136] Bernd Lücke, Jan Peise, Giuseppe Vitagliano, Jan Arlt, Luis Santos, Géza Tóth, and Carsten Klempt. Detecting multiparticle entanglement of dicke states. *Phys. Rev. Lett.*, 112:155304, Apr 2014.

[137] Timur Sh. Iskhakov, Ivan N. Agafonov, Maria V. Chekhova, Georgy O. Rytikov, and Gerd Leuchs. Polarization properties of macroscopic bell states. *Phys. Rev. A*, 84:045804, Oct 2011.

[138] J. Sewell, R. M. Napolitano, N. Behbood, G. Colangelo, F. Martin Ciurana, and W. Mitchell, M.˙ Ultrasensitive atomic spin measurements with a nonlinear interferometer. *Phys. Rev. X*, 4:021045, Jun 2014.

[139] *See supplementary material at at [URL will be inserted by publisher] for further details and supporting experiments.*

[140] Takeshi Fukuhara, Adrian Kantian, Manuel Endres, Marc Cheneau, Peter Schausz, Sebastian Hild, David Bellem, Ulrich Schollwock, Thierry Giamarchi, Christian Gross, Immanuel Bloch, and Stefan Kuhr. Quantum dynamics of a mobile spin impurity. *Nat. Phys.*, 9(4):235–241, 04 2013.

[141] J. K. Korbicz, J. I. Cirac, and M. Lewenstein. Spin squeezing inequalities and entanglement of N qubit states. *Physical Review Letters*, 95:120502, 2005.

[142] D. A. Lidar, I. L. Chuang, and K. B. Whaley. Decoherence-free subspaces for quantum computation. *Phys. Rev. Lett.*, 81:2594–2597, Sep 1998.

[143] Stephen D. Bartlett, Terry Rudolph, and Robert W. Spekkens. Classical and quantum communication without a shared reference frame. *Phys. Rev. Lett.*, 91:027901, Jul 2003.

[144] Morris L. Eaton. *Multivariate statistics.* John Wiley & Sons, 1983.